

Title	RADIATION FROM RELATIVISTIC ELECTRONS IN A TURBULENT ELECTROMAGNETIC FIELD
Author(s)	寺木, 悠人
Citation	大阪大学, 2014, 博士論文
Version Type	VoR
URL	https://doi.org/10.18910/34030
rights	
Note	

Osaka University Knowledge Archive : OUKA

<https://ir.library.osaka-u.ac.jp/>

Osaka University

RADIATION FROM RELATIVISTIC ELECTRONS IN A TURBULENT ELECTROMAGNETIC FIELD

Yuto Teraki

Department of Earth and Space Science

Graduate School of Science

Osaka University, Osaka, JAPAN

1-1 Machikaneyama-cho, Toyonaka, Osaka 560-0043, Japan

teraki@vega.ess.sci.osaka-u.ac.jp

Submitted to Osaka university: February 2014

Abstract

We present the results of the first principle numerical calculations for the radiation spectrum from relativistic electrons moving in a turbulent electromagnetic field and its applications to high energy astrophysical objects. Our method does not contain any approximations for the calculation of the radiation spectrum from prescribed electron trajectories, since the Lienard-Wiechert potential is employed directly. We investigate the cases for which we cannot use any approximated radiation formula.

We first show the radiation spectra from electrons moving in a static and small scale magnetic turbulence. The radiation is characterized by the strength parameter $a \equiv \omega_{\text{st}}/k_{\text{typ}}c = e\sigma/mc^2k_{\text{typ}}$, where ω_{st} is the cyclotron frequency defined by the spatial averaged magnetic field strength $\sigma = \langle B^2 \rangle^{1/2}$, and k_{typ}^{-1} is the typical scale of the magnetic turbulence. For $a \gg \gamma$, where γ is the Lorentz factor of the radiating electrons, and for $a \ll 1$, the radiation has been well studied as the synchrotron radiation and the jitter radiation, respectively. We investigate the radiation spectra for previously unexplored parameter range of $1 \lesssim a \lesssim \gamma$. The obtained spectrum shows a novel shape which has not been seen before. The spectrum in middle frequency region resembles the synchrotron one, but the spectrum of frequency region lower than $a^{-3}\gamma^2\omega_{\text{st}}$ deviate from it, and an extra power law component emerges in frequency region higher than the synchrotron cutoff. We interpret this newly found spectral shape by considering the electron orbit.

Secondly, we investigate the radiation from electrons in a Langmuir (electrostatic) turbulence. Since the Langmuir waves oscillate rapidly with plasma frequency ω_p , we take it into

account. We perform calculations of radiation spectra for various values of a defined by using $\sigma = \langle E^2 \rangle^{1/2}$ and of oscillation parameter $b \equiv \omega_p/k_{\text{typ}}c$, and we obtain a chart of spectral signatures in $a - b$ plane. The most important results here is the clarification of the spectral shape for $a > b > 1$, which has been misidentified or confused in other previous studies. The typical frequency is $\sim \gamma^2 \omega_{\text{st}}$, and the spectral index in the frequency region lower than the typical frequency is $1/3$. We confirm the origin of the newly found signatures by semi-analytical calculations and name the radiation mechanism for $a > b > 1$ "Wiggler Radiation in Langmuir turbulence" (WRL) after the Wiggler, which is an insertion device of the intense high energy radiation, since the mechanism which determines the spectral features resembles the Wiggler mechanism.

Thirdly, we propose a model of the gamma ray flares of the Crab nebula using the radiation signatures of the jitter radiation. The central problem here is that the peak energy of the flares exceeds the maximum energy E_c determined by synchrotron radiation loss. When there exists a turbulent magnetic field with $a < 1$, jitter radiation can emit photons with energy higher than E_c . We discuss a model in which the flares are triggered by plunging of the high density blobs into the termination shock and forming the magnetic turbulence with $a < 1$. We predict the observational signatures for future observations to be confronted with our models.

Contents

Abstract	i
Acknowledgements	iii
1 Introduction	1
2 Observations of High Energy Astrophysical Objects	5
2.1 Gamma ray bursts	5
2.2 Relativistic jets in active galactic nuclei	8
2.3 Gamma ray flares of the Crab nebula	11
3 Past Studies for Radiation Spectrum	15
3.1 Breaks of synchrotron and inverse Compton approximations	16
3.2 Radiation theories for turbulent electromagnetic fields	18
3.3 Parameters of electromagnetic turbulences	21
4 Method of Numerical Calculation	23
4.1 Field description	23
4.1.1 Magnetic turbulence	24
4.1.2 Langmuir turbulence	25
4.2 Equation of motion and radiation spectra	27

5	Magnetic Turbulence	29
5.1	Results	29
5.2	Interpretation	33
5.3	Summary	36
6	Langmuir Turbulence	39
6.1	Results	39
6.1.1	Short wavelength regime	39
6.1.2	Long wavelength and weak regime	44
6.1.3	Long wavelength and strong regime	45
6.2	Pure plasma oscillation	48
6.3	Discussion & Summary	58
7	Application to the Gamma Ray Flares of the Crab Nebula	63
7.1	Introduction	63
7.2	Jitter radiation model	65
7.2.1	Small scale turbulence	65
7.2.2	Energetics	69
7.2.3	Spectrum	73
7.3	Discussion	76
7.3.1	Difference from other models and predictions	76
7.3.2	Acceleration and scatterers	77
7.4	Summary & Conclusion	78
8	Overall Conclusions	81
8.1	Spectral features for isotropic electromagnetic turbulence	82
8.2	Jitter radiation model of the Crab gamma ray flares	83
	Appendix	84

A Basic Concepts of Radiation from a Single Particle	85
A.1 Synchrotron radiation	85
A.2 Useful concepts	89
A.2.1 Photon Formation Time and Photon Formation Length	90
A.2.2 Method of virtual quanta	92
A.2.3 Wiggler and Undulator	93
B Details of Past Studies	95
B.1 Jitter radiation	96
B.2 Multi dimensional jitter radiation and Diffusive Synchrotron Radiation	100
B.3 Beyond the perturbative DSR theory	103
B.4 Other studies	104
C Physical Interpretations of Spectral Indices in Various Regions Considered in this Thesis	111
C.1 Undulator	111
C.2 Jitter radiation	113
C.2.1 One-dimensional jitter radiation	114
C.2.2 Multi dimensional jitter radiation	114
C.2.3 LPM effect on the jitter radiation	115
C.3 DRL: small deflection regime	116
C.4 Wiggler radiation: low frequency	118
D Turbulent Electromagnetic Field	123
D.1 Electromagnetic turbulences in PIC simulations	123
D.2 Linear analysis	126
D.2.1 Dispersion relation	126
D.2.2 Weibel (filamentation) instability	128

D.2.3 Two stream instability	131
--	-----

Bibliography	135
---------------------	------------

Acknowledgements

I would like to thank at first Professor Fumio Takahara for being my supervisor and a great partner for the discussions. I think that I was very lucky to become a graduate student under him. I also thank Professor Kentaro Nagamine for being a boss of my research laboratory. This thesis may have not been completed without his cooperation. I would like to extend my gratitude to Associate Professor Yutaka Fujita, Assistant Professor Hideyuki Tagoshi, Assistant Professor Toru Tsuribe, Dr. Kenji Toma for useful discussions. I am also grateful to the present and past students of Theoretical Astrophysics Group in the Osaka University for fruitful discussions, and Secretaries Yasuko Nishii and Mayumi Sasaki for their kind supports. This work is supported by JSPS Research Fellowships for Young Scientists (24593). Finally, I thank my wife and my family for supporting me all over the life.

Chapter 1

Introduction

High energy astrophysical objects such as Gamma Ray Bursts (GRB), Active Galactic Nuclei (AGN), and Pulsar Wind Nebulae (PWN) are the most spectacular phenomena in the universe. It is common that they have relativistic flows, i.e., relativistic jets or relativistic winds. Their bulk kinetic energy is converted to the thermal and non-thermal particles at collisionless shocks, which are formed by plunging of jets or winds into ambient matters (external shocks), or by collisions of their internal structures (internal shocks). In addition, the magnetic reconnection may play an important role for energy conversion. The energy is finally converted to the high energy radiation by non-thermal particles. The major part of radiation is from high energy electrons, although high energy protons sometimes involve creating gamma ray emission. The electrons emit X-rays and gamma-rays by synchrotron and Inverse Compton scattering, which are most popular explanations for the observed spectra. However, there are many observations which are inconsistent with these radiation theories. Although much effort has been put in making explanations for those observations, they are still open problems.

The turbulence is one of the promising factors for the radiation mechanism which we have not fully considered. From the viewpoint of the particle acceleration, it has been claimed that the turbulent electromagnetic fields are generated and amplified by some plasma instabilities at the shock region. However, the study of the radiation mechanisms from electrons in electro-

magnetic turbulence are still embryotic. Medvedev (2000) proposed the radiation mechanism from a relativistic electron moving in a static small scale turbulent magnetic field in the context of the GRB, and he called this radiation mechanism "jitter radiation". Fleishman (2006) extended the radiation theory for multi dimensional turbulence, and he called the radiation mechanism "Diffusive Synchrotron Radiation". Stimulated by these studies, some researchers including themselves have been trying to clarify the radiation features from electrons in general electromagnetic turbulences. These researches have not been completed yet.

It is the goal of this thesis to shed light on the radiation theory in the context of the high energy astrophysical objects. We perform first principle numerical calculations to obtain the radiation spectra for various electromagnetic turbulences. In chapter 2, we describe the summary of the observational facts which are hard to explain with the existing radiation theories. In chapter 3, we describe the summary of the past studies related to our study in this thesis. We also describe our motivations for investigations of the radiation spectra here. In chapter 4, we describe our numerical method which we use to calculate the radiation spectra from electrons moving in random electromagnetic fields. In chapter 5, we present the results of calculations of radiation spectra for static magnetic turbulence. This chapter 5 is based on the paper Teraki & Takahara (2011). In chapter 6, we present the results of the calculations of radiation spectra for oscillating Langmuir turbulence. This chapter 6 is based on the paper Teraki & Takahara (submitted to ApJ). In chapter 7, we present a model of the unresolved observational results of the gamma ray flares of the Crab nebula. We reproduce the flare by jitter radiation mechanism, and discuss the constraints on the physical situation when flares occur. This chapter 7 is based on the paper Teraki & Takahara (2013). In chapter 8, we draw an overall summary and conclusions. In Appendix A, we review the basics of the radiation from a relativistic charged particle. In Appendix B, we review past studies related to this thesis in detail, which is an extension of the chapter 3. In Appendix C, we describe the physical interpretations of spectral indices which emerge in the radiation spectra in various configurations of electromagnetic turbulences. In Appendix D, we review the generation of the

electromagnetic turbulences by plasma instabilities.

Chapter 2

Observations of High Energy Astrophysical Objects

In this chapter, we shortly review the observations of the high energy astrophysical objects which have relevances to this thesis. We concentrate our interests on the observational facts which we refer to in later chapters.

2.1 Gamma ray bursts

Gamma-ray bursts (GRB) are intense signals of ~ 100 keV- 1 MeV photons lasting for $10^{-3} - 10^3$ s and appear at random in the sky about once a day. These short, energetic bursts of γ -rays are likely signs of the birth of rapidly spinning, stellar-mass black holes or neutron stars with high magnetization. They also reveal very broadband afterglows, from radio to X-rays. Moreover, they are at cosmological distances, being a unique tool to explore the state of the entire universe. Now it is believed that a highly relativistic plasma jet which is ejected from a collapsing star emits γ -rays, and the interaction of the jet with surrounding medium of the source makes afterglow. However, it remains unclear how the jet produces the γ -rays. The standard model of GRB is based on the synchrotron radiation from accelerated electrons at the

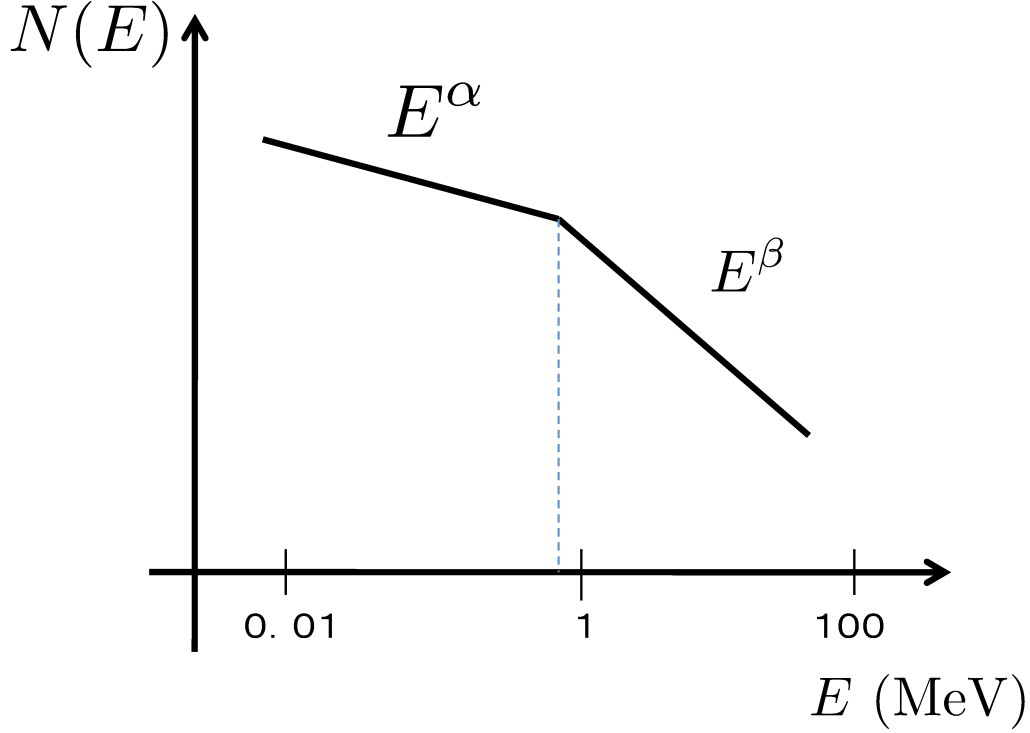


Figure 2.1: Typical spectrum of the GRB. This spectral shape is represented Band function equation (2.1).

internal shocks in the jets. However, a nonnegligible number of GRB contradict this model. The observational spectra of prompt emission of GRB are well described by a smoothly-joining broken power law, known as the "Band function" (Band et al., 1993)

$$N(E) = N_0 \begin{cases} (E/E_0)^\alpha \exp(-E/E_0) & \text{for } E < (\alpha - \beta)E_0, \\ (E/E_0)^\beta (\alpha - \beta)^{\alpha-\beta} \exp(\beta - \alpha) & \text{for } E > (\alpha - \beta)E_0, \end{cases} \quad (2.1)$$

which is depicted in Figure 2.1. Three independent spectral parameters are involved, i.e., a low energy photon spectral index α , a high energy photon spectral index β , and the transition energy E_0 or peak of $E^2 N(E)$ spectrum for $\beta < -2$ ($E_p = (\alpha + 2)E_0$). It is found that α

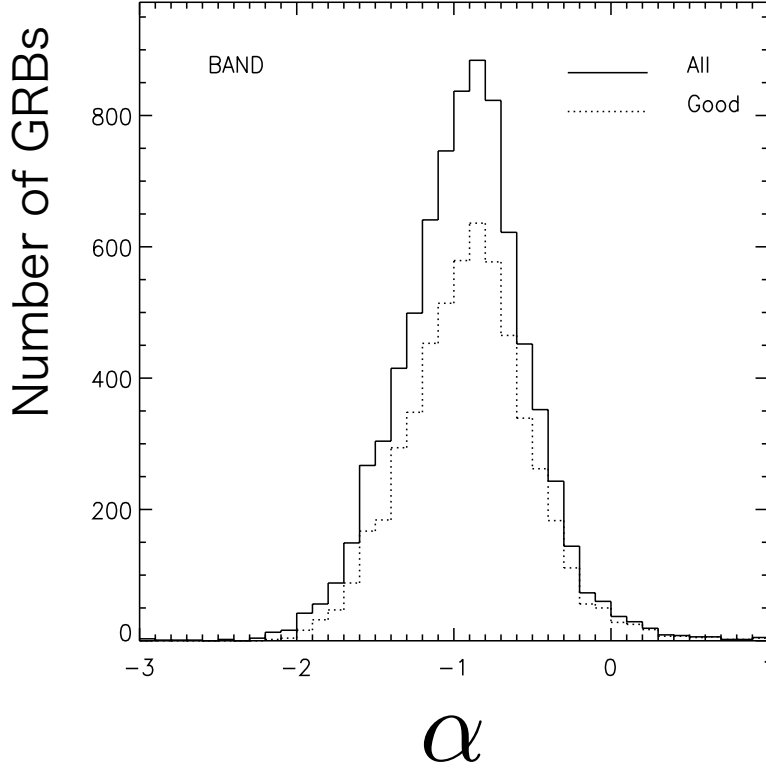


Figure 2.2: Observed distribution of α which is the photon index of the low energy side of the Band function (Kanku et al. 2006).

centered around -1 and their distribution width is ~ 1 , and β centered around -2.2 and their distribution width is ~ 1.5 . E_p distribution is log-normal, centered around ~ 250 keV. Around a third of GRBs show a spectrum in the low energy side of the peak harder than the synchrotron theory predicts ($\alpha > -2/3$), which is firstly claimed by Preece et al. (1998), and we can see them in the α -distribution in Figure 2.2 (Kaneko et al. 2006). It is a crucial problem, because the observations of a third of GRB contradict the standard scenario. To explain these GRBs, other radiation mechanisms are needed.

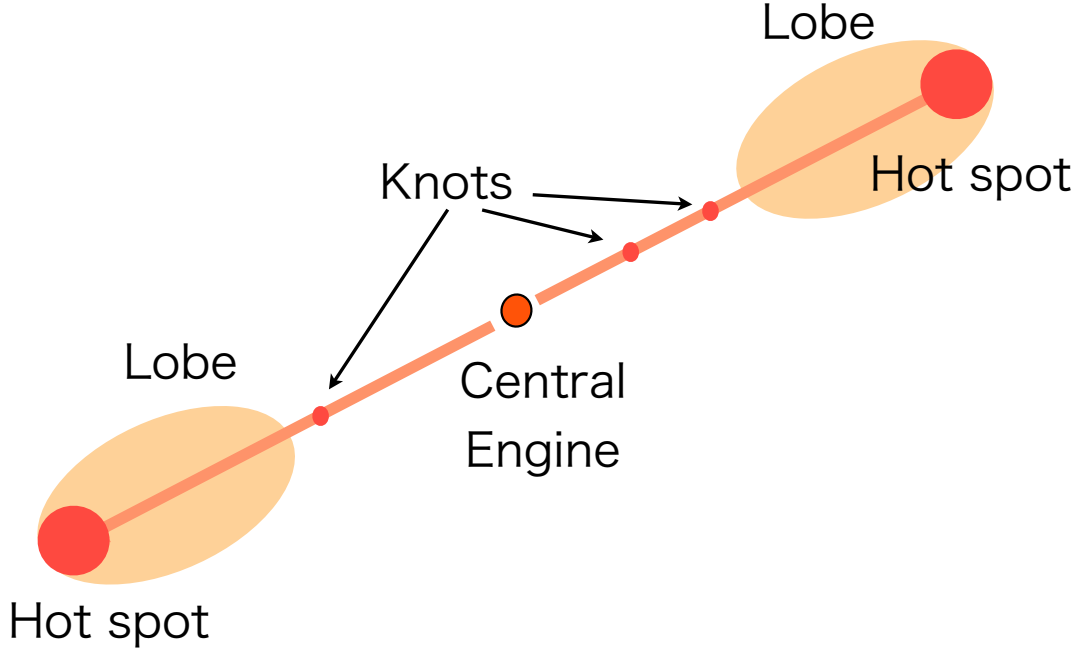


Figure 2.3: Cartoon of the typical morphology of AGN jets

2.2 Relativistic jets in active galactic nuclei

Active Galactic Nuclei (AGN) are the central region of a galaxy from where intense broadband radiation is emitted. According to the standard paradigm, the central engine of AGN consists of an accreting supermassive black hole (BH) weighing millions to several billions of solar masses. Moreover, relativistic jets are launched from vicinity of the BH.

We do not know the geometry of the accretion flow within a few tens of gravitational radii, i.e., whether it is thin disk that continues down to the innermost stable circular orbit (ISCO) or if the flow becomes closer to spherical near the BH. The accretion disk emits thermal ultraviolet, optical, and infrared radiation. Moreover, X-rays come from central engine. It

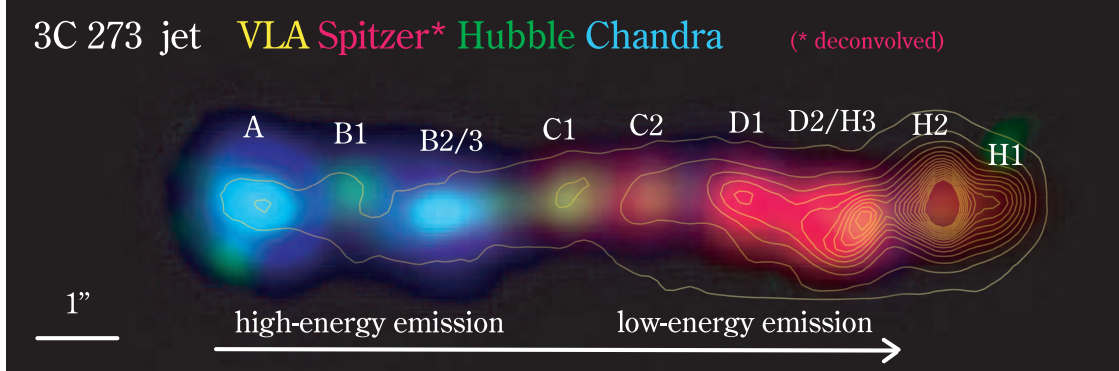


Figure 2.4: A composite image of the jet 3C 273. The colors correspond to the wavelength and also observation instruments. The wavelength of each instrument is as follows: VLA-radio, Spitzer-infrared, Hubble-optical, and Chandra-x-ray.

is thought to be from hot electrons in the corona by Compton scattering off some of these photons.

The jets can appear long or short, nearly straight or sharply curved, and relatively smooth or dominated by knots. The majority of knots move at apparently superluminal velocities (Jorstad et al. 2001, 2005). From this fact, we know that the jets have relativistic speed. This large amount of bulk kinetic energy is converted to the particle energy and electromagnetic field at the shock region. The synchrotron radiation and inverse Compton scattering are also major emission mechanism for the emission regions such as knots, hot spots and lobes of AGN

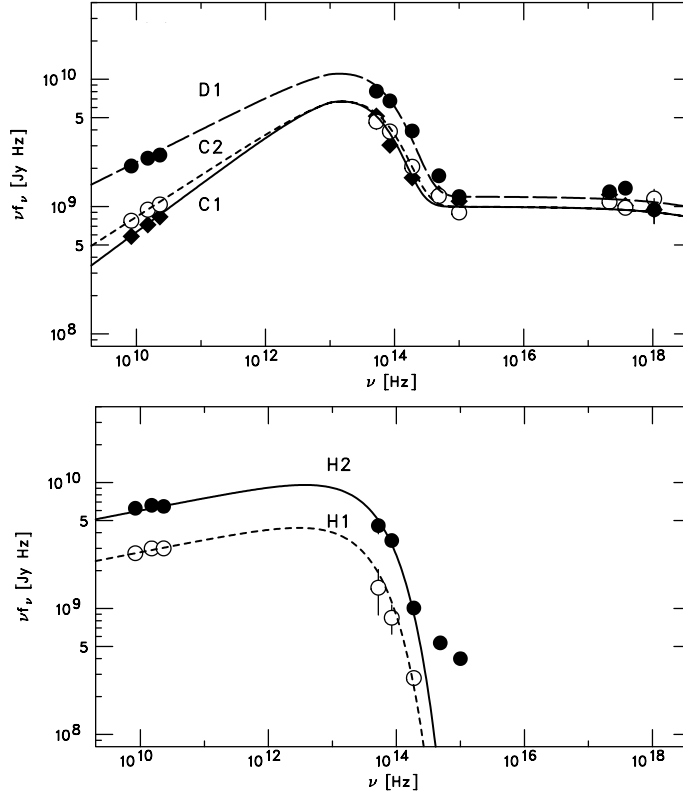


Figure 2.5: Broadband spectral energy distributions of the 3C 273 jet. Upper panel shows radiation spectra of knot regions of D1, C2, and C1 in Figure 2.4. Lower panel shows radiation spectra of head regions of H1 and H2. Extra components are seen beyond the first cut off around 10^{14} Hz .

jets. A cartoon of them is depicted in Figure 2.3. The superluminal knots are thought to be the internal shock region, and a part of subluminal knots may be the recollimation shock region. The internal structure is smoothed out by internal shocks. Then, the average flow interacts with the external medium and forms the external shock. This terminated region is the hot spots, and the thermalized gas expands sideways and makes the radio lobe (Figure 2.3).

The standard model of AGN is as above. This model has succeeded in explaining the observed signatures, such as the morphology and multiband spectra. However, there are observations which are difficult to explain by a simple picture in the standard model. For

example, the optical region of radiation spectra of knots and hot spots for 3C273 shows peculiar trend (Uchiyama et al. 2006). They are described by a power law in radio region and there is a cutoff feature in infrared region, and an extra power law component emerges in optical to X-ray region (Figure 2.5). We can see the cutoff and extra power law component in the spectra for both of knot regions D1 and C2. On the other hand, although we see that feature in the hot spot of H2, we do not see that in the hot spot H1. The major interpretation of this type of spectra is synchrotron radiation from two populations of non thermal electrons. However, it is ambiguous how to make two distinct electron populations. Alternatively, it might be possible that the emission is from a single electron population and the spectral shape is characterized by non-standard radiation mechanisms. We lastly note that the same spectral features are seen in other AGN jets such as PKS 1136-135 and 3C 445, which have been reported in a few papers (Uchiyama et al. 2007, Perlman et al. 2010). Thus, this may common features for AGN jets.

2.3 Gamma ray flares of the Crab nebula

The Crab nebula and its pulsar are among the best-studied objects in astronomy (X-ray image of the Crab nebula is shown in Figure 2.6, which is from Chandra website http://chandra.harvard.edu/photo/2002/0052/0052_xray_widefield.jpg). Their origin is a massive core-collapse supernova observed in the year 1054 A.D. During the explosion of the progenitor star, a fast-rotating neutron star, the Crab pulsar, was formed. The pulsar dissipates an enormous amount of rotational energy into the surrounding medium at a rate of $\sim 5 \times 10^{38}$ erg/s. Most of the luminosity is kinetic, i.e., pulsar wind has almost all spindown luminosity. The wind consists of mainly electrons and positrons, which are cold in the co-moving frame of the wind. Its bulk kinetic energy is converted to the particle energy at the termination shock. They form the pulsar wind nebula and lose their energy by radiation.

Although the Crab nebula has been regarded as a stationary emitter except for a secular

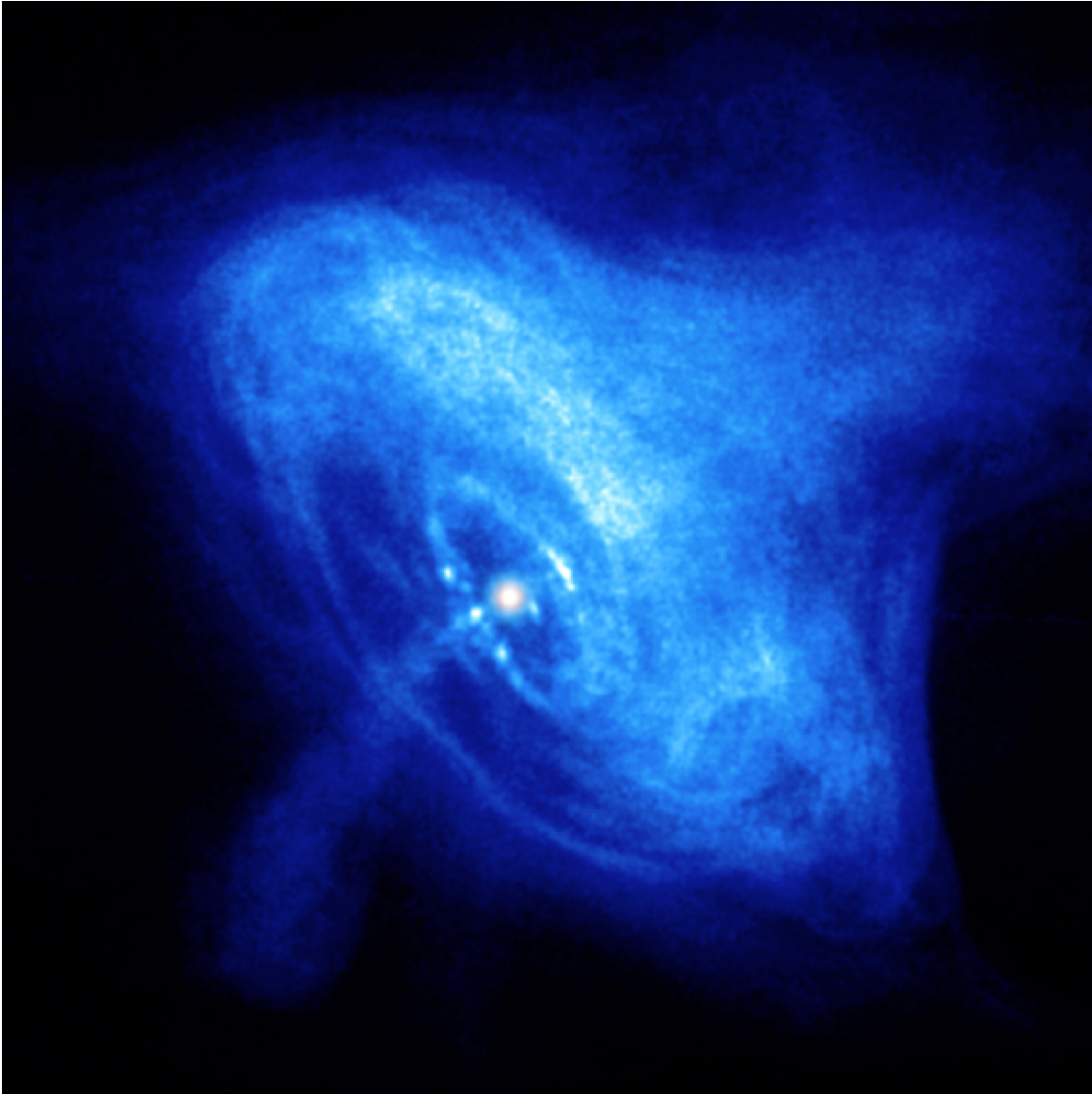


Figure 2.6: Chandra X-ray image of the Crab nebula from Chandra website.

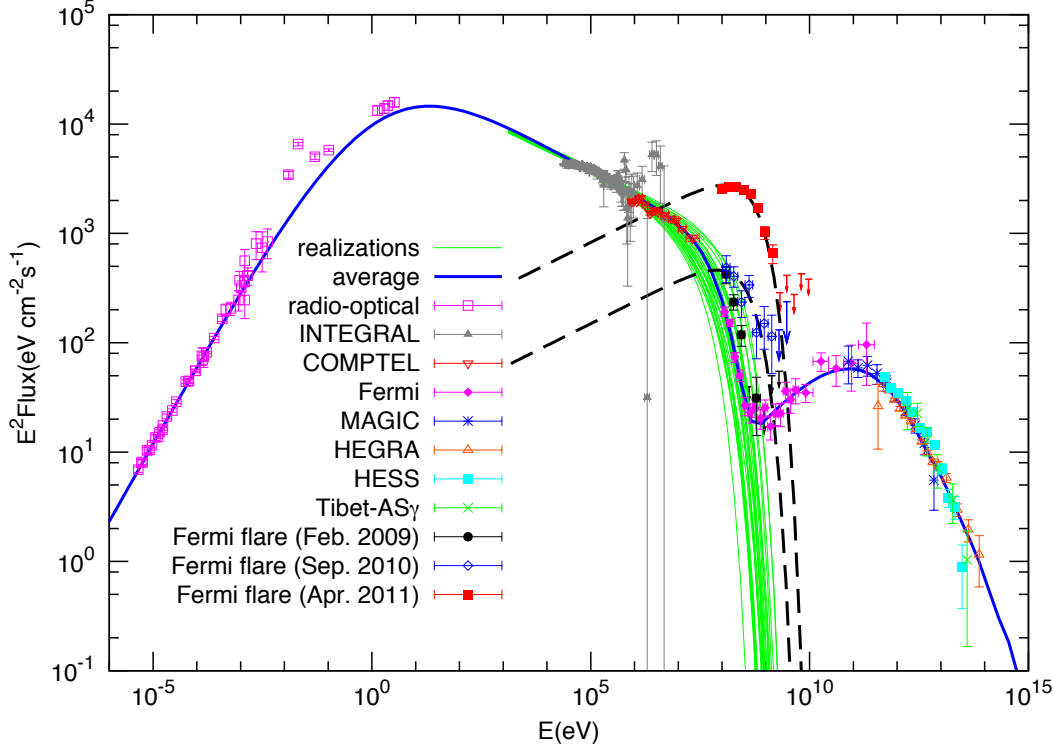


Figure 2.7: Multi band observed spectra of the Crab nebula (Yuan et al. 2011a). The filled red square is the strongest gamma rays flare observed by Fermi satellite in April 2011.

change due to the expansion, recently, strong flares were detected five times in the range > 100 MeV by AGILE (Tavani et al. 2011) and Fermi (Abdo et al. 2011, Buehler et al. 2012, Ojha et al. 2012) satellites (Figure 2.7). The flares occur about once in a half year, the flux doubling timescale is around 8 hours, and duration time is a few weeks. The peak energy is as high as 375 MeV which is a challenge for the standard scenario of pulsar wind nebulae (Buehler et al. 2012). When electrons/positrons are accelerated on gyro timescale, synchrotron radiation limits the attainable energy (see e.g. Kirk & Reville 2010), and the maximum energy of synchrotron radiation is ~ 100 MeV. It is notable that this maximum energy of the synchrotron radiation does not depend on the magnetic field strength. The

peak energy of the flares exceeds this value, it is the central serious problem of these flares. Since there seem to be no counterparts in other energy ranges, they should involve only the highest energy particles. In fact, the flare of April 2011 shows very hard spectrum. The photon index is $\gamma_F = 1.27 \pm 0.12$ which is averaged about time in all over the flare state (Buehler et al. 2012), and become as hard as $\gamma_F = 1.08 \pm 0.16$ which is calculated in only the most luminous period in the flare period (Clausen-Brown & Lyutikov 2012). The peak flux amounts to $(186 \pm 6) \times 10^{-7} \text{cm}^{-2} \text{s}^{-1}$, 30 times larger than the quiescent one. The isotropic luminosity amounts to $4 \times 10^{36} \text{erg s}^{-1}$ corresponding to 1% of the spin down luminosity of the Crab pulsar. The size of emission region of the flares should be as small as $ct_{\text{fluc}} \sim 10^{15} \text{cm}$ or $ct_{\text{dur}} \sim 3 \times 10^{16} \text{cm}$, where t_{fluc} is the fluctuation timescale estimated from flux changes and t_{dur} is the duration timescale of the flares. Either of them is very small compared to the circumference of the termination shock $2\pi r_{\text{ts}} \sim 2 \times 10^{18} \text{cm}$, where r_{ts} is the radius of the termination shock from the Crab pulsar. It is notable that such a large amount of energy is concentrated in a small region. The peak of the νF_ν spectrum of the Crab nebula is in the optical band. It is about $2 \times 10^{37} \text{erg/s}$. On the contrary, the mean value in the flaring state of April 2011 flare is $2 \times 10^{36} \text{erg/s}$. We have to reproduce such a high luminosity in the models. We note that peculiar gamma ray flares such as that we show above have not been seen in other PWNe. Although more than 50 γ -ray pulsars are detected in energy range higher than 100 GeV, Fermi-LAT observed only four PWNe (Ackermann et al., 2011). Other PWNe than the Crab nebula show no evidence of the sharp decrease $\sim 100 \text{MeV}$ and the shallow increase above $\sim 1 \text{GeV}$ as seen in the Crab nebula.

Chapter 3

Past Studies for Radiation Spectrum

As we see in chapter 2, high energy astrophysical objects often contain features which are not easily explained by the conventional synchrotron and inverse Compton emissions. To explain these observations, the radiation mechanisms are still an active issue. Recently, much attention has been paid to the effects of electromagnetic turbulences on the radiation signatures (e.g., Medvedev 2000, Fleishman 2006, Kelner, Aharonian, & Khangulyan 2013 and Mao & Wang 2013), since the main scene of the emission regions of high energy astrophysical objects is collisionless shocks, and the turbulent electromagnetic fields would be generated in the shock region by some plasma instabilities (see Appendix D). However, the radiation spectra from relativistic electrons moving in turbulent electromagnetic fields have not been studied completely. There is a room for novel emission signatures in the consideration of turbulence. To show the unexplored field about radiation spectra from turbulent field, we start from a discussion of the break of synchrotron and inverse Compton approximations.

3.1 Breaks of synchrotron and inverse Compton approximations

Consider relativistic electron moving in a turbulent magnetic field. If the spatial scale of magnetic field (i.e. typical eddy scale) $\lambda_B = 2\pi/k_{\text{typ}}$ is much larger than the local Larmor radius of the electron, there is no difference between this turbulent field and the uniform magnetic field for this electron. Thus, the radiation spectrum is identical to the synchrotron radiation¹. On the other hand, if λ_B is much smaller than the local Larmor radius r_L , the electron does not trace a herical orbit, but rather trace an almost rectilinear orbit. The radiation from this electron should be different from the synchrotron radiation for this case.

Radiation spectra from a small scale turbulent magnetic field are recently rediscovered under a very simple configuration, and it is called the "jitter radiation" (Medvedev 2000). Before discussing the radiation for more general turbulence, we shortly show the one-dimensional jitter radiation. More detailed discussion is shown later in this chapter and Appendix B. In the treatment of Medvedev (2000), the magnetic turbulence is assumed to be essentially of one mode and one-dimensional dependence along the velocity written as $\vec{k}_{\text{typ}} = (k_x, 0, 0)$. Differences from the synchrotron radiation become significant when λ_B is smaller than the Photon Formation Length (PFL: the concept of PFL is explained in Appendix A.) of the synchrotron photons r_L/γ , where γ is the Lorentz factor of the electron. The reason of the PFL of the synchrotron radiation is not r_L but r_L/γ is from the relativistic beaming effects, and further explanation is written in Appendix A. When we can neglect the time variability of the turbulent field², the radiation spectrum is characterized by the spatial scale per PFL of synchrotron

¹Rigorously speaking, the radiation spectra from ensemble of electrons moving in large scale turbulence are not perfectly identical to the uniform magnetic field. Because of the fluctuation of the local strength and direction of magnetic field, the spectrum around the peak becomes broader and flatter than the spectrum for uniform field (Crusius & Schlickeiser 1986).

²In many cases of astrophysical shocks, Weibel instability is thought to be the most promising processes to generates the magnetic field. The Weibel instability generate magnetic entropy waves. The entropy mode

radiation, which is called strength parameter:

$$a = \lambda_B \frac{e|B|}{2\pi mc^2}, \quad (3.1)$$

where e is elementary charge, m is the mass of the electron, c is the speed of light, and $|B|$ is the strength of the magnetic fields. We note that the strength parameter does not depend on the particle Lorentz factor. When $a \gg \gamma$, the scale of turbulent fields is much larger than the Larmor radius, so that the synchrotron approximation is valid. In contrast, when $a \ll 1$, λ_B is much smaller than the scale r_L/γ , so that the electron change the acceleration direction before the beaming cone sweeps observer. In other words, the deflection angle θ_{def} when the electron moves the distance λ_B is smaller than $1/\gamma$. Therefore, jitter approximation that the observer is always in the beaming cone at least in one deflection time can be applied.

The spectral features of the jitter radiation are significantly different from the synchrotron radiation. For example, the peak frequency in ωF_ω spectrum is $\gamma^2 k_{\text{typ}} c$ for $a < 1$, which is different from the synchrotron frequency $\gamma^2 eB/mc$. The spectrum for the frequency region lower than the peak is $F_\omega \propto \omega^1$, while that for higher than the peak is an abrupt cutoff. As we see above, the spectrum for the magnetic turbulence is calculated for $a \ll 1$ and $a \gg \gamma$ by using appropriate approximations. However, when $1 \lesssim a \lesssim \gamma$, no simple approximation of the radiation spectrum has been known. This is an unexplored field for the static magnetic turbulent fields.

Next we discuss the break of the inverse Compton approximation. When a relativistic electron is moving in an electromagnetic wave, in other words, an relativistic electron interacting with photons, the radiation from the electron is usually called inverse Compton scattering. Rees (1972) claimed that this approximation breaks down when the strength of the electromagnetic field is very large, and he called it "synchro-Compton radiation". He assumed that does not oscillate, so the typical timescale is determined by the turnover time of an eddy. It is longer than the crossing time of a relativistic electron if we assume the background plasma is sub-relativistic. Therefore, we can treat the magnetic field as a static field when we calculate the radiation spectra for the zeroth-order approximation.

the strong electromagnetic wave is emitted from the Crab pulsar with frequency Ω (30Hz) according to the "oblique rotator" model by Ostriker & Gunn (1969), and argued that the radiation from an electron moving in the strong wave is not the inverse Compton scattering (with frequency $\gamma^2\Omega$) but synchrotron-like (synchro-Compton) radiation. He claimed that the radiation signature of synchro-Compton radiation resembles that of the synchrotron radiation. The typical frequency is determined by the field strength as $\gamma^2 eB/mc$, and the low frequency spectral index is roughly $1/3$. He pointed out that this wave fulfills the condition of $eB/mc > \Omega$, which is calculated from the frequency and strength of the strong wave. Therefore, the deflection angle θ_{def} is larger than $1/\gamma$ in this wave, so that the typical photon formation time (PFT) changes from $1/\Omega$ to mc/eB . Getmantsev & Tokarev (1972) stated that the radiation signature from a single charged particle is determined by frequency or wavelength of the background wave for $\theta_{\text{def}} \ll 1/\gamma$, while it is determined by the field strength for $\theta_{\text{def}} \gg 1/\gamma$ in the same way as synchrotron radiation as long as the energy variations at the particle motion in the arbitrary electromagnetic field are smaller than the energy of the particle. Although the explicit expressions of the radiation spectra from a single electron for $\theta_{\text{def}} \sim 1/\gamma$ are not known as they noted, they presented a general expression of radiation spectrum from an ensemble of electrons, since the radiation spectra from relativistic electrons with a power law distribution are weakly affected by the radiation features from a single particle. Their formula covers wide range of the physical conditions of emission regions in the astrophysical objects, since it is written for particles with power law distribution, which is the major particle distribution in the astrophysical objects.

3.2 Radiation theories for turbulent electromagnetic fields

After the pioneering works of seventies such as Getmantsev & Tokarev 1972, several works which calculate the radiation spectra precisely by using statistical treatments have been performed in eighties. Toptygin & Fleishman (1987, hereafter TF87) developed the most sophis-

ticated method for this approach. We shortly review their treatment in Appendix B. They introduced the critical wavelength λ_{crit} and called components with $\lambda \leq \lambda_{\text{crit}}$ the "small scale component", where λ_{crit} obeys the inequality

$$r_g \gg \lambda_{\text{crit}} \gg r_g/\gamma. \quad (3.2)$$

The inequality can be transformed to $1 \ll \lambda_{\text{crit}} e|B|/mc^2 \ll \gamma$, so that the division through λ_{crit} may be ambiguous. Based on the theory of TF87, Fleishman (2006) developed a radiation theory from a relativistic electron in a static turbulent magnetic field, and he call it Diffusive Synchrotron Radiation (DSR). Therefore, the critical wavelength in DSR theory is also ambiguously defined. It is a notable point for discussions in chapter 5.

For later convenience, we shortly review their treatment of DSR theory. They treat the electron motion by a statistical approach and use a perturbative treatment for calculation of the radiation. They firstly assume $a \ll 1$ and therefore, rectilinear trajectory with constant velocity but take into account non-zero acceleration from the external field. The calculation formula for the radiation spectra is the same as the one written in Landau & Lifshitz (1971) for $\theta_{\text{def}} \ll 1/\gamma$. They calculate the correlation between the acceleration and the Fourier modes of magnetic turbulence, and get the radiation spectra. The peak frequency in ωF_ω spectrum is $\gamma^2 k_{\text{typ}} c$, which is the same as the jitter radiation. The other spectral features are different from the one-dimensional jitter radiation because there are differences in assumed magnetic turbulences between the jitter theory and DSR theory. In DSR, the magnetic turbulence is isotropic and has a power law distribution represented as $B^2(k) \propto k^{-\mu}$. The radiation spectrum in frequency region lower than $\gamma^2 k_{\text{typ}} c$ is $F_\omega \propto \omega^0$, and becomes $F_\omega \propto \omega^{-\mu}$ in higher frequencies, because they assumed that the turbulence exists up to the maximum wave number $k_{\text{max}} \gg k_{\text{typ}}$, which is in contrast to the jitter radiation (Medvedev 2000). Next, they considered the effects of multiple scattering beyond the perturbative treatment for $a > 1$. The angle between the velocity and observer direction becomes larger than the beaming cone after many deflections even for $\theta_{\text{def}} < 1/\gamma$, and the approximation of rectilinear trajectory is broken. They treat the

change of direction of motion in many deflections by diffusion approximation. In consequence, a spectral break emerges in the low frequency region with a suppression of low frequency photons. The spectrum becomes $F_\omega \propto \omega^{1/2}$ from this effect and the index of $1/2$ comes from the diffusivity. We note that the physical interpretation of the spectral features above is shown in Appendix C. Using DSR theory, Fleishman & Urtiev (2010) calculated the radiation spectrum for the static magnetic turbulent field with $a > 1$. Such a magnetic turbulence is expected to be generated by Weibel instability around the shock front (see Appendix D). They claimed that the break frequency approaches the peak frequency as θ_{def} becomes large, and for frequency region just below the peak frequency $\gamma^2 k_{\text{typ}} c$ is $F_\omega \propto \omega^{1/2}$ even for $\theta_{\text{def}} \gg 1/\gamma$. The peak frequency for $a > 1$ is identical to $a < 1$ in DSR theory, which is inconsistent with the states by Getmantsev & Tokarev (1972).

The radiation mechanism from Langmuir turbulence has been little studied compared to the radiation from turbulent magnetic fields. The Langmuir turbulence has been pointed out to be also generated around the shock front of the relativistic shocks (Silva 2006, Dieckmann 2005, Bret, Dieckmann, & Deutch 2006), so it should be as important as the radiation from turbulent magnetic field. There are a few important works about this radiation process, such as Melrose 1971 which consider the typical frequency and Schlickeiser 2003 which consider the power of this process. Among these studies, Fleishman & Toptygin (2007a,b) have developed the most systematic treatment of radiation from electrons in Langmuir turbulence (see references cited in Fleishman & Toptygin 2007b for other earlier relevant studies). Their treatment is almost the same as the DSR except for the consideration of time variability of the Fourier components of the turbulent field (Langmuir waves). They call this radiation mechanism "Diffusive Radiation in Langmuir turbulence" (DRL). We shortly review these results. The wavenumber of the Langmuir waves is assumed to satisfy the condition $\omega_p > k_{\text{typ}} c$, where ω_p is the plasma frequency. They introduce a variable ω_{st} which is statistically averaged "strength frequency" which resembles cyclotron frequency for magnetic field, but the electric field strength E is used as $\omega_{\text{st}} = e \langle E^2 \rangle^{1/2} / mc$, where $\langle \rangle$ means ensemble average. For

$\omega_p > \omega_{st}$, the peak frequency is $\gamma^2 \omega_p$. The spectrum just below the peak frequency is $F_\omega \propto \omega^1$, and becomes $F_\omega \propto \omega^0$ in lower frequencies. For $\omega_p < \omega_{st}$, the peak frequency is also $\gamma^2 \omega_p$ and frequency region lower than the peak becomes $F_\omega \propto \omega^{1/2}$. This index of $1/2$ also comes from diffusivity, which is the same as non-perturbative DSR. The physical explanations about them are also shown in Appendix C.

DSR and DRL are most accepted radiation theory for the turbulent field. However, their results are inconsistent with the prediction by Getmantsev & Tokarev (1972). On the other hand, in recent paper about jitter radiation (Medvedev et al. 2011), they also claimed (without confirmation) that the radiation spectra resembles synchrotron radiation when $\theta_{def} > 1/\gamma$, which is consistent with Getmantsev & Tolarev (1972). The radiation spectra about these fields is in the discussion. We here summarize an unexplored field we discussed above for the radiation from a relativistic electron:

- The radiation spectra for strong deflection regime, such as $1 \lesssim a \lesssim \gamma$ for static magnetic turbulence and $\omega_{st} > \omega_p > k_{typ}c$ for Langmuir turbulence should be investigated.

We perform the first principle numerical calculations for clarification of them. It is the goal of this study to obtain general properties of the radiation spectra from a relativistic electron in oscillating and spatially fluctuating electromagnetic fields.

3.3 Parameters of electromagnetic turbulences

Before proceeding to the calculations, we show our motivations for studying the radiation spectra for these cases in astrophysical background. First we show the recent studies of Weibel instability for magnetic turbulence.

Several particle-in-cell (PIC) simulations of relativistic collisionless shocks have been performed to study the nature of turbulent magnetic fields which are generated near the shock front (e.g., Frederiksen et al. 2004; Kato 2005; Chang et al. 2008; Haugbolle 2010). The

characteristic scale of the magnetic fields is the order of inertial length as predicted by the linear analysis of Weibel instability. Then, the typical scale of the turbulent magnetic field λ_B is written by using a coefficient κ as

$$\lambda_B = \kappa \frac{c}{\omega_{pe}\Gamma}, \quad (3.3)$$

where ω_{pe} is the electron plasma frequency, and Γ is the bulk Lorentz factor of upstream fluid at the shock rest frame. The energy conversion fraction into the magnetic fields

$$\varepsilon_B = \frac{B^2/8\pi}{\Gamma n m_p c^2} \quad (3.4)$$

is $10^{-3} - 0.1$, where $B^2/8\pi$ is energy density of magnetic fields, and $\Gamma n m_p c^2$ is the kinetic energy density of the shell. The Lorentz factor of electrons is similar to Γ , and that κ is typically 10 from the result of PIC simulations, the strength parameter a can be estimated as

$$a = \frac{1}{\sqrt{2\pi}} \kappa \varepsilon_B^{1/2} \sqrt{\frac{m_p}{m_e}} \sim O(1 - 10). \quad (3.5)$$

Thus, the assumption $a \ll 1$ on which jitter radiation and DSR weak random field regime are based is not necessarily valid when we consider the radiation from the relativistic shock region. Therefore, $a \gtrsim 1$ is the most important and necessary to study parameter regions.

Next we discuss the Langmuir turbulence. According to Silva (2006), the strength of Langmuir waves generated at the shock region by two stream instability approaches non-relativistic wave breaking limit $\omega_p \sim \omega_{st}$. We further mention the spatial scale of Langmuir waves. We should neither treat the Langmuir turbulence as a static field nor just an oscillating field. The crossing time can be comparable to the period of the Langmuir waves, because the typical spatial scale is about inertial length c/ω_p , governed by the plasma frequency ω_p (Diekmann 2005). Therefore,

$$\omega_p \sim \omega_{st} \sim \omega_0 \quad (3.6)$$

is supposed to be achieved in the Langmuir turbulence in the shock region. We should clarify the radiation signatures from electrons moving in such turbulences.

Chapter 4

Method of Numerical Calculation

We use Lienard-Wiechert potential directly to calculate the radiation spectra. This method is computationally expensive (see Reville & Kirk 2010), but it does not include any approximation for calculation of the radiation spectra from prescribed trajectory. Therefore, this method is suitable for studying the cases for which any approximations are difficult to adopt.

4.1 Field description

We calculate the radiation spectra for two cases. The one is magnetic turbulence generated by Weibel instability. We treat it as a static field when we calculate the radiation spectra. The variation timescale of the field is determined by the turnover time of an eddy. It is longer than the crossing time of relativistic electron if we assume that the background plasma is subrelativistic. Therefore, we can assume the magnetic field is static.

The other is Langmuir turbulence generated by two stream instability. For Langmuir turbulence, we cannot treat the field as static, because the crossing timescale is longer than the variation timescale of the fields. The typical scale of Langmuir turbulence is about inertial length c/ω_p , and the field oscillates with the plasma frequency ω_p (Diekmann 2005). Therefore we take into account the oscillation of the field for this case.

4.1.1 Magnetic turbulence

The isotropic turbulent magnetic field is generated by using the discrete Fourier transform description as developed in Giacalone & Jokipii (1999). It is described as a superposition of N Fourier modes, each with a random phase, direction and polarization

$$\mathbf{B}(\mathbf{x}) = \sum_{n=1}^N A_n \exp\{i(\mathbf{k}_n \cdot \mathbf{x} + \beta_n)\} \hat{\xi}_n. \quad (4.1)$$

Here, $A_n, \beta_n, \mathbf{k}_n$ and $\hat{\xi}_n$ are the amplitude, phase, wave vector and polarization vector for the n -th mode, respectively. The polarization vector is determined by a single angle $0 < \psi_n < 2\pi$

$$\hat{\xi}_n = \cos \psi_n \mathbf{e}'_x + i \sin \psi_n \mathbf{e}'_y, \quad (4.2)$$

where \mathbf{e}'_x and \mathbf{e}'_y are unit vectors, orthogonal to $\mathbf{e}'_z = \mathbf{k}_n/k_n$. The amplitude of each mode is

$$A_n^2 = \sigma^2 G_n \left[\sum_{n=1}^N G_n \right]^{-1}, \quad (4.3)$$

where the variance σ represents the amplitude of the turbulent field. We use the following form for the power spectrum

$$G_n = \frac{4\pi k_n^2 \Delta k_n}{1 + (k_n L_c)^\alpha}, \quad (4.4)$$

where L_c is the correlation length of the field. Here, Δk_n is chosen such that there is an equal spacing in logarithmic k -space, over the finite interval $k_{\min} \leq k \leq k_{\max}$, where we take $k_{\max} = 100 \times k_{\min}$ and $N = 100$ with $k_{\min} = 2\pi/L_c$ and $\alpha = 11/3$. Since we have no reliable constraint for value of α from observations of high energy astrophysical objects, we adopt the Kolmogorov turbulence $B^2(k) \propto k^{-5/3}$ tentatively, where the power spectrum has a peak at k_{\min} . Then we define a parameter which parametrizes the radiation spectra using σ and k_{\min} as

$$a \equiv \frac{e\sigma}{mc^2 k_{\min}} = \frac{\omega_{\text{st}}}{\omega_0}, \quad (4.5)$$

where $\omega_{\text{st}} \equiv e\sigma/mc$ and $\omega_0 \equiv k_{\min}c$. We call ω_{st} "strength omega", which is identical to nonrelativistic cyclotron frequency, and ω_0 "spatial omega". The strength omega ω_{st} accounts

for the effect of the field strength to the radiation spectra. It is from the curvature of orbit and beaming effects for the relativistic particles. When a particle has relativistic energy, the radiation is concentrated in the beaming cone with an angle $\sim 1/\gamma$, so the searchlight sweeps the observer in the timescale of $mc/e\sigma = 1/\omega_{\text{st}}$. Therefore, this timescale is independent on the Lorentz factor of the radiating electron. The meaning of ω_{st} is different from the original meaning of cyclotron frequency. Thus, we call it strength omega. The spatial omega ω_0 is the parameter which parametrizes the effect of the spatial fluctuation. Since the electron moves nearly at the light speed, the changing rate of force direction for the electron is $2\pi c/\lambda = \omega_0$. It also affects the radiation spectra. The ratio of ω_{st} to ω_0 , $\omega_{\text{st}}/\omega_0 = a$ parametrizes the field feature for the radiation spectra from the point of view of strength and spatial fluctuation scale.

4.1.2 Langmuir turbulence

For Langmuir turbulence, we use 3D isotropic turbulence. If the Langmuir waves are generated near the shock front, they may be highly anisotropic on the spot. However, we assume the isotropic turbulence for two reasons. First, the Langmuir turbulence in large part of the emission region would be isotropic, since Langmuir waves interact with background ions and form the Kolmogorov type isotropic turbulence (Treumann & Baumjohan 1997). Second, the radiation spectra for 3D and 1D turbulence are not so different except for a particular case that the direction of radiating electrons and the wavevector is parallel, i.e., when the radiation is linear acceleration emission. However, the perpendicular acceleration emission is dominated as long as the direction slightly differs from the wavevector direction, since the electric field vector is parallel to the wavevector for Langmuir wave. If the shock is ultra-relativistic, the downstream plasma may be relativistically hot. However, we assume the mildly relativistic shock in this thesis, and therefore the plasma in the emission region is subrelativistic, and ignore the thermal velocity of background plasma in the dispersion relation of Langmuir waves $\omega^2 = \omega_p^2 + 3/2 k^2 v_{\text{e,th}}^2$. Thus, we use the propagating Langmuir waves with the same frequency

ω_p .

We generate 3D isotropic Langmuir turbulence by using Fourier transform description, which is slightly modified from the description for magnetic turbulence, because the Langmuir wave is a longitudinal wave. It is described by superpositions of N Fourier modes, each with random phase, and direction

$$\mathbf{E}(x) = \sum_{n=1}^N A_n \cos\{(\mathbf{k}_n \cdot \mathbf{x} - \omega_p t + \beta_n)\} \frac{\mathbf{k}_n}{|\mathbf{k}_n|} \quad (4.6)$$

Here, A_n , β_n , \mathbf{k}_n , and ω_p are the amplitude, phase, wave vector, frequency of the n th mode, respectively. The definition of amplitude A_n is written in the same manner as the case of the magnetic turbulence. We use 10^3 Fourier modes for Langmuir turbulence, and $k_{\min} = 2\pi/L_c$, $\alpha = 9/2$ and k_{\max} is chosen $10^3 k_{\min}$ or $10k_{\min}$. It has a peak at k_{\min} and the spectral index is the one for 3-dimensional isotropic Langmuir turbulence. Then we define two parameters which characterize radiation spectra for Langmuir turbulence. The one is a , which is well known as the strength parameter. It means the Lorentz factor of an electron which is accelerated along the electric field on the spatial scale $2\pi/k_{\min}$. For $\gamma \gg 1$, the acceleration is almost perpendicular to the velocity. Therefore, the local curvature radius of the orbit suffering from perpendicular acceleration by the electric field is $\sim \gamma mc^2/(e\sigma)$. We can use the strength parameter a in the same way as the case of the magnetic turbulence. The other is the ratio of the frequency of the Langmuir waves to ω_0 ,

$$b \equiv \frac{\omega_p}{k_{\min} c} = \frac{\omega_p}{\omega_0}. \quad (4.7)$$

For $b \gg 1$, the force direction changes with frequency ω_p for all electrons. For $b \ll 1$, a change of the force direction is mainly from the spatial fluctuation. Summarizing above, although there are three parameters of the turbulent field $(\omega_0, \omega_{st}, \omega_p)$, we can reduce them to two parameters of (a, b) when our interest is on the spectral signature. We investigate the spectral features in the parameter plane of (a, b) .

4.2 Equation of motion and radiation spectra

For the case of the magnetic turbulence, we inject isotropically 32 monoenergetic electrons with $\gamma = 10$ in the prescribed magnetic fields, and solve the equation of motion

$$\gamma m_e \dot{\mathbf{v}} = -e\boldsymbol{\beta} \times \mathbf{B} \quad (4.8)$$

using 2nd order Runge-Kutta method. We neglect radiation back reaction of the electrons, because the back reaction force is much smaller than the force $\sim eB$ in equation 4.8 for the physical parameters we use. We pursue the orbit of electrons up to the time $300 \times T_g$, where T_g is the gyro time $T_g = 2\pi\gamma mc/e\sigma$. It is much longer than the Photon Formation Time of lowest frequency of the radiation spectra we calculate. The PFT is defined by the coherence time for forming the photons (Reville & Kirk 2010, Akhiezer & Shul'ga 1987).

For the case of Langmuir turbulence, we inject $10^2 - 10^3$ monoenergetic electrons with Lorentz factor $\gamma_{\text{init}} = 10$ into the generated turbulent field. The initial velocity is randomly chosen to achieve an isotropic distribution. Next we solve the equation of motion

$$\frac{d}{dt}(\gamma m \mathbf{v}) = -e\mathbf{E}, \quad (4.9)$$

by using the method which has second order accuracy for each time step. We also neglect radiation back reaction for this case. We pursue the orbits of electrons up to 100 times of PFT for the peak frequency photons for this case. The electrons get energy in the Langmuir turbulence from the parallel (to the velocity) component. Spectral broadening due to finite integration time of particle orbit is inevitable. To compromise the accurateness and computational practice, we choose the integration time as $100 \times$ PFT of the peak frequency. As we see in the section 6, PFT for the peak frequencies of the spectra is the one of the typical timescales of $1/\omega_0$, $1/\omega_{\text{st}}$, and $1/\omega_p$. We choose a suitable one for each spectrum. It is sufficiently long to resolve the spectral shape in the low frequency regions. Moreover, it is not too long to calculate the instantaneous radiation spectra. If we pursue electrons much longer time than the PFT, the radiation spectra correspond to an integrated spectrum of photons emitted over

much longer time with changing energy. It can be understood by superposing the effects of instantaneous spectra and electron acceleration. When we do not obtain the instantaneous spectra, we can not discern which of them determines the spectral features. Therefore, in this thesis we concentrate on instantaneous spectra.

We calculate the radiation spectra using the acceleration, velocity, and position of electrons. The energy dW emitted per unit solid angle $d\Omega$ (around the direction \mathbf{n}) and per unit frequency $d\omega$ to the direction \mathbf{n} is computed as

$$\frac{dW}{d\omega d\Omega} = \frac{e^2}{4\pi c^2} \left| \int_{-\infty}^{\infty} dt' \frac{\mathbf{n} \times [(\mathbf{n} - \boldsymbol{\beta}) \times \dot{\boldsymbol{\beta}}]}{(1 - \boldsymbol{\beta} \cdot \mathbf{n})^2} \exp\left\{i\omega\left(t' - \frac{\mathbf{n} \cdot \mathbf{r}(t')}{c}\right)\right\} \right|^2, \quad (4.10)$$

where $\mathbf{r}(t')$ is the electron trajectory, t' is retarded time (Jackson 1999). Since we have not any specific constraints for a and b which are realized in the high energy astrophysical object, we sweep wide parameter range of a for magnetic turbulence, and both of a and b for Langmuir turbulence, and study the radiation features.

Chapter 5

Magnetic Turbulence

We investigate the radiation spectra for $1 \lesssim a \lesssim \gamma$. In §5.1 we describe numerical results. In §5.2 we give a physical interpretation. In section 5.3, we summarize this chapter.

5.1 Results

First, we show the radiation spectrum for $a = 3/2\pi$ in Figure 5.1. The frequency is normalized by the fundamental frequency $\omega_g = e\sigma/(\gamma mc)$, and the magnitude is arbitrarily scaled. The jagged line is the calculated spectrum, while the straight line drawn in the low frequency region is a line fitted to a power law spectrum. The fitting is made in the range of $1 - 350\omega_g$ and the spectral index turns out to be 0.44. The straight line drawn in the high frequency region shows a spectrum of $\propto \omega^{-5/3}$ expected for diffusive synchrotron radiation for reference (Toptygin & Fleishman 1987). The spectrum is well described by a broken power law, and the spectral index of the low energy side is harder than synchrotron theory predicts. The peak frequency of this spectrum is located at around $10^3\omega_g$. This frequency corresponds to approximately the typical frequency of synchrotron radiation $\omega_{\text{syn}} = 3\gamma^2 e\sigma/2mc \sim 10^3\omega_g$, for $\gamma = 10$.

Figure 5.2 shows the spectrum for $a = 5/2\pi$. The spectral shape changes from that of $a = 3/2\pi$ in both sides of the peak. The spectrum of the low frequency side becomes a broken

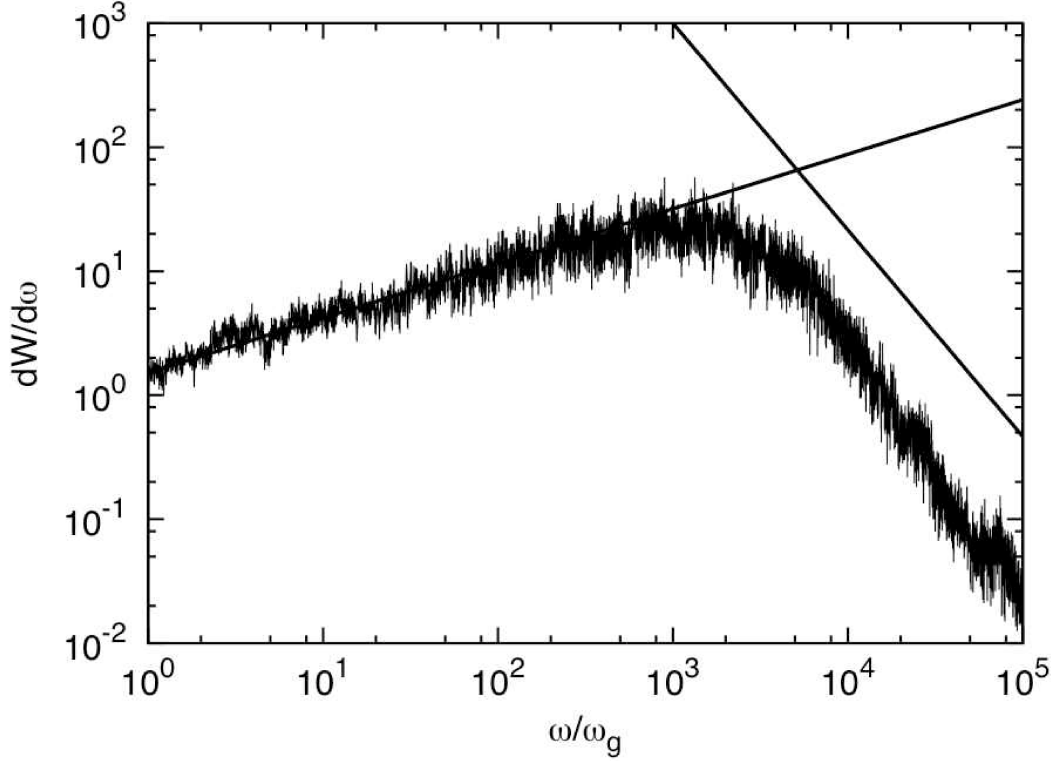


Figure 5.1: Radiation spectrum for $a = 3/2\pi$, $\alpha = 11/3$ and $\gamma = 10$. The straight line in the low frequency region shows a power law spectrum with an index 0.44. The straight line in the high frequency region is $dW/d\omega \propto \omega^{-5/3}$ for reference. Power law index of the low frequency spectrum is harder than the synchrotron theory predicts.

power law with a break around $10\omega_g$, above which the spectrum is fitted by a power law with an index of 0.33, as expected for synchrotron radiation, while below the break the index is 0.58. The high frequency side above the peak indicates an excess above a power law spectrum $dW/d\omega d\Omega \propto \omega^{-5/3}$. It looks like an exponential cutoff. The whole spectrum is described by a superposition of a synchrotron spectrum and a DSR broken power law spectrum. This spectral shape is totally novel and is different from the one by described Fleishman (2010). He reported that the spectrum is described by broken power law in the same range of a as this

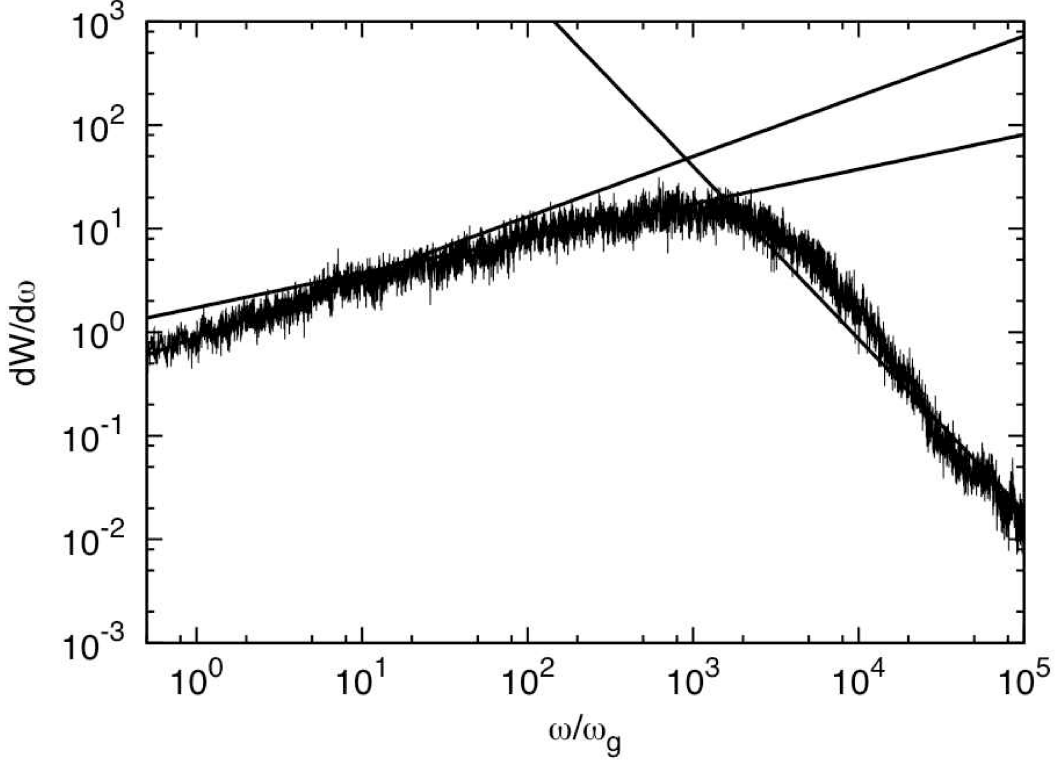


Figure 5.2: Radiation spectrum for $a = 5/2\pi$, $\alpha = 11/3$ and $\gamma = 10$. Two straight lines drawn in low frequency region are fitted one to a power law spectrum in the range of $0.5 - 10\omega_g$ and $10 - 10^3\omega_g$, respectively. The power law index is 0.58 and 0.33. The latter corresponds to the synchrotron radiation. The straight line in the high frequency region is $dW/d\omega \propto \omega^{-5/3}$, and we see a broad hump in the peak region, which is identified with the synchrotron spectrum with an exponential cutoff.

work ($1 < a < \gamma$, $a \sim 10^2$ and $\gamma \sim 10^3$) (Fleishman 2010).

To confirm our inference we calculate the case of $a = 7/2\pi$, for three different values of α , i.e., $\alpha = 14/3$, $11/3$ and $8/3$ and the results are shown in Figure 5.3. The curved black line is a theoretical curve of synchrotron radiation, and three straight black lines are $dW/d\omega d\Omega \propto \omega^{-2/3}$, $\omega^{-5/3}$ and $\omega^{-8/3}$ expected for DSR theory for reference. The green line

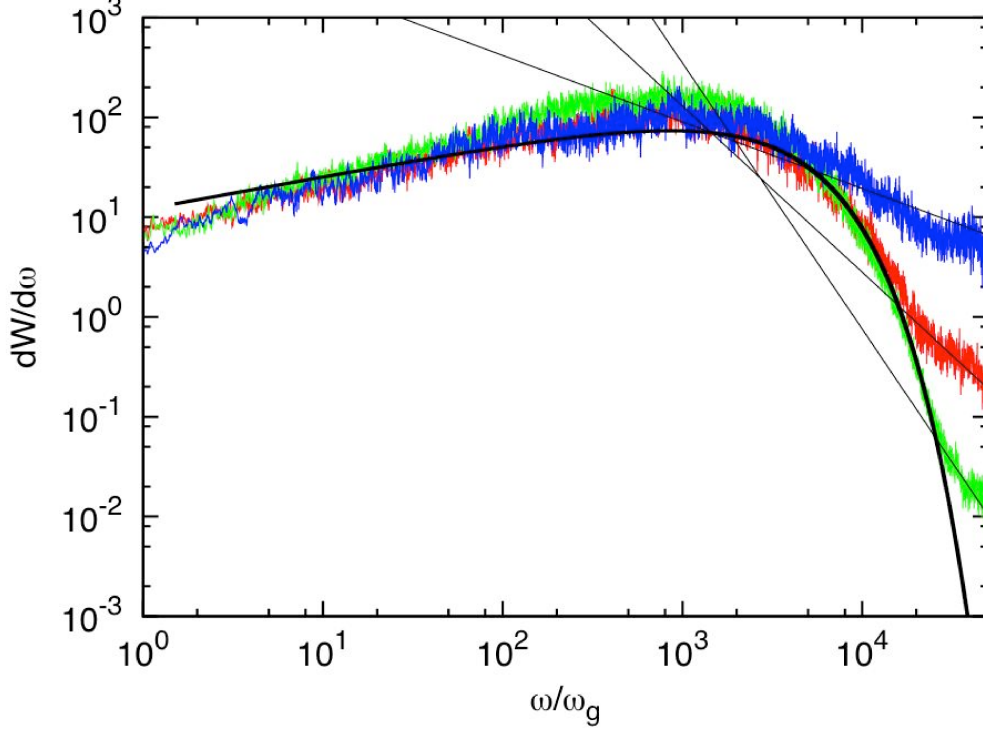


Figure 5.3: Radiation spectra for $a = 7/2\pi$ and $\gamma = 10$, with $\alpha = 14/3, 11/3$ and $8/3$. Green, red and blue lines are calculated spectra $\alpha = 14/3, 11/3$ and $8/3$, respectively. Straight black lines are $dW/d\omega \propto \omega^{-\alpha+2}$. Curved black line is a theoretical curve of synchrotron radiation. We see effects of different spectrum of the turbulent magnetic fields in high energy region.

corresponding to $\alpha = 14/3$ reveals a clear exponential cutoff, and reveals DSR component in only the highest frequency region. The power law index of this component in the highest frequency region coincides with the expected value $-\alpha + 2 = -8/3$. The red and blue lines correspond to $\alpha = 11/3$ and $8/3$, respectively. They indicate a common feature to the green one.

5.2 Interpretation

We give a physical explanation of the spectra obtained in the previous section. At first, we interpret the broken power law spectrum for $a = 3/2\pi$ by using DSR theory. Next, we consider physical interpretation of the complex shape of radiation spectrum for $a = 5/2\pi$ and $a = 7/2\pi$. Finally, we compare our work with previous studies.

To begin with, we review the spectral feature of DSR based on the non-perturbative approach for $a < 1$ (Fleishman 2006). The typical spectrum takes a following form: $dW/d\omega d\Omega \propto \omega^{1/2}$ in the low frequency region, $\propto \omega^0$ in the middle frequency region, and $\propto \omega^{-\alpha+2}$ in the high frequency region. The low frequency part and the middle frequency part are separated at $\omega_{\text{LM}} \sim a\omega_{\text{syn}}$. This spectral break corresponds to the break of the straight orbit approximation due to the effect of multiple scattering (Fleishman 2006). On the other hand, the middle frequency part and the high frequency part are separated at the typical frequency of jitter radiation $\omega_{\text{MH}} = \omega_{\text{jit}}$ which is estimated by using the method of virtual quanta as $\omega_{\text{jit}} \sim \gamma^2 k_{\text{min}} c \sim a^{-1} \omega_{\text{syn}}$ (Medvedev 2000, Rybicki & Lightman 1979). Then, for $a \sim 1$, $\omega_{\text{LM}} \sim \omega_{\text{MH}}$ is achieved and the middle region may vanish. The spectrum for $a \lesssim 1$ becomes a broken power law with only one break, which is located at roughly the synchrotron frequency ω_{syn} . The power law index of low frequency side is ~ 0.5 (which is harder than synchrotron radiation), and that of high frequency side is $-\alpha + 2 = -5/3$. Thus, the spectral feature for $a = 3/2\pi$ can be explained by an extrapolation of DSR non-perturbative approach for $a < 1$, if we consider that the middle frequency region is not conspicuous. Although our spectral index 0.44 slightly differs from 0.5 for DSR, this index is still harder than the synchrotron theory. The situation $a \sim 1$ can be achieved at the internal shock region of GRB, so that this may be responsible for harder spectral index than synchrotron observed for some GRBs.

Next we interpret the spectral features for $a = 5/2\pi$ and $7/2\pi$. The conceptual diagram of these spectra for $1 < a < \gamma$ is depicted in Figure 5.4, and a schematic picture of an electron trajectory is depicted in Figure 5.5. We explain the appearance of another break in the low

frequency range seen at around $10\omega_g$ in Figure 5.2. On the scale smaller than λ_B , the electron motion may be approximated by a helical orbit, while it is regarded as a randomly fluctuating trajectory when seen on scales larger than λ_B . Therefore, for the former scale, we can apply the synchrotron approximation to the emitted radiation. The beaming cone corresponding to the frequency ω is given by

$$\theta_{\text{cone}} = \frac{1}{\gamma} \left(\frac{3\omega_{\text{syn}}}{\omega} \right)^{1/3} \quad (5.1)$$

(Jackson 1999). The deflection angle θ_0 of the electron orbit during a time λ_B/c is estimated to be $\theta_0 = a/\gamma$ from the condition

$$\frac{\gamma\lambda_B}{a}\theta_0 = \lambda_B \quad (5.2)$$

as seen in Figure 5.5. Thus, the synchrotron theory is applicable only for $\theta_{\text{cone}} < \theta_0$, so that the break frequency is determined by $\theta_0 = \theta_{\text{cone}}$, and we obtain

$$\omega_{\text{br}} \sim a^{-3}\omega_{\text{syn}}. \quad (5.3)$$

This break frequency is the same as obtained by Medvedev (Medvedev 2010). We understand that as a is larger, break frequency becomes lower, and when a is comparable to γ , ω_{br} coincides with the fundamental frequency $e\sigma/\gamma mc$.

Next, we discuss on the high frequency radiation, which results from the electron trajectory on scales smaller than λ_B . The synchrotron theory applies between $\lambda_B/a = r_g/\gamma$ and λ_B . However, we should notice that electron motion suffers from acceleration by magnetic turbulence on scales smaller than λ_B/a . The trajectory down to the smallest scale of $2\pi/k_{\text{max}}$ is jittering, which is attributed to higher wavenumber modes as seen in the zoom up of Figure 5.5. If the field in this regime is relatively weak, i.e., α is relatively large (Figure 5.3, green line: $\alpha = 14/3$), the trajectory on the scale smaller than λ_B/a does not much deviate from a helical orbit. In this case, radiation spectrum reveals an exponential cutoff, and a power law component appears only in the highest frequency region. On the contrary, if the smaller scale field is relatively strong, as in the case of $\alpha = 8/3$ depicted in the blue line in Figure 5.3, the power law component becomes predominant in the high frequency region, and the synchrotron

exponential cutoff is smeared out. The intersection frequency of curved black line and straight black lines at around $10^3\omega_g$ in Figure 5.3 corresponds to ω_{jit} as seen in Figure 5.4. Since the intersection frequency is determined by a , the frequency where the power law component appears over the synchrotron cutoff is dependent on α . The excess from the theoretical curve in the middle frequency region in Figure 5.3 may be explained by consideration of two effects. One is the contribution of hidden DSR component, and the other is a range of synchrotron peak frequency which is caused by a fluctuation of magnetic field intensity.

Fleishman reported that the spectrum for $1 < a < \gamma$ and $3 < \alpha < 4$ becomes a broken power law (Fleishman & Urtiev 2010). Medvedev asserted that the high frequency region of the spectrum reveals an exponential cutoff for $1 < a < \gamma$ (Medvedev 2010). Our result indicates that an exponential cutoff plus an extra power law component appears, which is different from Fleishman's remark and from Medvedev's remark on the high frequency region. On the other hand, similar spectra to ours have been reported in Fleishman (2005) and Reville & Kirk (2010) when a uniform field is added to turbulent field. Because the high energy power law component arises from a turbulent spectrum over the wavenumber space, this component does not exist when the small scale field is excited only in a narrow range of wavenumber space. Since the energy cascade of turbulent magnetic fields should exist at least to some degree, we regard that the higher wavenumber modes naturally exist. It depends on the set of parameters of σ and k_{max} whether this high energy power law component can be seen or not. If $2\pi e\sigma/mc^2k_{\text{max}} > 1$, this component will not be seen. If the magnetic turbulence is excited by Weibel instability at the relativistic shocks, it is not possible for k_{max} to be much larger than k_{min} because the wavelength of injection ($\lambda_B = 2\pi/k_{\text{min}}$) is only a few ten times the skin depth at most. Therefore, the component will not be seen for $a \gg 1$ while for $a \sim O(1)$, this power law component will be seen.

As for the frequency region lower than the break frequency $\omega_{\text{br}} = a^{-3}\omega_{\text{syn}}$, Medvedev remarked that the spectrum is similar to small angle jitter radiation (Medvedev 2010). However, it remains to be open if it is so for $1 < a < \gamma$, because the assumption that the straight orbit

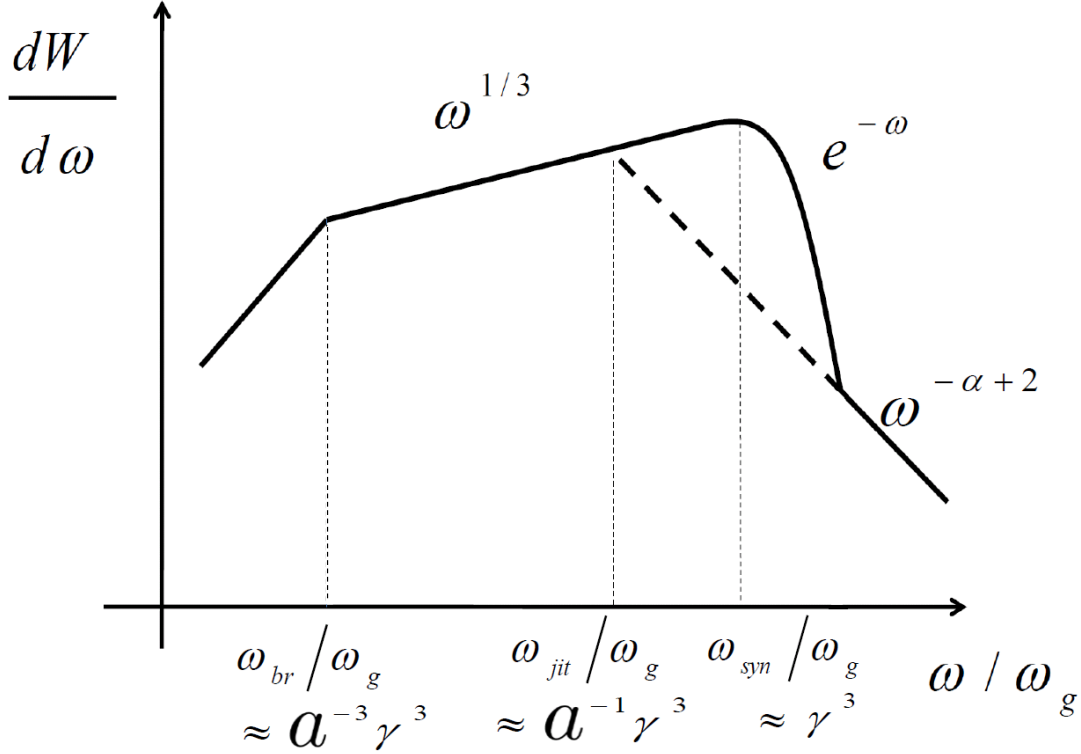


Figure 5.4: Conceptual diagram of the radiation spectrum for $5 \leq a < \gamma$.

approximation of radiating particle is broken. To predict the exact radiation spectrum of the frequency region lower than the break frequency, it is necessary to pursue the particle orbit to follow the long term diffusion which is a formidable task.

5.3 Summary

We calculate the radiation spectrum from relativistic electrons moving in the small scale turbulent magnetic fields by using the first principle calculation utilizing the Lienard-Wiechert potential. We concentrate our calculation on a range of the strength parameter of $1 < a < \gamma$. We confirm that the spectrum for $a = 3/2\pi$ is a broken power law with an index of low energy

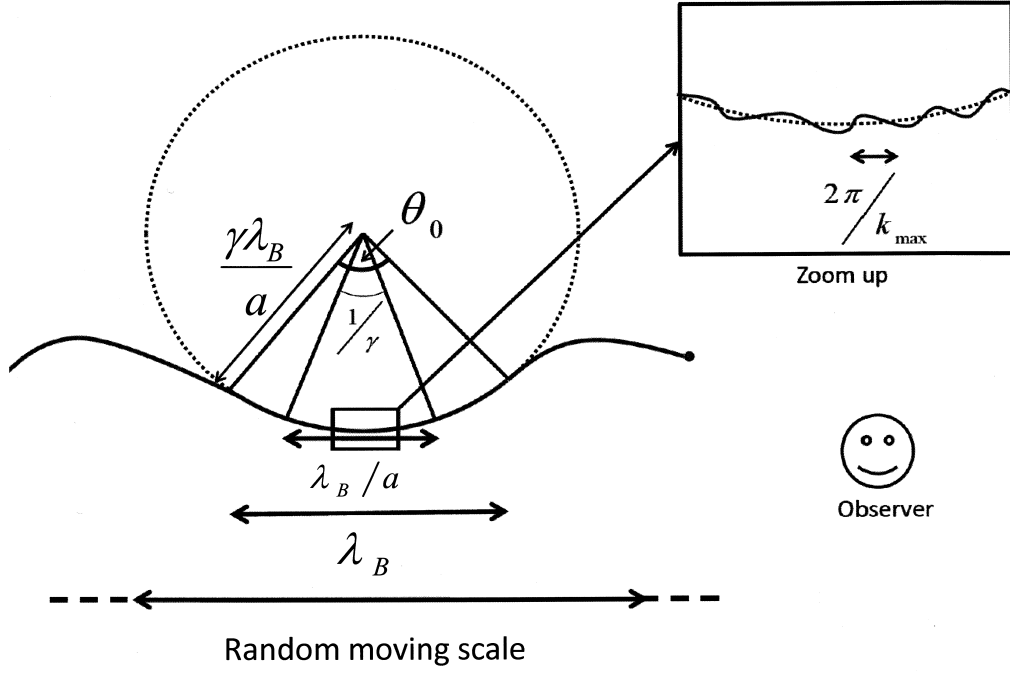


Figure 5.5: Cartoon showing the electron trajectory for $1 < a < \gamma$. The radius of the guiding circle is the Larmor radius $r_g = \gamma \lambda_B / a$. Low frequency photons are emitted from the motion on scales larger than λ_B , while middle frequency ones from that on the intermediate scale between λ_B / a and λ_B are basically synchrotron radiation. The spectral break at $a^{-3} \gamma^3$ in Figure 5.4 corresponds to the break of synchrotron approximation at the scale of λ_B . The scale $\lambda_B / a = r_g / \gamma$ corresponds to the synchrotron peak frequency. On the smallest scale down to $2\pi / k_{\max}$, the trajectory is approximately straight, and jittering is responsible for the power law component in the highest frequency region in Figure 5.4.

side ~ 0.5 , and that some GRBs with low energy spectral index harder than synchrotron theory predicts may be explained. Furthermore, we find that the spectrum for $a = 7/2\pi$ takes a novel shape described by a superposition of a broken power law spectrum and a synchrotron one. Especially, an extra power law component appears beyond the synchrotron cutoff in the high frequency region reflecting magnetic field fluctuation spectrum. This is in contrast with previous works (Fleishman & Urtiev 2010, Medvedev 2010). Our spectra for $a = 5/2\pi$ and $a = 7/2\pi$ are different from both of them. We have given a physical reason for this spectral feature. This novel spectral shape may be seen in various other scenes in astrophysics. For example, the spectrum of 3C273 jet at the knot region may be due to this feature (Uchiyama et al. 2006).

Chapter 6

Langmuir Turbulence

In this chapter, we investigate the radiation spectra for a wide range of the field parameters of Langmuir turbulences. By sweeping the parameter plane of a and b , we obtain general signatures of the radiation spectra. In section 6.1, we show the numerical results. In section 6.2, we give the physical interpretations of the discovered spectral features using radiation for a spatially uniform plasma oscillation. In section 6.3, we make a summary and some discussions.

6.1 Results

6.1.1 Short wavelength regime

First, we show the radiation spectra for $b = \omega_p/\omega_0 \ll 1$ (Figure 6.1), i.e., for the situation where typical spatial scale is shorter than the inertial length. We set $a = 0.1$ to 20, and fix $b = 10^{-2}$; specifically we set $\omega_0 = 1$ and $\omega_p = 10^{-2}$, and change ω_{st} from 0.1 to 20, and take $k_{\max} = 10^3 k_{\min}$. The inequality $b \ll 1$ can be transformed to $\lambda \ll 2\pi c/\omega_p$, which means that the fluctuation scale is much smaller than the inertial length. These fluctuations would be damped by Landau damping and may not be realized in high energy astrophysical objects (Treumann & Baumjohan 1997). However, we cannot reject the possibility that $b \lesssim 1$ is

realized for some time span in relativistic plasmas, so that we study the spectra for $b < 1$. To explore the regime for $b < 1$ clearly, we set an extreme value $b = 10^{-2} \ll 1$. An example of the temporal variation of the Lorentz factor of an electron is depicted in Figure 6.2.

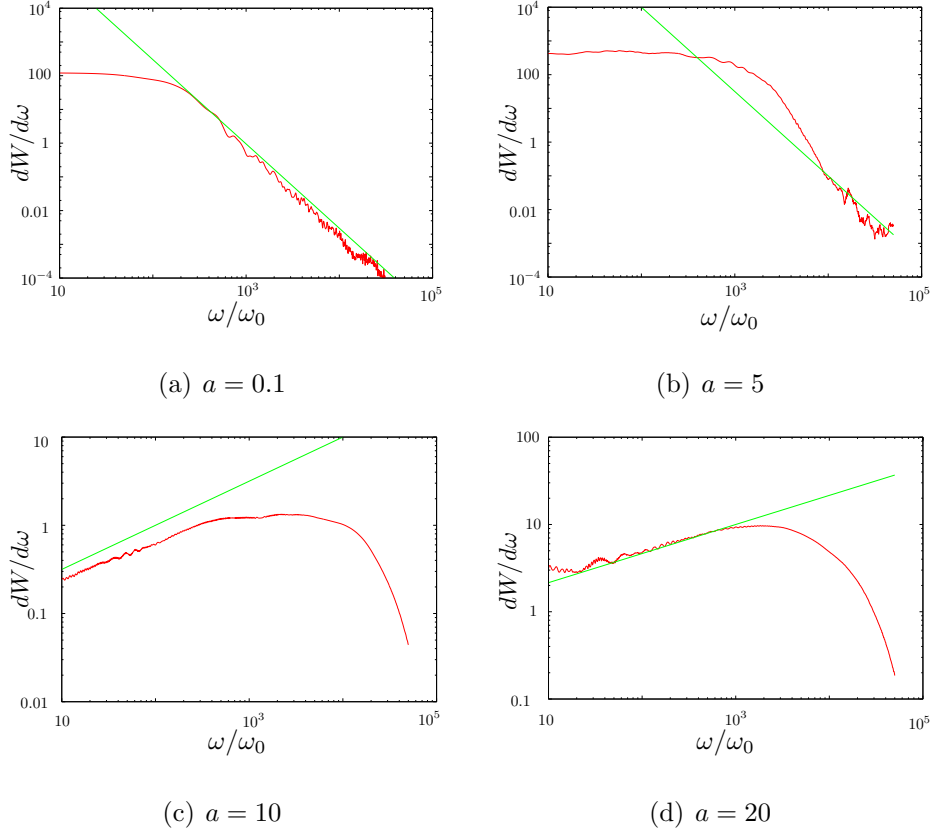


Figure 6.1: Radiation spectra for $b = \omega_p/\omega_0 = 10^{-2}$ and $a = \omega_{st}/\omega_0 = 0.1, 5, 10$, and 20 . Vertical axis is the spectral power in arbitrary unit and horizontal axis denotes frequency ω normalized by ω_0 . The number of electrons used for these calculations is 160. (a) $a = \omega_{st}/\omega_0 = 0.1$, and the straight line shows a power law spectrum with index $-5/2$: (b) $a = 5$, and the straight line shows a power law spectrum with an index $-5/2$: (c) $a = 10$, and the straight line shows a power law spectrum with an index $1/2$: (d) $a = 20$, and the straight line shows a power law spectrum with index $1/3$. We see the transition from jitter radiation regime to the Wiggler radiation regime in Langmuir turbulence (WRL).

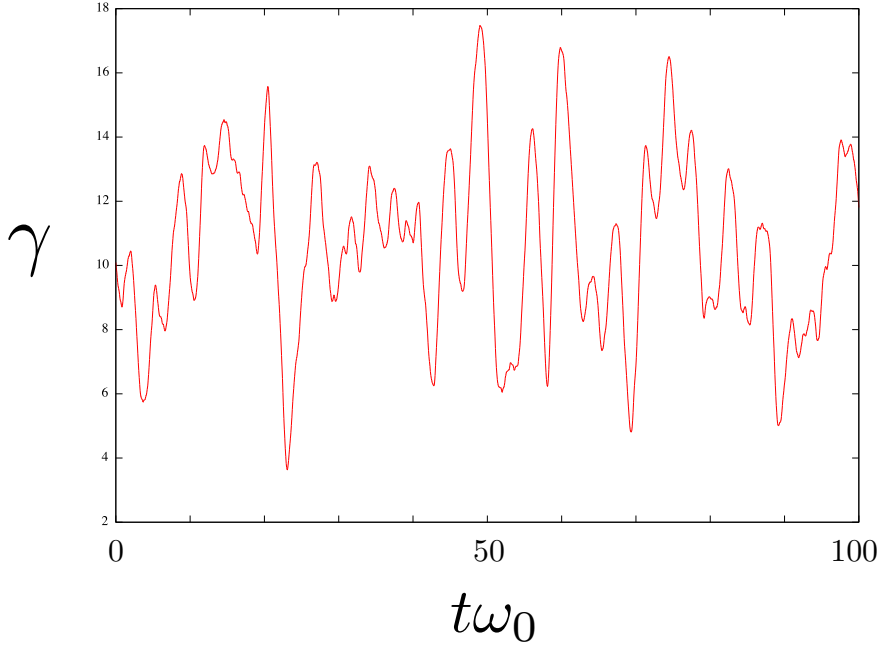


Figure 6.2: An example of the temporal variation of the Lorentz factor of an electron for $a = 5$ and $b = 10^{-2}$ ($\omega_{\text{st}} = 5$, $\omega_0 = 1$, and $\omega_p = 10^{-2}$).

For $a = 0.1$, the low frequency spectrum is as flat as $F_\omega \propto \omega^0$, and there is a break at $\omega \sim 200$, and the spectrum declines with power law $F_\omega \propto \omega^{-5/2}$ in the high frequency region. For $a = 5$, the break frequency becomes higher than that for $a = 0.1$, and the high frequency spectrum deviates from a power law. For $a = 10$, the spectrum in low frequency region becomes hard with an index $\sim 1/2$, and the spectrum in higher frequencies reveals a cutoff feature. For $a = 20$, we see further different features. The spectrum in low frequency side of the peak becomes softer, with the spectral index of about $1/3$, and we see a small deviation from a power law in the lowest frequency region. The features for these spectra can be understood by using the analogy to the radiation theory from the stochastic magnetic field (Medvedev et al. 2011, Teraki & Takahara 2011). Since the wavelength of Langmuir waves for $b \ll 1$ is very short, the oscillation of the electric field can be neglected in the particle crossing time of the wavelength. In fact, $b \ll 1$ is also written by $\lambda/c \ll 2\pi/\omega_p$. The crossing time λ/c corresponds

to the PFT of the typical frequency.

As explained above, we can use the straight analogy to the radiation theory of the stochastic magnetic fields for the radiation spectra from Langmuir turbulence for $b < 1$ by substituting the electric field strength E with magnetic field strength B . For $a < 1$ and $b < 1$, we can use the radiation theories of the DSR and jitter radiation theory (Fleishman 2006, Medvedev 2006). On the contrary, for $a > 1$ and $b < 1$ jitter radiation of strong deflection regime can be applicable (Medvedev et al. 2011, Teraki & Takahara 2011). We call $a < 1$ and $b < 1$ regime as "jitter radiation" regime because the jitter radiation is basically perturbative theory for $a < 1$. We call the radiation for $a > 1$ and $b < 1$ regime as "Wiggler Radiation in Langmuir turbulence", or "WRL" in short. Although the Wiggler radiation is not the radiation mechanism from the stochastic field but that for a fixed field, it has a common picture that the observer is in and off the beaming cone in the course of time.

First, we describe the signature of the radiation spectra of jitter radiation or Diffusive Synchrotron Radiation. The radiation signatures are determined by acceleration perpendicular to the motion, and the observer is always in the beaming cone, which is the same situation as the Langmuir turbulence for $a \lesssim 1$ and $b < 1$. For $a \ll 1$, the spectrum is written by a broken power law $F_\omega \propto \omega^0$ in the low frequency region and $F_\omega \propto \omega^{-\mu+2}$ in the high frequency region. The break frequency is $\sim \gamma^2 \omega_0 = \gamma^2 k_{\min} c$. For $a \sim 1$, while the break frequency remains the same as $\gamma^2 \omega_0$, the multiple deflection effect comes into play in the spectral features near the break frequency. The spectrum in the low frequency region becomes $F_\omega \propto \omega^{1/2}$. Since the multiple deflection makes the angle between observer direction and velocity larger than the beaming cone angle $1/\gamma$, the observer sees the radiation over the timescale which is determined by the deflection condition. Fleishman supposed that the angle changes diffusively. The break frequency of $a\gamma^2\omega_{st}$ is calculated from the angle diffusion (Fleishman 2006). The spectral index of $1/2$ comes from the diffusivity, too.

Next, we describe the signatures for strong deflection regime of $a \gg 1$. For magnetic turbulence, the spectral shape resembles synchrotron radiation in the middle frequency region

and deviations from it would be seen in low frequency region and highest frequency region (Teraki & Takahara 2011). The peak frequency of $\gamma^2\omega_{\text{st}}$ is from the sweeping of the beaming cone on the observer. The picture is same as the synchrotron radiation. For short wavelength regime $\omega_0 \gg \omega_p$ of Langmuir turbulence, the physical picture is the same as this, because the spatial fluctuation dominates the changing rate of the deflection angle. A single deflection angle is $\sim eE\lambda/\gamma mc^2$, which is larger than $1/\gamma$ for $a = \omega_{\text{st}}/\omega_0 = e\sigma/mc^2 k_{\text{min}} > 1$. As a result, the beaming cone sweeps out of the observer within one deflection. The intensity of the radiation off the beaming cone is weak. Therefore, the timescale which sweeps the observer $\sim 1/\omega_{\text{st}}$ corresponds to the PFT of the typical frequency. Considering the photon chasing effect, we get the peak frequency $\sim \gamma^2\omega_{\text{st}}$. The spectral break in the low frequency region would correspond to the deviation from local circular orbit, but the numerical error from finite integration time is also becoming large in the lower frequency region. We do not discuss this point further here, since it is not the main point of contents in this chapter. The power law component in the highest frequency region comes from the smaller scale part of turbulence. It is the same as the spectra of jitter regime. We note here that the power law component in high frequency region cannot be seen for $a = 10$ and $a = 20$. The reason may be as follows. In contrast to the magnetic turbulence, the energy of radiating electrons changes for $a \gtrsim 1$. Therefore, the high frequency region is determined by only the later part of integration time, because the peak frequency is $\sim \gamma^2\omega_{\text{st}}$ for $a > 1$, and the electrons get energy and radiate higher energy photon in later time. The power law component for the highest frequency region in our calculation is hidden by the component that small numbers of electrons with larger energy radiate by Wiggler mechanism.

Finally, we consider effects of the energy change in WRL regime, which is the one of the different points from the magnetic case. Based on an example of the change of Lorentz factor is depicted in Figure 6.2, we estimate the energy change in PFT $1/\omega_{\text{st}}$ for peak frequency. The

PFT is $1/\omega_{\text{st}}$. The change of Lorentz factor is estimated as

$$\Delta\gamma = eE \cdot \frac{c}{\omega_{\text{st}}} \frac{1}{mc^2} \sim 1. \quad (6.1)$$

Therefore, the change of the Lorentz factor in this timescale is smaller than 1. Thus, we do not need to consider the energy change in PFT for peak frequency. However, for sufficiently large a , we have to take it into account for lower frequency spectrum. We calculate the spectra for modest a in this chapter, so we omit this problem. It will be studied in future works.

6.1.2 Long wavelength and weak regime

Next we show the radiation spectra for $a < 1$ and $b > 1$ (Figure 6.3), i.e., a situation where long wavelength turbulence with weak amplitudes dominates; the spectra for $b = 0.1$ and 1 are also depicted for comparison. An example of the temporal variation of the Lorentz factor of an electron is depicted in Figure 6.4. Firstly, we consider the meaning of the parameters of $a < 1$ and $b > 1$, which correspond to $\omega_p > \omega_0 > \omega_{\text{st}}$. In this regime, the changes of the direction of acceleration are mainly due to wave oscillation, rather than the spatial fluctuations because the crossing time is longer than the oscillation time. Moreover, $\theta_{\text{def}} < 1/\gamma$ is derived from $b > a$. Therefore, we can regard the orbit as straight in the time scale of plasma oscillation $1/\omega_p$. The condition $b > 1$ can be transformed to $\lambda > 2\pi c/\omega_p$, which means that the inertial length is shorter than the wavelength. Therefore, this regime is likely to occur in the astrophysical objects.

We set $\omega_0 = 1$, $\omega_{\text{st}} = 10^{-2}$ and change ω_p from 0.1 to 10, so that $a = 10^{-2}$ and $b = 0.1$ to 10, and take $k_{\text{max}} = 10^3 k_{\text{min}}$. As was discussed in the previous subsection for $b = 0.1$, the spectrum shows jitter radiation signature. The peak frequency is $\gamma^2 \omega_0$ and $F_\omega \propto \omega^0$ in the low frequency region, and $F_\omega \propto \omega^{-5/2}$ above the peak frequency reflecting the spectrum of the turbulent electric field $E^2(k) \propto k^{-5/2}$. As b becomes larger, the peak shifts to higher frequency. For $b = 10$, the peak frequency is $\sim 10^3$, which is identified with $\gamma_{\text{init}}^2 \omega_p$. The spectral index of low frequency side is ~ 1 . This feature coincides with the result of DRL theory (Fleishman 2006).

We call this regime "DRL regime". The DRL theory predicts the spectral shape for $a < 1$ and $b > 1$ as follows. The peak frequency is $2\gamma^2\omega_p$ with an abrupt cutoff in the higher frequency side and a power law component emerges in the highest frequency region for $k_{\max} \gg \omega_p/c$. In the low frequency side, the spectrum becomes $F_\omega \propto \omega^1$.

The peak frequency is determined by the time scale of plasma oscillation. The shortest timescale of the electron motion is $1/\omega_p$, and the observer located along the initial velocity direction can see this radiation, because the orbit is regarded as straight in this time scale as we showed above. We consider Doppler boosting, and we get the peak frequency $2\gamma^2\omega_p$ in the observer frame. The origin of the power law component in the highest frequency region is same as jitter radiation. The hard spectral index in the frequency region lower than peak of 1 is from the effect of the electrons which have the same oscillating frequency ω_p move different angles to the observer (Fleishman 2007a,b). It is regarded as the emission spectrum from an electron integrated over the solid angle, which can be understood in an analogy to the Undulator theory (Jackson 1999), although the force direction changes in this case not spatially but temporally. When the particle mean velocity and the wavenumber are fixed, that makes no difference for the radiation spectra. The peaky shape of the spectra is the most remarkable feature of the spectra for DRL case. A difference is that the wave number is a vector, while the frequency is a scalar. For DSR, the electron feels spatial fluctuation with wavenumber along the velocity $\mathbf{k} \cdot \mathbf{v}/v$, therefore the low frequency spectrum becomes flat. On the other hand, for DRL, all electrons feel the same frequency of ω_p for the Langmuir turbulence (c.f. Fleishman & Toptygin 2007a,b, Medvedev 2006).

6.1.3 Long wavelength and strong regime

The remaining interesting regime of $a > 1$ and $b > 1$ has not been well investigated. In this regime temporal variation of the electric field dominates and electron orbits significantly deviate from rectilinear motion. These parameters mean that the wavelength is longer than the inertial length and that the typical scale of PFT is $mc^2/e\sigma$. We set $a = 10^2$, $b = 20$ to 800,

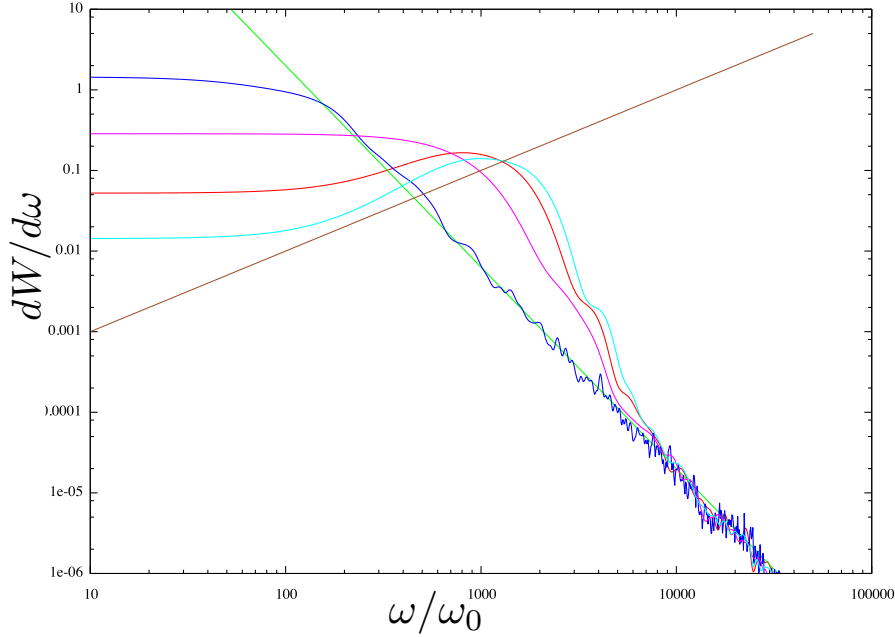


Figure 6.3: Radiation spectra for $a = 10^{-2}$ and $b = 0.1, 1, 5, 7$, and 10 from top to down in low frequency range. The number of electrons used for these calculations is 160. The straight lines show a power law spectrum with index 1 and $-5/2$. We see the transition from jitter radiation to DRL as b increases.

so that $a/b = 0.125$ to 5 , and $\omega_0 = 1$. We set $\omega_{st} = 10^2$, and we change ω_p from 20 to 800 , and k_{max} is chosen to be $10k_{min}$ here. We show the interesting results for $a > 1$ and $b > 1$ (Figure 6.5). An example of energy change for $a = 100$ and $b = 20$ is depicted in Figure 6.6.

We examine two regimes of $a < b$ and $a > b$ separately. For $a < b$, the peak frequency is $\sim \gamma_{init}^2 \omega_p$. The spectral index of low frequency region is 1, and cutoff feature can be seen above the peak. This region is regarded as the DRL regime from these signatures. For $a < b$, i.e., $\omega_{st} < \omega_p$, the particle is not deflected by large angle because the direction of the electric field changes in a time shorter than the time for which the beaming cone sweeps the observer. We set $k_{max} = 10k_{min}$, therefore, a power law component in high frequency region is not seen at all.

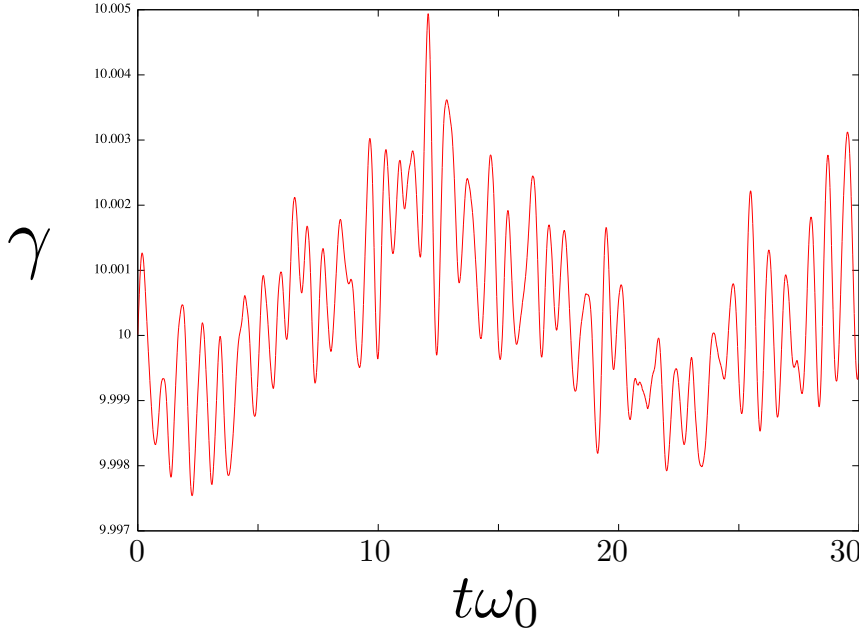


Figure 6.4: An example of the temporal variation of the Lorentz factor of an electron for $a = 10^{-2}$ and $b = 10$ ($\omega_{st} = 10^{-2}$, $\omega_0 = 1$, and $\omega_p = 10$).

On the contrary, different features emerge for $a > b$. The peak frequency becomes larger than $\gamma_{init}^2 \omega_p$. Moreover, the spectra below the peak frequency become softer, the index changes from 1 to $1/3$. The energy change of electrons may cause the change of the peak frequency, but it cannot explain the soft spectrum. Rather, it would be naturally understood that the peak frequency is $\gamma^2 \omega_{st}$ and $F_\omega \propto \omega^{1/3}$ by using the analogy of the Wiggler radiation. We consider that we should use WRL theory not only for $a > 1 > b$, but also for $a > b > 1$, because the deflection angle in one deflection is also larger than $1/\gamma$ for this case. This is in contrast to the DRL theory, which predicts the same spectral signatures for the parameter range of $a > b > 1$ as for $b > a > 1$. According to DRL theory, the peak frequency is $\gamma^2 \omega_p$ even if $a > b$, and the spectral index below the peak is $1/2$. Thus, our numerical calculations reveal new features which have not been known previously for Langmuir turbulence. We ascribe that the parameter regime $a > b > 1$ is in the WRL regime in $a - b$ plane. To clarify the

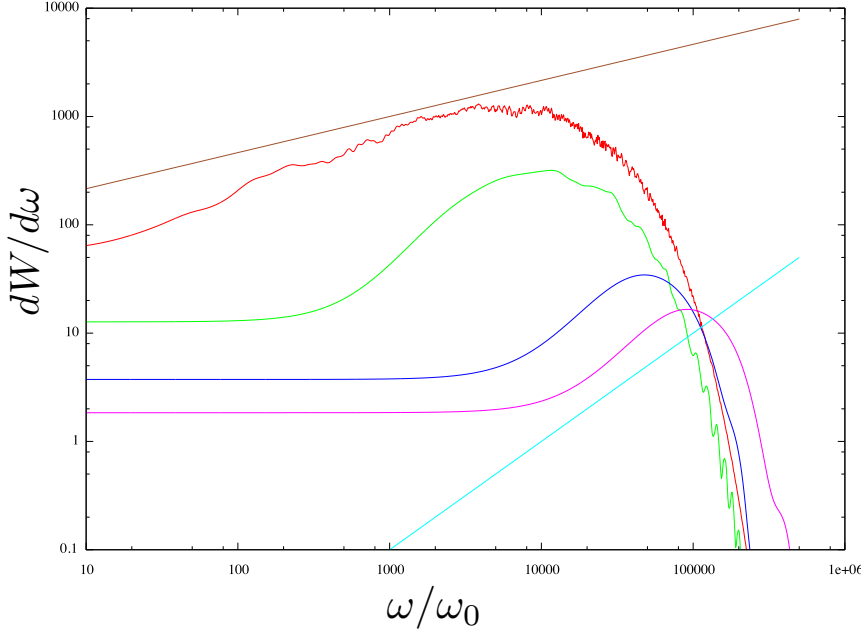


Figure 6.5: Radiation spectra for $a = 10^2$ with $b = 20, 90, 400$, and 800 from top to down. The number of electrons used in these calculations is 800. The straight lines show the power law spectra with index $1/3$ and 1 . We see the transition from the DRL to WRL as b decreases.

spectral features for $a > b > 1$ in more detail, and to confirm our consideration, we examine the radiation from a relativistic electron moving in pure plasma oscillation in the next section.

6.2 Pure plasma oscillation

In this section, we investigate the emission of a relativistic electron suffering from pure plasma oscillation in order to discuss the interpretation of the features of the radiation spectra for $a > b > 1$. To clarify the origin of the peak frequency $\gamma^2 \omega_{st}$, we set a simple configuration of the electric field, where electron motion is deterministic compared to stochastic character in turbulent fields. We calculate the electron velocity analytically and the radiation spectra numerically. By comparing the motion and spectra, we interpret the mechanism which deter-

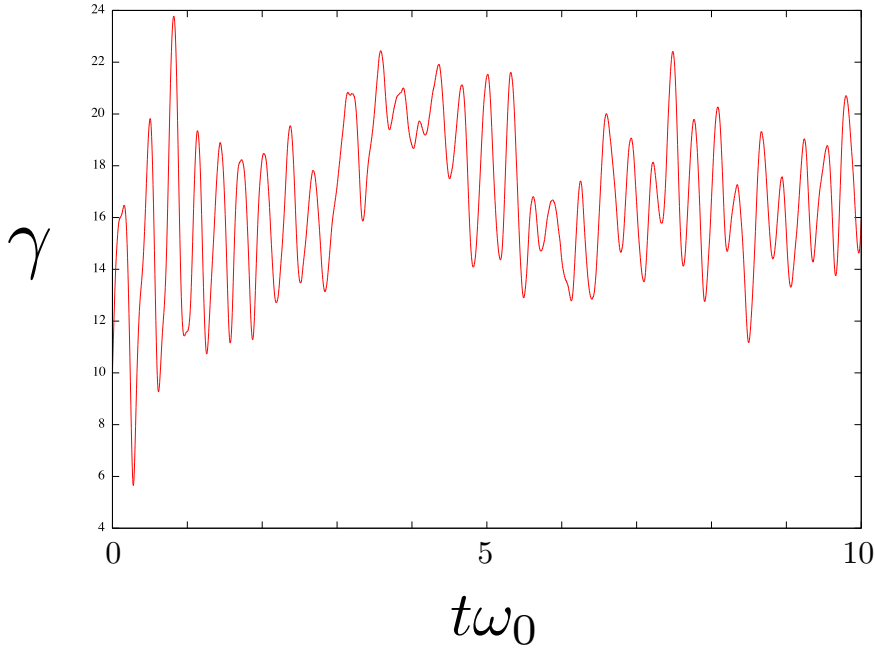


Figure 6.6: An example of the temporal variation of the Lorentz factor of an electron for $a = 10^2$ and $b = 20$ ($\omega_{\text{st}} = 10^2$, $\omega_0 = 1$, and $\omega_p = 20$).

mines the peak frequency. Lastly we consider the radiation spectra from the turbulent field by using these results.

We use a single Langmuir wave which has infinitely large wavelength $k = 0$, in other words, $\omega_0 = 0$. Therefore, it is a pure plasma oscillation. We set $\mathbf{E} = (E_x, 0, 0)$ with

$$E_x = E_0 \cos(\omega_p t). \quad (6.2)$$

We characterize the field by using a single parameter of

$$\eta \equiv \omega_{\text{st}}/\omega_p. \quad (6.3)$$

We inject an electron along the z -axis at $t = 0$ with the initial Lorentz factor γ_{init} and solve the equation of motion (4.9). Therefore, the orbit is determined by γ_{init} and η . Here, we define α for convenience

$$\alpha \equiv \left(\frac{\gamma_{\text{init}}}{\eta} \right)^2. \quad (6.4)$$

This parameter characterizes the motion. Solving the equation of motion, we get the momentum

$$\begin{aligned} p_x &= -\frac{eE_0}{\omega_p} \sin \omega_p t \\ p_z &= \text{const} \end{aligned} \quad (6.5)$$

with $p_z = \gamma_{\text{init}} mc \beta_{\text{init}}$. We note that the z -component of the momentum is constant, but the z -component of the velocity is not constant. The Lorentz factor behaves as

$$\gamma = \eta \sqrt{\alpha + \sin^2 \omega_p t}, \quad (6.6)$$

For $\alpha \gg 1$, the Lorentz factor is always nearly γ_{init} , while for $\alpha \lesssim 1$, the Lorentz factor significantly oscillates. Using these equations, we can write the velocity as

$$\begin{aligned} \beta_x &= -\frac{\sin \omega_p t}{\sqrt{\alpha + \sin^2 \omega_p t}} \\ \beta_z &= \frac{\sqrt{\alpha - \frac{1}{\eta^2}}}{\sqrt{\alpha + \sin^2 \omega_p t}}. \end{aligned} \quad (6.7)$$

Since the velocity is a periodic function, we can define the mean velocity by $\bar{\beta} = \frac{\omega_p}{2\pi} \int_0^{2\pi/\omega_p} \beta_z dz$. In the limit of $\alpha \rightarrow \infty$ the electron motion can be approximated by a harmonic oscillation to the x direction aside from a constant velocity along the z -axis. As α decreases but it still much larger than unity, the motion can be approximated by a figure of eight when the mean motion is subtracted. As α decreases further, the motion becomes increasingly nonlinear. To get a clear view of the motion, it is convenient to transform to the mean velocity frame at the next step. The velocity in the mean velocity frame is given by

$$\begin{aligned} \beta'_x &= -\frac{\eta}{\bar{\gamma}} \frac{\sin \theta}{\eta \sqrt{\alpha + \sin^2 \theta} - \bar{\beta} \sqrt{\gamma_{\text{init}}^2 - 1}} \\ \beta'_z &= -\frac{\sqrt{\gamma_{\text{init}}^2 - 1} - \bar{\beta} \eta \sqrt{\alpha + \sin^2 \theta}}{\eta \sqrt{\alpha + \sin^2 \theta} - \bar{\beta} \sqrt{\gamma_{\text{init}}^2 - 1}}, \end{aligned} \quad (6.8)$$

where $\theta = \omega_p t$. The mean velocity $\bar{\beta}$ cannot be represented elementarily in a general form. Then, we take the parameter $\alpha \ll 1$ and approximate the motion hereafter. We note that

$\alpha \gg 1$ means $\gamma_{\text{init}} \gg \eta$, therefore η can be much larger than 1 when $\gamma_{\text{init}} \gg 1$. We expand the Lorentz factor and the velocity, and get the mean velocity and the mean Lorentz factor in the lowest order of α .

$$\begin{aligned}\bar{\beta} &= \beta_{\text{init}} \left(1 - \frac{1}{4\alpha}\right) \\ \bar{\gamma} &= \frac{\gamma_{\text{init}}}{\sqrt{1 + \frac{\eta^2}{2}}}\end{aligned}\tag{6.9}$$

For $\eta \ll 1$, $\bar{\gamma}$ is similar to γ_{init} , while for $\eta \gg 1$, $\bar{\gamma} = \sqrt{2}\gamma_{\text{init}}/\eta$ is much smaller than γ_{init} . Using this approximated velocity, we calculate the maximum Lorentz factor in the mean velocity frame, to clarify the fact that the radiation signatures depend on η as

$$\gamma'_{\text{max}} = \frac{\gamma_{\text{init}}}{\sqrt{1 + \frac{\eta^2}{2}}} \left[\sqrt{\gamma_{\text{init}}^2 + \eta^2} - \beta_{\text{init}} \left(1 - \frac{1}{4\alpha}\right) \sqrt{\gamma_{\text{init}}^2 - 1} \right].\tag{6.10}$$

For $\eta \ll 1$,

$$\gamma'_{\text{max}} = 1 + \frac{\eta^2}{2}.\tag{6.11}$$

The motion in this frame is non-relativistic, therefore, the radiation in this frame is dipole radiation. On the other hand, for $\eta \gg 1$, the maximum Lorentz factor is

$$\gamma'_{\text{max}} = \frac{3\sqrt{2}}{4}\eta.\tag{6.12}$$

Therefore, the motion is relativistic even in this frame and the radiation spectrum consists of higher harmonics, because β' approaches 1. It should be noted that for $\eta = 1$, the motion in the mean velocity frame is mildly relativistic with Lorentz factor $\gamma'_{\text{max}} = 1.02$, and $\beta' = 1/5$. We can see that the transition from non-relativistic harmonic motion to relativistic motion occurs around $\eta \sim$ a few from this fact.

The trajectory in the mean velocity frame is obtained by integrating the approximated velocity in the original frame over t and by transforming to the mean velocity frame

$$\begin{aligned}x' &= \frac{c}{\sqrt{\alpha}\omega_p} \cos \theta \\ z' &= \sqrt{\frac{\beta_{\text{init}}^2 \eta^2}{32(2 + \beta_{\text{init}}^2 \eta^2)}} \frac{c}{\sqrt{\alpha}\omega_p} \sin 2\theta,\end{aligned}\tag{6.13}$$

where $\theta = \omega_p t$. Basic features of the motion are the same as discussed above in the original frame. However, the parameter which characterizes the motion is not α but η in this frame. The trajectory is a straight line for $\eta \ll 1$ and a figure of eight for $\eta \gtrsim 1$. Next, we discuss the phase of oscillation of the electron to consider the characteristic radiation frequency in the mean velocity frame. The phase θ is written by

$$\theta = \omega_p t = \omega_p \bar{\gamma} (t' + \frac{\bar{\beta}}{c} z'). \quad (6.14)$$

The phase depends on not only t' , but also z' . This phase shift from $\bar{\gamma}\omega_p t'$ is not negligible compared to 2π . It reaches $\sim 1/4$ for $\eta \rightarrow \infty$, even if $\eta = 1$ it is $\sim 1/12$. However, the fundamental oscillation frequency is determined by the period $T = 2\pi/\bar{\gamma}\omega_p$. Since z' is a periodic function and $z' = 0$ for $\theta = 2\pi$ and $\theta = 0$ as seen in equation (6.8). Lastly we note that the phase change rate $d\theta/dt'$ is not constant. Summarizing above, the motion in the mean velocity frame is a simple non-relativistic harmonic motion for $\eta \ll 1$, and relativistic motion on the figure of eight trajectory, and the frequency for both case is $\bar{\gamma}\omega_p$. It should be noted that the velocity is dependent on η and the characteristic radiation frequency changes with η .

Next we show numerically calculated radiation spectra from the electron and their features are interpreted in terms of the properties of the orbit. We fix $\omega_{st} = 1$, and change ω_p to change the parameter η . The observer is on the z -direction. We calculate radiation spectra using much longer integration time than the PFT, because the electron moves perfectly periodically. As a consequence, the spectra show very sharp features, which makes it easier to understand the relation between spectral features and orbit. First, we show the spectrum for $\eta = 10^{-3}$ ($\omega_p = 10^3$, Figure 6.7(a)). We see a sharp peak like a delta function at the frequency $2\gamma_{\text{init}}^2\omega_p = 2 \times 10^5$. This is understood in terms of the motion of the electron in the mean velocity frame. For $\eta \ll 1$, in the mean velocity frame, electron motion is a non-relativistic simple harmonic motion with the frequency $\sim \bar{\gamma}\omega_p$. Therefore, the radiation is the dipole radiation with the frequency of $\bar{\gamma}\omega_p$. Since $\bar{\gamma} \sim \gamma_{\text{init}}$ for $\eta \ll 1$, the radiation frequency in the observer frame is $2\gamma_{\text{init}}^2\omega_p$. Thus, we ascribe the frequency $2\gamma_{\text{init}}^2\omega_p$ in the radiation spectra of perturbative

regime ($\omega_{\text{st}} < \omega_p$) to the Doppler shifted dipole radiation. Next we show the spectrum for $\eta = 0.01$ ($\omega_p = 10^2$, Figure 6.7(b)). We can see the higher harmonics of $2\gamma_{\text{init}}^2\omega_p = 2 \times 10^4$. It is from effects of retarded time, as is clearly seen in the mean velocity frame. However, the effect is very weak, as the power of the second harmonics is about 10^{11} times smaller than the fundamental mode in the frequency resolution of this calculation. The ratio of the power of the second harmonics to the fundamental mode is proportional to β'^2 , so the second harmonics is much smaller than the fundamental mode in this case.

For $\eta \sim 1$, the spectral shape changes significantly. First, the higher harmonics stand more strongly, because β' approaches 1. Many harmonics are as strong as the fundamental mode for $\eta = 1$ (Figure 6.7(c)), and the envelope of the peaks of the harmonics shows an exponential cutoff. We note that the spectrum in the frequency region higher than 5000 comes from numerical error. Second, the frequency of the fundamental mode deviates from $2\gamma_{\text{init}}^2\omega_p$, because the difference between $\bar{\gamma}$ and γ_{init} becomes larger. The mean Lorentz factor $\bar{\gamma}$ is $\sqrt{2/3}\gamma_{\text{init}}$ for $\eta = 1$, thus the frequency of the fundamental mode in the original frame is $2\bar{\gamma}^2\omega_p = 133$. The difference between 133 and $2\gamma_{\text{init}}^2\omega_p = 200$ is small, but we can discern it in Figure 6.7(c). Next we discuss the peak frequency (cutoff frequency) for $\eta > 1$. We show the spectra for $\eta = 1, 3$, and 5 in Figure 6.8. The fundamental frequency is 133 for $\eta = 1$, 12 for $\eta = 3$, and 3 for $\eta = 5$, but the cutoff frequency around a few hundreds does not change. We see the cutoff frequency is not of the fundamental mode, but it is determined by the higher harmonics for $\eta > 1$. The radiation spectra in the observer frame also can be derived by regarding it as a Doppler boosted emission. However, since the mechanism which determines the peak frequency is the same as the Wiggler radiation we can understand the peak frequency more easily by considering the PFT in the observer frame. The condition $\eta = \omega_{\text{st}}/\omega_p > 1$ is equivalent to that PFT of the typical frequency in Wiggler mechanism, where $1/\omega_{\text{st}}$ is shorter than the oscillating time $1/\omega_p$. On the other hand, the Lorentz factor relevant for the peak frequency is not $\bar{\gamma}$, but γ_{init} , because the beaming cone sweeps the observer in the phase around $2n\pi$, where n is a natural number. We note that the change of the Lorentz factor in the time

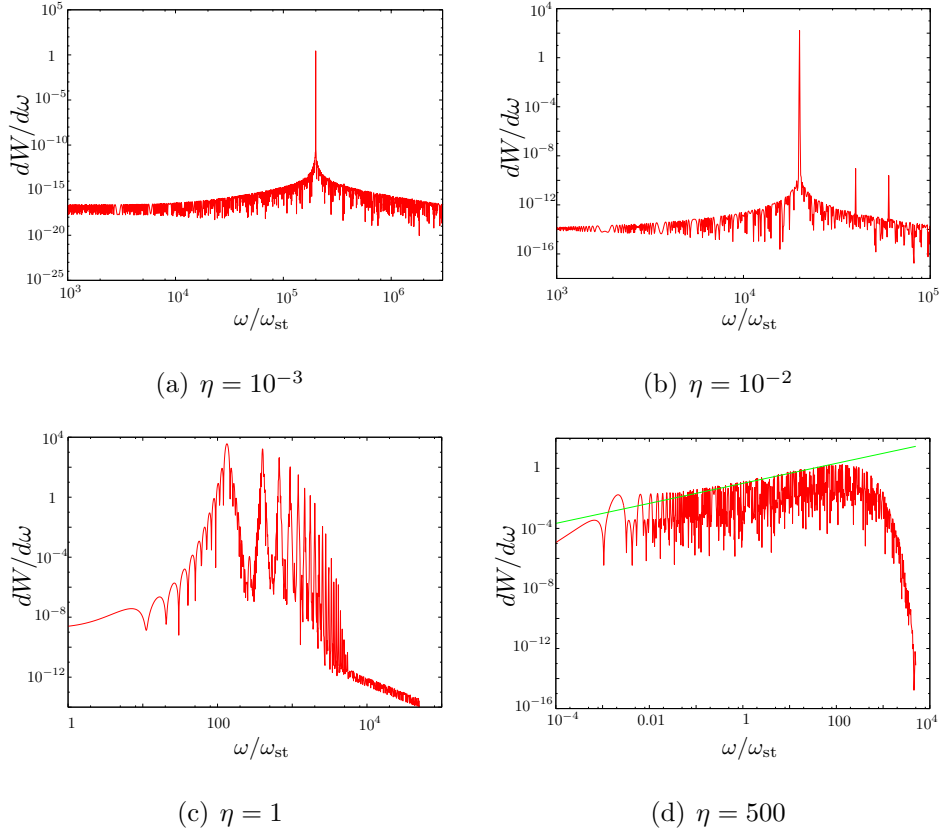


Figure 6.7: Radiation spectrum from an electron with $\gamma_{\text{init}} = 10$ moving in the oscillating field. Horizontal axis is frequency normalized by $\omega_{\text{st}} = 1$. (a) $\eta = \omega_{\text{st}}/\omega_{\text{p}} = 10^{-3}$, ($\omega_{\text{p}} = 10^3$) (b) $\eta = 10^{-2}$, ($\omega_{\text{p}} = 10^2$) (c) $\eta = 1$, ($\omega_{\text{p}} = 1$) (d) $\eta = 500$, ($\omega_{\text{p}} = 2 \times 10^{-3}$), and the straight line shows a power law spectrum with index $2/3$. The fundamental mode in panels (a) and (b) are $\bar{\gamma}^2 \omega_{\text{p}} \simeq \gamma_{\text{init}}^2 \omega_{\text{p}}$, while that in (c) is $\bar{\gamma}^2 \omega_{\text{p}} = 133 < \gamma_{\text{init}}^2 \omega_{\text{st}}$. We see the strong higher harmonics in (c) and (d).

scale of $1/\omega_{\text{st}}$ is 1 at most, as seen in equation (6.1). As a result, the cutoff frequency is $\sim \gamma_{\text{init}}^2 \omega_{\text{st}}$. In this way, we get a clear understanding of the mechanism of the peak frequency shift around $\eta \sim O(1)$.

Here, we compare the results in this section with the radiation spectra obtained in the preceding section. The case of Langmuir turbulence with $a > b > 1$ ($\omega_{\text{st}} > \omega_{\text{p}} > \omega_0$) corresponds to the case of pure plasma oscillation with $\eta > 1$, since $\eta = \omega_{\text{st}}/\omega_{\text{p}}$ and $\omega_0 = 0$ for pure plasma

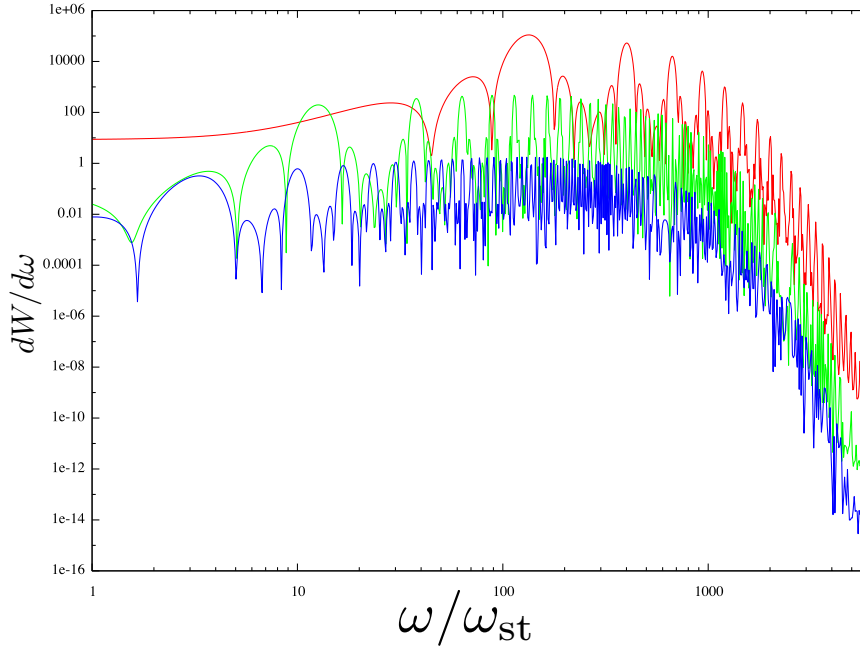


Figure 6.8: Radiation spectra for $\eta = 1, 3$, and 5 ($\omega_p = 1, 1/3$, and $1/5$) from top to down. A factor of 10^2 is multiplied to the spectrum for $\eta = 1$, and 10^{-2} is multiplied for $\eta = 5$. The fundamental frequency is $2\bar{\gamma}^2\omega_p$. It is 133 for $\eta = 1$, 12 for $\eta = 3$ and 3 for $\eta = 5$. The cutoff frequency is a few times of $\gamma_{\text{init}}^2\omega_{\text{st}} = 100$, which does not depend on ω_p explicitly.

oscillation. Moreover, the approximation we used in pure plasma oscillation of $\gamma_{\text{init}} > \eta$ is also applicable for the case of Langmuir turbulence, since $\eta = a/b \leq 5$ and $\gamma_{\text{init}} = 10$ for the spectra shown in Figure 6.5. We have shown that the peak frequency is $\gamma_{\text{init}}^2\omega_{\text{st}}$, and it consists of the higher harmonics of $\bar{\gamma}^2\omega_p$ for pure plasma oscillation with $\eta > 1$. Therefore, the peak frequency for the Langmuir turbulence with $a/b > 1$ in Figure 6.5 is interpreted as $\gamma^2\omega_{\text{st}}$, and it naturally explains the fact that the peak frequency is larger than $\gamma_{\text{init}}^2\omega_p$. We make two more discussions about this issue here, the one is the validity for application of the result for pure plasma oscillation to the case for the Langmuir turbulence, and the other is the Lorentz factor for the peak frequency for the case of Langmuir turbulence. First we discuss the validity for the application of Wiggler mechanism to case of the Langmuir turbulence. Even though the

electric field is turbulent, the electric field does not change over the timescale $1/\omega_{st}$ because the timescale of $1/\omega_{st}$ is the shortest in the three timescales of $1/\omega_{st}$, $1/\omega_p$, and $1/\omega_0$. In other words, the photon formation length of the typical frequency for the Wiggler radiation $\sim c/\omega_{st}$ is shorter than the spatial fluctuation scale $\sim c/\omega_0$ and inertial length $\sim c/\omega_p$. Therefore, the electric field for the radiating electron over the timescale $1/\omega_{st}$ is roughly constant, and the beaming cone sweeps observer in one deflection. As a result, the peak frequency is determined by Wiggler mechanism. Next we discuss the Lorentz factor of electrons which radiate peak frequency. The Lorentz factor of electrons varies with time for the turbulent electric field. Because the integration time for the calculation is 100 times larger than $1/\omega_{st}$, the electron is accelerated chaotically. The peak frequency consists of the superposition of the radiation from the electron in different time. The electron emit the peak frequency photon when the beaming cones sweep the observer, which is realized stochastically. Therefore the Lorentz factor is not pre-determined for the case of the turbulent electric field. However, for this case of $a/b \leq 5$ we note that the change of Lorentz factor in the integration time is not very large as seen in Figure 6.6, therefore we can regard the Lorentz factor $\gamma \sim \gamma_{init}$. Lastly we consider the spectral index for the Langmuir turbulence with $a > b > 1$. As we see above, the spectral index for $a > b > 1$ is not 1 predicted by perturbative DRL nor $1/2$ predicted by the angle diffusion effect. We regard that the spectral index is around $1/3$, because the radiation mechanism is identified as Wiggler mechanism, and the angle integrated spectral index is $1/3$ in Wiggler mechanism. Summarizing above, we confirm that the peak frequency is $\sim \gamma_{init}^2 \omega_{st}$ and the spectral index in low frequency side of the peak $\sim 1/3$ for the Langmuir turbulence with $a > b > 1$ and $a/b = O(1)$.

Lastly for completeness in the parameter range of η , we investigate the example of the extreme case of $\eta \gg \gamma_{init}$. For $\eta > \gamma_{init}$, the motion becomes strongly nonlinear and cannot be treated analytically. Thus, we show numerically calculated electron orbit. We show the radiation spectra and the orbit for $\eta = 500 > \gamma_{init}$ (Figure 6.7(d), Figure 6.9). As we expected, the peak frequency is $\sim \gamma_{init}^2 \omega_{st}$. We note that the spectral index of $2/3$ is the same as the

Wiggler radiation when the observer is located in a particular direction, i.e., the spectrum is not the angle integrated spectrum. This spectral index is evidence for the spectral index of $1/3$ for the case of turbulence with $a > b > 1$ for which angle integrated spectrum is calculated. The Lorentz factor changes from 10 to $O(100)$, but γ_{init} is relevant to the observer situated at z -axis. In other words, the beaming cone sweeps the observer when $\gamma \sim \gamma_{\text{init}}$ in the present geometry. The Lorentz factor relevant to each observer oriented in different angles is significantly different to each other. Moreover, in general the energy change in the PFT of peak frequency becomes larger than mc^2 , because the electric force in some phase of oscillation accelerates the electron linearly, and the curvature radius becomes larger. Thus, we have to consider the linear acceleration emission in this case. We consider the spectral flattening in the lowest frequency region of Figure 6.7d. The low frequency flattening should come from the condition that the observer sees the strong emission for a longer time than the synchrotron radiation in a uniform magnetic field. Since the orbit for the present case is more elongated to the x direction as seen in Figure 6.9, low frequency emission is observed to be enhanced from the z -axis. Although this is a trivial spectral shape, this feature has not been noticed before. This signature may play a role in the turbulent case. Thus, we draw the line on $a/b = \gamma$ and $a = 1$, and divide the $a > b > 1$ region. We call the radiation for this parameter range as "non-linear trajectory" radiation. This part of the spectra from an electron moving in the 3D turbulent electric field is determined by the chaotic trajectory. The generalization of the features of this regime is a future work.

Summarizing this section, we have considered the motion and radiation in a single mode plasma oscillation. We clarify that the cutoff frequency for $\eta > 1$ ($\omega_{\text{st}} > \omega_{\text{p}}$) is $\gamma_{\text{init}}^2 \omega_{\text{st}}$, which consists of higher harmonics of the fundamental frequency of $\bar{\gamma}^2 \omega_{\text{p}}$. It is from the effect that the beaming cone sweeps the observer, in the same way as the Wiggler radiation. Using this result, we interpret that the peak frequency for 3D Langmuir turbulence for $a > b > 1$ ($\omega_{\text{st}} > \omega_{\text{p}} > \omega_0$) is $\gamma^2 \omega_{\text{st}}$, where γ is determined by the acceleration. The shallower spectrum for $a > b > 1$ can be explained by WRL mechanism. Lastly, we show numerically calculated

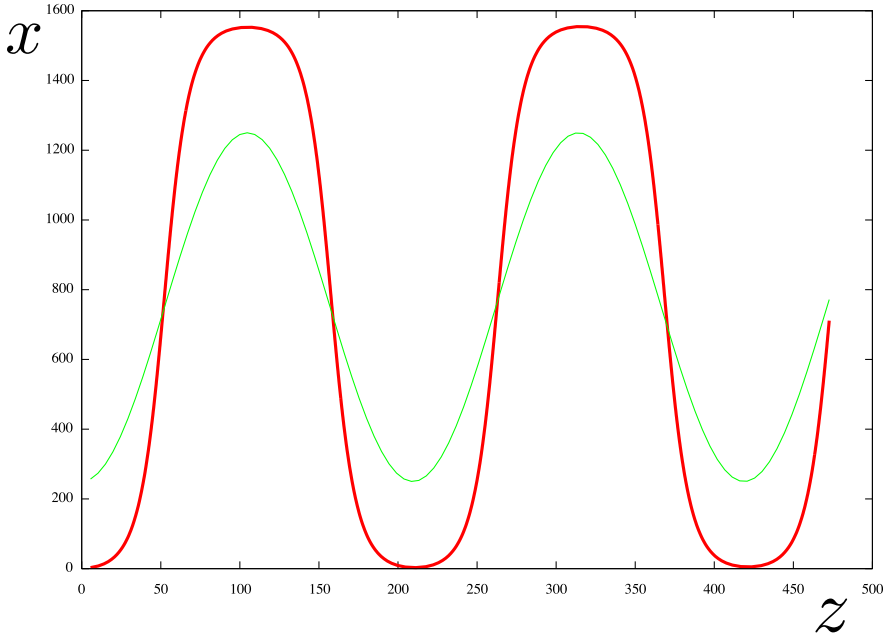


Figure 6.9: Electron orbit for $\eta = 500$. Vertical axis is x , and horizontal axis is z . The thick line shows the orbit for the radiating electron, while the thin line shows a sine curve for comparison.

radiation spectra for the extreme case of $\eta \gg \gamma_{\text{init}}$. It shows Wiggler like spectra in the middle and high frequency region, while the flattening can be seen in the low frequency region. It is from the effect of elongated trajectory to the electric field direction. The radiation signatures are summarized as a chart in the $a - b$ plane in Figure 6.10.

6.3 Discussion & Summary

We have calculated the radiation spectra from relativistic electrons moving in a Langmuir turbulence by using first principle numerical calculation. We characterize the radiation spectra by two parameters. The one is $a = \omega_{\text{st}}/\omega_0$, where $\omega_{\text{st}} = e\sigma/mc$ is the strength omega, and $\omega_0 = 2\pi c/\lambda$ is the spatial omega. The strength omega accounts for the effect of the field strength to the radiation spectra, and the spatial omega accounts for the effect of spatial

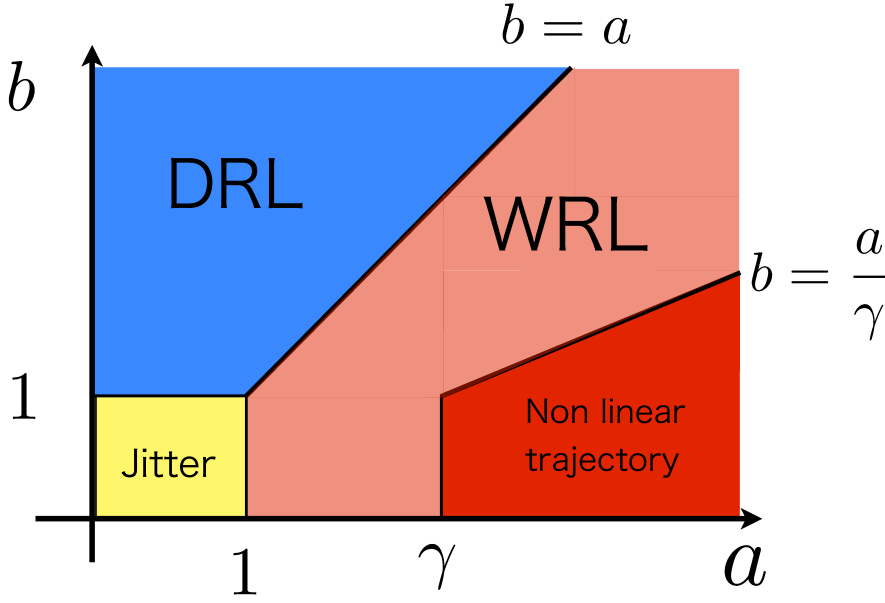


Figure 6.10: Chart of the radiation regimes. Horizontal axis is $a = \omega_{st}/\omega_0 = e\sigma/mc^2 k_{min}$, and vertical axis is $b = \omega_p/\omega_0$. For the jitter regime with $a < 1$ and $b < 1$, the radiation spectra are determined by the spatial fluctuations, because ω_0 is the largest of the three. The typical frequency for this case is $\gamma^2\omega_0$. For $b > a > 1$, i.e., $\omega_p > \omega_{st} > \omega_0$, the radiation spectra are represented by DRL theory, and typical frequency is $\gamma^2\omega_p$. The line $b = a$ divides the DRL region and WRL region, and the spectral features for the WRL regime $a > b > 1$ are newly clarified in this chapter. The typical frequency is $\gamma^2\omega_{st}$ and the spectral index of frequency region lower than the peak is $\sim 1/3$, in the same way as synchrotron radiation. For $a > \gamma$ and $a > \gamma b$, the orbit of a radiating electron depicts non-linear trajectory, and its signature appears at the low frequency region of the spectrum.

fluctuation with a typical scale of λ . The other is $b = \omega_p/\omega_0$, where ω_p is the plasma frequency, which accounts for effects of the time variability of the waves. We investigate the spectral signatures in the $a - b$ plane (Figure 6.10). For $a < 1$ and $b < 1$, the spectral features are the same as those of jitter radiation or Diffusive Synchrotron Radiation. For $b > a > 1$ and $b > 1 > a$, the theory of the Diffusive Radiation in Langmuir turbulence is confirmed, where time variability plays a primary role. For $a > b > 1$, the spectra show previously unknown features. In this regime, the peak frequency is $\sim \gamma^2 \omega_{st}$, which is higher than the predicted frequency $\gamma^2 \omega_p$ from the DRL theory. The spectral index of the frequency region lower than the peak is $\sim 1/3$. These features are explained by the Wiggler mechanism. To clarify the radiation features in this regime, we calculate the radiation spectra from an electron moving in an oscillating electric field, i.e., for vanishing spatial omega. We analytically calculate the motion of the electron, and numerically calculate the radiation spectra from this electron. We show that for $\eta = a/b \gtrsim 1$, the spectrum around the peak frequency consists of the higher harmonics of the fundamental mode, by considering the radiation in the mean velocity frame. The electron motion becomes relativistic for $\eta > 1$ even in this frame, so that strong higher harmonics photons are emitted because of the retarded time effect. As a result, the spectra in the observer frame consists of the higher harmonics of $\gamma^2 \omega_p$. The peak frequency is characterized by $\gamma^2 \omega_{st}$, which is understood by the analogy of the Wiggler radiation.

The feature that the radiation spectra from Langmuir turbulence have a wide range of spectral indices can be important for high energy astrophysical objects, in particular gamma ray bursts. The emission mechanism of GRB is not settled for now. The spectral indices of low frequency side of the Band function are distributed as a Gaussian with the central value of 0. Non-negligible number of GRBs have spectral index harder than the theoretical limit for synchrotron radiation $1/3$. The photospheric emission models can overcome this difficulty, but it also has another difficulty. The low energy spectral index of photospheric emission is 2, which is too hard to make it soft to the observe spectral indices ~ 0 . On the other hand, the radiation mechanism from Langmuir turbulence in this chapter has some advantages. Not

only the spectral index is harder than the synchrotron radiation and it can reproduce very hard spectra of observed GRB (Fleishman 2007b), but also it may explain a wide range of spectral indices. Because the parameters of a and b are likely to have a value around 1 near the shock front (Silva 2006, Dieckmann 2005), so that the radiation spectra change drastically around these parameters.

Chapter 7

Application to the Gamma Ray Flares of the Crab Nebula

7.1 Introduction

In this chapter, we show a jitter radiation model of Crab gamma ray flares. As we see in chapter 2, the observational results of these flares can not be explained by the standard model of pulsar wind nebulae. The radiation mechanism which is supposed in standard model in this energy range (around 100 MeV) is the synchrotron radiation. We consider a model in which the radiation mechanism changes from synchrotron radiation to jitter radiation in flare states.

We first rewrite observational features of the Crab flares for later convenience.

- The flares occur about once in a half year, the flux doubling timescale is around 8 hours, and duration time is a few weeks.
- The peak energy is as high as $375\text{MeV} > E_c$.
- There seem to be no counterparts in other energy ranges.
- They sometimes show very hard spectrum as $F_\omega \propto \omega^{1.08 \pm 0.16}$

We next introduce several other models which have been proposed to overcome the crucial problem of E_c . The obvious possibility is relativistic beaming effect. In the standard scenario of pulsar wind nebulae (e.g. Kennel & Coroniti 1984), the bulk speed of nebula region is nonrelativistic, but a possibility of the emission regions having relativistic speed was discussed from various aspects. (Komissarov & Lyutikov 2011, Bednarek & Idec 2011, Yuan et al. 2011, Kohri et al. 2012, Clausen-Brown & Lyutikov 2012). Another possibility is a separation between the acceleration region and emission region (Uzdensky et al. 2011, Cerutti et al. 2012, 2013). They considered the acceleration by the electric field on a reconnection sheet. The magnetic field on the reconnection sheet is much weaker than outside the sheet, and electrons can be accelerated by the electric field suffering from much weaker radiation loss and achieve a larger Lorentz factor. In somewhat different view point, Bykov et al. (2012) considered effects of inhomogeneities of the magnetic field strength. The highest Lorentz factor of electrons is limited by the mean strength of magnetic field, and the highest energy emission comes from small regions where the magnetic field is strongest. The spatial scale of the acceleration region is the same order of the Larmor radius of the highest energy electrons $r_L \sim 2 \times 10^{17} \left(\frac{\gamma}{10^{10}}\right) \left(\frac{B}{10^{-4}\text{G}}\right)^{-1} \text{cm}$, while the scale of the emission region is as small as $ct_{\text{fluc}} \sim 10^{15} \text{cm}$ or $ct_{\text{dur}} \sim 3 \times 10^{16} \text{cm}$. If the magnetic field varies by a factor of 3 in a small region, the emission energy can be higher than E_c in this case.

A common feature of these models is that the radiation process is considered to be synchrotron radiation. In contrast, we consider yet another possibility that the magnetic fields become turbulent on very small scales, and radiation process changes from synchrotron radiation to jitter radiation. The photon energy of jitter radiation can be higher than E_c in this situation (Fleishman 2006). For the jitter radiation, the typical frequency is determined by the scale λ_B of the turbulent magnetic field. We suppose that this scale is much smaller than $2\pi mc^2/eB$ and that the electrons move approximately straightly. The typical frequency is γ^2 times the inverse of the timescale that the electrons move across λ_B , and

$$\omega_B \sim \gamma^2 2\pi c / \lambda_B. \quad (7.1)$$

Therefore, photons with frequencies higher than $\gamma^2 eB/mc$ can be emitted if the spatial scale of the turbulent magnetic field is smaller than $2\pi mc^2/eB$.

In section 7.2, we explain possibilities to create the flares by jitter radiation and discuss the flare energetics and spectra. In section 7.3, we discuss differences from other models. We summarize this chapter in section 7.4.

7.2 Jitter radiation model

7.2.1 Small scale turbulence

When $\lambda_B < 2\pi mc^2/eB$, in other words, when the strength parameter

$$a \equiv \frac{eB\lambda_B}{2\pi mc^2} \quad (7.2)$$

is smaller than 1, jitter frequency is larger than synchrotron frequency. Using the condition for jitter approximation of $a < 1$, we can write the strength of magnetic field of the emission region as

$$B < 1 \times 10^{-3} \left(\frac{\lambda_B}{10^7 \text{cm}} \right)^{-1} \text{G}. \quad (7.3)$$

We suppose that the acceleration site for the flares is near the shock front. We tentatively assume that the magnetic field becomes turbulent in a small part of the acceleration region, though we consider later that the size of them is same order. The Lorentz factor of accelerated electrons which emit the highest energy synchrotron photons $\sim 100\text{MeV}$ in a quiescent state is thought to be $\sim 10^{10}$ and the average magnetic field strength of $\sim 10^{-4}\text{G}$ (Kennel & Coroniti 1984, De Jager & Harding 1992, Atoyan & Aharonian 1996, Tanaka & Takahara 2010). The required scale of turbulence to meet the condition $a < 1$ is $\lambda_B < 10^8\text{cm}$ when magnetic field strength is 10^{-4}G . On the other hand, the required scale to emit flare photons with energy $\sim 400\text{MeV}$ by the highest energy electrons through the jitter radiation, the required scale of turbulent magnetic field is $\sim 3 \times 10^7\text{cm}$.

We note that the wavelength of the striped wind of the Crab pulsar ($\lambda_{\text{sw}} \equiv c \times 33\text{ms} \sim 10^9\text{cm}$) is around the required length. Our picture of the flares is expressed as follows. When alternating magnetic fields are injected into the acceleration site, fluctuations with scales shorter than λ_{sw} are generated through compression or transformation to some type of waves. The highest energy electrons feel the small scale magnetic fields, and radiate high energy photons by jitter mechanism. In the quiescent state this mechanism may not work, because the density in the pulsar wind is very low, and the small scale turbulent field is suppressed, as we see in the next paragraph. Here we consider here how the small scale magnetic field can be generated when the flares occur. In general, the pulsar wind fluctuates temporarily and spatially. For example, the Crab pulsar is known to emit very energetic radio pulses, called "Giant Radio Pulse" (GRP) about once in thousands (e.g. Lundgren et al. 1995). This suggests that there may be large density fluctuations in the magnetosphere. Furthermore, from the observations of these GRPs, it has been argued that the dispersion measure fluctuates largely, and these fluctuations can not be explained by considering the density fluctuations of the interstellar medium alone. Therefore, it is suggested that there are large density fluctuations in the Crab nebula (Kuz'min et al. 2008, 2011). From these observations, it is quite natural to suppose that there are density fluctuations in the wind region. We advocate the model that plunging of a high density blob into the termination shock triggers a flare. We note, however, that the flares are not directly the same events as GRP (Mickaliger et al. 2012).

Next we compare the wavelength of striped wind and the typical scales of plasma in the co-moving frame, and consider the conditions for survival of small scale magnetic fields. Although the striped wind itself is a non-propagating entropy mode, existence of high density blobs and moderate reconnection may generate electrostatic and electromagnetic modes on somewhat shorter wavelength than λ_{sw} . We may consider various modes, for example, electron Bernstein mode, which is the electrostatic wave in a thermal plasma (Bernstein 1958), but we do not specify the type of plasma turbulence. When the inertial length is longer than the λ_{sw} , the electromagnetic modes can survive, while the short scale electrostatic mode may decay. To

estimate the typical scale of the survival of the longitudinal modes, we use the value of inertial length. First we consider it in the upstream, i.e., wind region. The Debye length is very small compared to the inertial length, because the plasma is cold when the reconnection is moderate. The inertial length c/ω_{pe} can be estimated given the comoving number density. The spindown luminosity is expressed by

$$L_{sd} = 4\pi r_{ts}^2 n \Gamma u m c^3 (1 + \sigma) = 6 \times 10^{38} \text{ergs}^{-1}, \quad (7.4)$$

where $r_{ts} = 3 \times 10^{17} \text{cm}$, n is the comoving number density, $\Gamma = 10^6$ (Kennel & Coroniti 1984) or $\Gamma = 7 \times 10^3$ (Tanaka & Takahara 2010) is the bulk Lorentz factor of the pulsar wind, u is the radial four velocity, σ is the ratio of magnetic to kinetic energy flux. In general, σ is thought to be much smaller than 1 at the shock region ($\sigma \sim 0.003$ is the best fit value in Kennel & Coroniti 1984). We adopt this assumption, and neglect σ in (7.4). When we adopt the value of the bulk Lorentz factor by Tanaka & Takahara 2010, we get the comoving density $n \sim 4 \times 10^{-10} \text{cm}^{-3}$ and the value of inertial length

$$\left(\frac{c}{\omega_{pe}} \right)_{u,TT} \sim 3 \times 10^{10} \text{cm}. \quad (7.5)$$

When we adopt $\Gamma = 10^6$ (Kennel & Coroniti model), the comoving density becomes smaller. Using the equation (7.4), we get $n \sim 2 \times 10^{-14} \text{cm}^{-3}$, and we obtain

$$\left(\frac{c}{\omega_{pe}} \right)_{u,KC} \sim 3 \times 10^{12} \text{cm}. \quad (7.6)$$

On the other hand, the comoving wavelength of striped wind is

$$(\Gamma \lambda_{sw})_{TT} \sim 1 \times 10^{12} \text{cm}, \quad (7.7)$$

$$(\Gamma \lambda_{sw})_{KC} \sim 2 \times 10^{14} \text{cm}. \quad (7.8)$$

Therefore, the inertial length is shorter than the wavelength of striped wind. From the estimation described above, we can see that the small scale turbulence can survive in the wind region.

Next we consider the parameters for downstream. We do not consider the possibility that the downstream plasma has a bulk relativistic speed. The inertial length and Debye length are comparable at relativistic temperatures. We adopt the value of typical Lorentz factor $\gamma = 7 \times 10^3$ (Tanaka & Takahara model), and $\gamma = 10^6$ (Keneel & Coroniti model). Then we obtain the inertial length

$$\left(\frac{c}{\omega_{pe}} \right)_{d,TT} \sim 3 \times 10^{10} \text{cm}, \quad (7.9)$$

$$\left(\frac{c}{\omega_{pe}} \right)_{d,KC} \sim 3 \times 10^{12} \text{cm}. \quad (7.10)$$

The wavelength of striped wind is compressed by a factor of a few $\times \Gamma$ times compared to comoving wavelength in the upstream. Therefore, the typical scale of magnetic field is

$$(\lambda_{sw})_d \sim 3 \times 10^8 \text{cm}. \quad (7.11)$$

From the estimation above, we see that the small scale turbulence decays far downstream. We note that near the shock front or in the shock transition region, the plasma is not completely thermalized. Therefore, the small scale turbulence can survive in some measure there.

Generally, when the Debye length is much larger than λ_{sw} , the longitudinal mode would disappear rapidly. However, when the dense blob enters the shock front, the inertial length becomes shorter and small scale turbulence tends to survive in longer time. The density required for the survival far downstream is 10^5 times larger than the mean density n , but even when the density contrast is less extreme, short wavelength turbulence required for the flares can exist in the shock transition region.

Summarizing this subsection, jitter radiation can produce the flare when the small scale turbulence survives in the shocked dense blob, and the typical scale of turbulence is consistent with the typical frequency of the flares. We propose the flare model that the high density blob plunge into the termination shock, an entropy mode is compressed or transformed to some other waveform in the shock transition region, the accelerated electrons move in this kind of turbulent field and radiate the highest energy photons by jitter mechanism.

7.2.2 Energetics

Now that we have shown that the peak energy higher than E_c can be explained by jitter radiation, we next examine the energetics of flares. Firstly we note that the energetics problem is very difficult to solve and has not been much addressed in previous models. The scale of the emission region is constrained by the observed fluctuation time scale as $ct_{\text{fluc}} \sim 10^{15}\text{cm}$ or by the duration timescale as $ct_{\text{dur}} \sim 3 \times 10^{16}\text{cm}$. It is very difficult to concentrate 1% of the spin down luminosity on this small region, compared to the circumference of the termination shock $\sim 2 \times 10^{18}\text{cm}$, in either case. We discuss the energetics by considering the size of the emission region and the density of radiating particles in it. The Crab nebula is not spherically symmetric as is seen in the X-ray image by Chandra X-ray observatory (Figure 2.6). It is possible that the emission regions of 100MeV gamma-rays are patchy, but we do not resolve the Crab nebula at 100MeV gamma-rays, then we assume that the shape of the emission region is a ring as drawn in Figure 7.1, for simplicity. When the nebula is quiescent, the radial thickness is determined by synchrotron cooling. To estimate the radial thickness, we suppose that the acceleration site is located only near the shock front, and the electrons return to the shock front on gyro time. If we assume the standard value of the strength of magnetic field $B = 300\mu\text{G}$ (Kennel & Coroniti 1984), and considering the fact that cooling limits the attainable energy as $\gamma \sim 6 \times 10^9 (\frac{B}{3 \times 10^{-4}\text{G}})$, we get the radial thickness of the ring as $r_L \sim 3 \times 10^{16}\text{cm}$. When we assume $B = 85\mu\text{G}$ (Tanaka & Takahara 2010), the thickness is three times larger. We assume that the injection site of highest energy electrons is on the equatorial plane, so the ring height is also constrained by gyro radius of highest energy electrons. The radius of the termination shock is $3 \times 10^{17}\text{cm}$, so the radial thickness and height of the 100MeV ring is a few $\times 10\%$ of the radius.

Next we estimate the parameters in the emission region in the flare state. Firstly we examine the case when the scale of the blob is $ct_{\text{fluc}} \sim 10^{15}\text{cm}$, and the single blob becomes the emission region for the flare. We assume that the blob moves on the equatorial plane, so a part of the ring becomes the emission region of flare. If we assume that the strength of magnetic

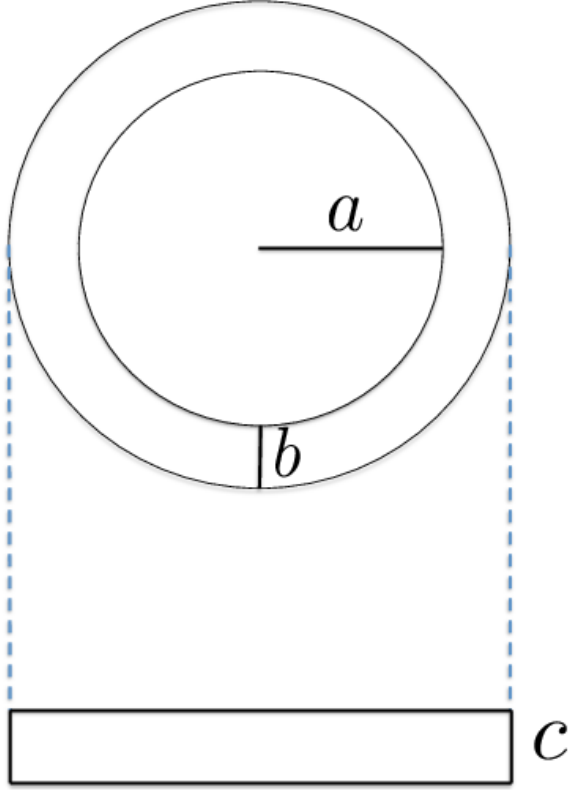


Figure 7.1: Cartoon of the "100MeV ring". The length a is the radius of termination shock $r_{ts} = 3 \times 10^{17}\text{cm}$, b is radial thickness and c is the height of 100MeV ring. They are restricted by the Larmor radius of $3 \times 10^{16}\text{cm}$.

field in the blob is the same as in the other region, the radial thickness of jitter emission region cannot be determined by synchrotron cooling, because the Larmor radius of the highest energy electrons $3 \times 10^{16}\text{cm} \left(\frac{B}{3 \times 10^{-4}\text{G}} \right)^{-3/2}$ is larger than the blob size ct_{fluc} . The acceleration region is larger than the jitter emission region and the size of emission region is determined by blob size in this picture. However, this picture does not work for flare models. The reason is as follows. The energy distribution of electrons at flare states is very hard and different from the one of the quiescent state. Then the acceleration process in the acceleration region of the highest energy electrons which emit flare photons is different from other region. We assume that a

dense blob enters in the termination shock region, and implicitly assume that the other region is undisturbed. Then the acceleration process outside the blob should be the same as in the quiescent state. Therefore, it is more natural that the magnetic field in the blob is stronger than the mean magnetic field strength and that the acceleration process is also different in the flare states to produce highest energy electrons with a very hard spectrum. Thus, the cutoff energy of accelerated electrons should be smaller because of the strong magnetic field. Since the size of acceleration region is limited by the blob size, the required strength of magnetic field is $3 \times 10^{-3}\text{G}$ to make $r_L = ct_{\text{fluc}}$, and the maximum Lorentz factor is limited by radiation loss and becomes smaller to $\sim 2 \times 10^9$. Therefore, the required wavelength of turbulent field becomes 10^6cm to emit 400MeV photons. This constraint may seem to be very tight, but it is not improbable. From this consideration, the volume of the blob is 10^{45}cm^3 and the emission region of the flare is about 2×10^6 times smaller than in quiescent state, because the volume of 100MeV ring is (circumference) \times (radial thickness) \times (height) $= 2 \times 10^{51}\text{cm}^3$.

The constraint for the volume of emission region can be alleviated when we assume the blob size is $ct_{\text{dur}} = 3 \times 10^{16}\text{cm}$, and flux fluctuation comes from the internal structure of the blob of which scale is $ct_{\text{fluc}} = 10^{15}\text{cm}$. We assume that the acceleration scale is the same as the blob scale, and small denser regions of which scale is $\sim ct_{\text{fluc}}$ distribute in it as depicted in Figure 7.2. The mean magnetic field strength is $3 \times 10^{-4}\text{G}$, by equating Larmor radius of highest energy electrons and ct_{dur} . The Lorentz factor of the highest energy electrons is determined by the magnetic field strength as $\gamma \sim 6 \times 10^9$, and the required wavelength of turbulent field to emit 400MeV photon is estimated as 10^7cm . The size of the blob is $3 \times 10^{16}\text{cm}$, which is the same as the thickness of the 100MeV ring in the quiescent state for the standard magnetic field strength. Therefore the blob volume is only about 10^2 times smaller than the 100MeV ring.

Next we consider the required number density of highest energy electrons in the blob to reproduce the flare luminosity. We are considering the high density blob, so the number density of accelerated electrons can be much larger than the one of the quiescent state. The luminosity

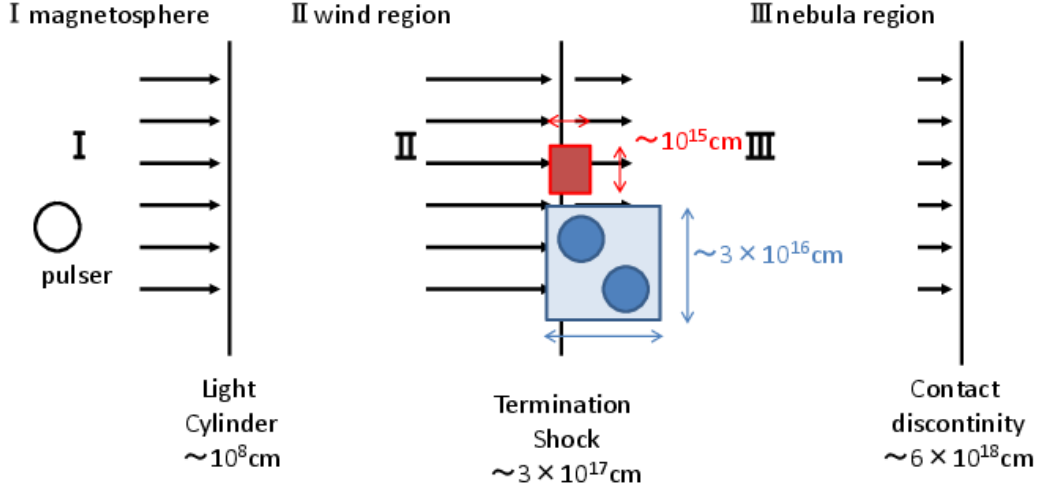


Figure 7.2: A schematic picture for comparison of relevant scales. The red box is the emission region of the homogeneous blob model, and the blue box is that of the inhomogeneous blob model.

is proportional to $\gamma^2 B^2 N$, where N is the number of electrons at maximum energy in the blob. First, for homogeneous blob of a size ct_{fluc} , we assumed that the magnetic field strength is about 10 times larger than the mean magnetic field strength. Therefore the maximum Lorentz factor is limited as 2×10^9 , which is a few times smaller than the Lorentz factor of the highest energy electrons in other regions in the 100MeV ring. The volume of the emission region is 2×10^6 times smaller than that in a quiescent state. Therefore, the required number density of the highest energy electrons in the blob is about 10^6 times larger than in the quiescent state to reproduce the flare luminosity. In section 7.2.1, we considered the required density for the survival of the small scale fluctuations in shock transition region. It is about 10^5 times the

mean density. If the acceleration is the same as in the quiescent state, the number density of the highest energy electrons may not be as large as 10^6 times the number density of the highest energy electrons in the quiescent state. However, the energy distribution of accelerated electrons is very hard, so the number of the highest energy electrons can be 10^6 times larger than in the quiescent state. Therefore, the flare luminosity can be explained by this model if the mean density in blob fulfills the condition of the survival of the small scale turbulence. Here, we have to note that the flare luminosity is 1% of the spindown luminosity, so the asymmetry of the pulsar wind must be very high in this model.

Next, we examine the constraint on the scenario of inhomogeneous blob of a size ct_{dur} . The blob volume is only 10^2 times smaller than the 100MeV ring, and we assumed that the magnetic field strength is the same order as the one of quiescent state ($3 \times 10^{-4}\text{G}$), so the maximum Lorentz factor of the electrons is the same as in other region. The required number density of highest energy electrons in the blob is about $10^2 - 10^3$ times larger than the mean density of highest energy electrons. The flare luminosity can be obtained by considering the hardness of electron energy distribution which is calculated from the observed flux alone, and the high number density of electrons would help to accomplish the large luminosity of flare. In short, while the small homogeneous blob scenario is not impossible, large inhomogeneous blob scenario is more plausible.

7.2.3 Spectrum

The observed spectra of flares indicate that the energy distribution of electrons is very hard. As is discussed in the previous subsection, the hard energy distribution of electrons is also required to solve the energetics. If the electrons take a power law energy distribution, the power law index p of electrons ($\frac{dN}{dE} \propto E^{-p}$) can be estimated from the photon index. However, when the strength parameter $a < 1$ and when either $p < 1$ or $p < 2\mu + 1$, the photon index around 100MeV can be determined by jitter mechanism, where μ is the power law index of isotropic turbulent magnetic field ($B^2(k) \propto k^{-\mu}$). The spectrum of flare component is fitted by

a power law plus cutoff, and the time integrated power law index is $\gamma_F = 1.27 \pm 0.12$ (Buehler et al. 2011). Clausen-Brown & Lyutikov reexamined the time resolved spectrum in Buehler et al. 2012, and obtained the photon index in the most luminous period as $\gamma_F = 1.08 \pm 0.16$. If the index is supposed to reflect the energy distribution of electrons, the time integrated power law index is $p = 1.54 \pm 0.24$ and time resolved one (in the most luminous state) is $p = 1.16 \pm 0.32$, because $\gamma_F = (p + 1)/2$. It is very hard and inconsistent with the power law index $p = 2.5$ at injection in the quiescent state (Tanaka & Takahara 2010). Additionally, the hard energy distribution is consistent with the observation that no counterpart of the flares has been detected in other wavelengths. From these facts, the particle acceleration in the blob is expected to be different from the other region. For example, a stochastic acceleration process may play a crucial role to make the hard electron energy distribution in a short time (see e.g. Hoshino 2012).

The hard photon index can be interpreted as the reflection of hard power law index of electron energy distribution, but getting the value $p \sim 1$ is somewhat difficult (Clausen-Brown & Lyutikov 2012). We show another interpretation of these spectral indices by using the theory of jitter radiation on the assumption that the accelerated electrons follow a very hard, almost monoenergetic distribution. For $a < 1$, the theoretical spectrum of jitter radiation from monoenergetic particles moving in an isotropic turbulent magnetic field is expressed as a broken power law and cutoff as is seen in Figure 7.3 (e.g. Fleishman 2006). The photon index of the low energy side is $\gamma_F = 1$, and that of the high energy side is $\gamma_F = \mu + 1$. The cutoff energy is determined by the smallest scale (in other words, dissipation scale λ_{dis}) of the turbulent field. The inertial length, which corresponds to the typical scale of magnetic field fluctuations, is proportional to $n^{1/2}$, and the luminosity is proportional to n when the emission region volume is fixed. Therefore, the typical photon energy of flares is the highest in the most luminous state. Additionally, the typical energy and flux should have the positive correlation in this model, and it is consistent with the observation (Buehler et al. 2011). We regard the photon index of $\gamma_F = 1.08 \pm 0.16$ as the intrinsic photon index of jitter radiation. At this

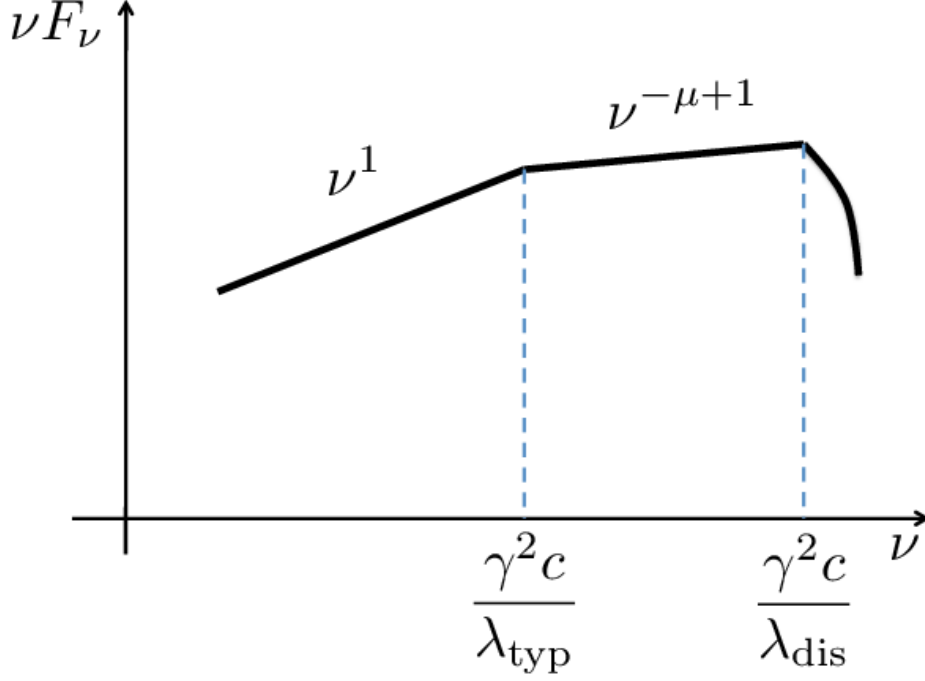


Figure 7.3: Radiation spectrum of jitter radiation by monoenergetic electrons for $a < 1$.

time, the dissipation scale λ_{dis} and injection scale λ_{typ} of turbulent field are very close, so it is difficult to resolve cutoff frequency $\gamma^2 c / \lambda_{\text{dis}}$ and break frequency $\gamma^2 c / \lambda_{\text{typ}}$. When the flux is smaller, the injection scale would be larger because the number density would be smaller. Therefore, $\gamma^2 c / \lambda_{\text{typ}}$ becomes smaller, so the photon index around 100MeV can be interpreted as a reflection of the power law index of magnetic field fluctuations. It should be noted that it is usual $\mu > 1$ in the ordinary turbulent field, which causes some problem that $\mu < 1$ is required to explain the observed spectral index.

7.3 Discussion

7.3.1 Difference from other models and predictions

We have considered inhomogeneities of the emission region. Bykov et al. also considered inhomogeneous emission regions. At first, we discuss the difference from their model. They assumed that the size of the acceleration site is much larger than the emission region, and the acceleration mechanism in the quiescent state and flare state is identical. If the energy distribution of electrons stays unchanged in the flare state, the spectra in 100MeV range cannot become harder than the spectrum in MeV range in the quiescent state. This does not seem to match observations. In contrast, we consider that the acceleration site should have a similar size to the blob size, and the acceleration mechanism is different in the flares, because the observed spectrum is very hard. When the electron energy distribution is very hard ($p \leq 1$), the photon index $\gamma_F = 1$ can be naturally explained by jitter mechanism. They deal with the problem assuming that the emission region is 1D for radial direction, and they do not consider the energetics explicitly in their paper. They consider the radial length of the emission region is the same as the quiescent state ($2 \times 10^{16}\text{cm}$), and there are the blobs randomly distributed with the 1% scale ($\sim 10^{14}\text{cm}$) having stronger magnetic field. The length is consistent with the observed timescale of the flares.

The scale corresponding to the single pulse of flare has to be smaller than 10^{15}cm . The solid angle of the emission region can be constrained by duration time of flare. Therefore, the predicted luminosity is a few dozen times smaller than the observed one. While they predicted that the polarization degree would enhance during the flare, our model predicts the converse prediction. The polarization degree would be very low during the flare, because the gamma-rays are emitted in the turbulent field by jitter mechanism.

The most popular interpretations of the Crab flares are Doppler boost models. While Doppler boost model predicts that the TeV-PeV flare would accompany the 100MeV flare, our model does not predict such a correspondence between GeV and TeV-PeV. In our model,

the increase of the highest energy electrons and frequency shift collaborate to create the flare. Therefore, the required total number of the highest energy electrons is only a few times larger than the quiescent state. In TeV-PeV range, since there are no frequency shift, and inverse Compton scattering by the highest energy electrons are in Klein-Nishina regime so that only a very weak bump will appear in PeV range.

The hard spectrum of flares is one of the difficult features to interpret. Clausen-Brown & Lyutikov explained this hard spectrum by very hard electron energy distribution near the radiation reaction limit. They assumed acceleration time much shorter than escaping time, and considered radiation loss. The electrons pile up near the maximum energy. They commented that the pile-up scenario could explain the observed SED by tuning the acceleration timescale. If acceleration time is much shorter than the fluctuation time of flare, the distribution becomes monoenergetic, and spectrum becomes intrinsic one $\gamma_F = 2/3$ for synchrotron radiation or $\gamma_F = 1$ for jitter radiation. Our model does not require the tuning of acceleration time, and predict that the flare spectrum will not be harder than $\nu F_\nu \propto \nu^1$.

7.3.2 Acceleration and scatterers

Kirk and Reville argued that jitter radiation cannot emit photons with energy higher than the critical synchrotron energy in the DSA scenario in their paper (Kirk & Reville 2010). In their analysis, they assumed that the scatterer (magnetic field fluctuation) is a single population. For $a < 1$, particles experience ballistic transport and take a longer time to come back to the shock than the gyrotime. Therefore, the acceleration time becomes longer, so the maximum energy of electrons becomes smaller, and radiation frequency is smaller than the one for $a > 1$ in spite of taking into account jitter mechanism. Conversely we argue that the jitter mechanism can emit higher energy radiation than synchrotron one. The reason for apparently inconsistent conclusions lies in the difference of situations. We assumed implicitly the existence of multi populations of scatterers. Although we do not specify the acceleration mechanism, we suppose that the large scale scatterers exist, too. The acceleration time depends on the large scale (as

large as Larmor radius) scatterers, so the acceleration time is not so long. Therefore, our model does not contradict their conclusion. In fact, the situation with two populations of scatterers are considered by Reville & Kirk 2010, and jitter component emerges over the synchrotron cut off. Stated another way, the photon energy of jitter component can be higher than that of synchrotron component when there are multi population of scatterers.

7.4 Summary & Conclusion

We propose a model which explains the flares of the Crab nebula over the 100MeV by jitter radiation. The wavelength of striped wind of the Crab pulsar is about two order of magnitude longer than the required scale of turbulent field to emit photons with energy $E > E_c$ by jitter mechanism. A high density region is required for existence of the small scale turbulence. It is suggested that there are large density fluctuations in the Crab pulsar magnetosphere and nebula. Therefore, we consider that there are high density blobs in the pulsar wind region. The blobs plunge into the termination shock, generate the short wavelength turbulence of electromagnetic field, and accelerated electrons radiate gamma-ray emission by jitter mechanism in the blob. The required strength of mean magnetic field in blob is 10 times larger, and the number density of highest energy electrons in blob is 10^6 times larger than in quiescent state to reproduce the April 2011 flare by homogeneous blob model for which the size of the blob is $ct_{\text{fluc}} \sim 10^{15}\text{cm}$. When we adopt the inhomogeneous blob model, for which the size of the blob is $ct_{\text{dur}} \sim 3 \times 10^{16}\text{cm}$, the required magnetic field strength is as large as that of the quiescent one, and number density of highest energy electrons is about $10^2 - 10^3$ times larger than in the quiescent state. The required high density of highest energy electrons in the blob is consistent with our assumption that high density blobs trigger flares and hard energy distribution of electrons which is implied by observed spectra. The very hard photon index $\gamma_F = 1.08 \pm 0.16$ of April 2011 flare in the brightest state is consistent with the intrinsic photon index of jitter radiation for $a < 1$. We make following three predictions for the future Crab flares: firstly, the

polarization degree will become lower in flare state, secondly, no counterpart will be seen in TeV-PeV range, and thirdly, the flare spectrum will not be harder than $\nu F_\nu \propto \nu^1$.

Chapter 8

Overall Conclusions

In this thesis, we have studied the radiation spectra from relativistic electrons moving in the turbulent electromagnetic fields. We should consider the radiation signatures taking into account the turbulence, since the electromagnetic turbulence would be generated in the shock region of high energy astrophysical objects. They often show the radiation spectra which are hard to explain with the conventional synchrotron and inverse Compton processes. We have performed first principle numerical calculations to investigate the radiation signatures for various turbulences. We have obtained a general reference chart of the spectral shapes as well as several new features previous unknown or only ambiguously understood for the 3D isotropic electromagnetic turbulence. In addition, to obtain better understanding of the radiation mechanisms which determine the spectral signature, we have performed analytical calculation of the electron motion for a single mode plasma oscillation and numerically calculate the radiation spectra which are compared with those for turbulent fields. We also consider applications of these radiation mechanisms to specific astrophysical objects, especially for the peculiar gamma ray flares from Crab nebula, for which we construct a detailed model. We summarize our important results.

8.1 Spectral features for isotropic electromagnetic turbulence

In chapters 5 and 6, we have investigated the radiation spectra for various turbulent fields. A turbulent field is characterized by the spatial scale λ_{typ} , field strength σ , and oscillation timescale T_w , and in term of the frequency by $\omega_0 = 2\pi c/\lambda_{\text{max}}$, $\omega_{\text{st}} = e\sigma/mc$, and $\omega_w = 2\pi/T_w$. We normalize ω_{st} and ω_w by ω_0 as

$$a \equiv \frac{\omega_{\text{st}}}{\omega_0} = \frac{2\pi e\sigma}{mc^2\lambda_{\text{typ}}}$$

$$b \equiv \frac{\omega_w}{\omega_0}.$$

We have studied two cases of the turbulences. The first one is the magnetic (transverse) turbulence supposed to be generated by Weibel instability. We assume that this magnetic field is static, because the Photon Formation Time (PFT) would be shorter than the variation time scale of the field. The parameter characterizing these fields is only a , since $b = 0$ for a static field.

- For $a \sim 1$, the break frequency in the low frequency region $\omega_{\text{bl}} \sim a\gamma^2\omega_{\text{st}}$ and the break frequency in high frequency region $\omega_{\text{bh}} \sim a^{-1}\gamma^2\omega_{\text{st}} = \gamma^2k_{\text{min}}c$ become nearly equal and a peak of the spectrum is formed. The lower side of the peak shows $F_\omega \propto \omega^{1/2}$, while the higher side of the peak shows $F_\omega \propto \omega^{-\mu}$, where μ is the power law index of the turbulence $B^2(k) \propto k^{-\mu}$. This result should be compared to that for $a \ll 1$, i.e., previously obtained by Medvedev (2006) and Fleishman (2006).
- For $1 < a < \gamma$, the spectrum shows mixed signatures of synchrotron and jitter radiation. Around the peak frequency, the spectral shape is identical to the synchrotron radiation, i.e., the peak frequency is $\gamma^2\omega_{\text{st}}$, and lower side of the peak shows $F_\omega \propto \omega^{1/3}$, and higher side shows an exponential cutoff. However, in the highest frequency region beyond the

cutoff, the power low component $F_\omega \propto \omega^{-\mu}$ emerges, and in the lowest frequencies a deviation from $F_\omega \propto \omega^{1/3}$ is seen around $a^{-3}\gamma^2\omega_{\text{st}}$.

- These spectral features are clearly interpreted by the concepts of PFL and electron trajectory.

The second one is the electrostatic (longitudinal) turbulence supposed to be generated by two stream instability. This turbulence consists of Langmuir waves, so that we take into account the time variability of the field. The parameters characterizing these fields are a and b , where the frequency of the field ω_w is assumed to be identical to the plasma frequency ω_p . We assume 3D isotropic turbulence, and the energy change of electron is directly taken into account. The main results are the followings.

- We organize the radiation signatures noted by previous researchers in various parameter range, and calculate the spectra in intermediate regimes for which any approximations hard to apply.
- For the most interesting parameter regime of $a > b > 1$, for which some confusion has been seen in previous works, we clarify the spectral signature. The peak frequency is $\gamma^2\omega_{\text{st}}$ and other spectral signatures are almost identical to the Wiggler radiation.
- We confirm the above by analytical calculation of electron motion in a pure plasma oscillation.
- The effects of energy change of the radiating electron plays minor role for the radiation spectra for $a \sim b \sim 1$, which is expected in relativistic shocks.

8.2 Jitter radiation model of the Crab gamma ray flares

The Crab gamma ray flares discovered recently show a few peculiar signatures. In particular, the maximum energy of gamma rays exceeds the critical energy E_c determined by synchrotron

radiation loss. We propose a model where the flare emission is due to jitter radiation mechanisms. This model satisfies the constraints of short variable time and very large luminosity, which have been ignored in a large part of previous researches.

- To reproduce the flares, we require that a high density blob with number density higher than $10^2 - 10^3 \times$ mean number density in quiescent state plunges into the termination shock, and the entropy mode (striped wind) is converted to the magnetic turbulence, and jitter radiation makes a gamma ray flare.
- We make three observational predictions for the future Crab flares: first, the polarization degree will become lower in flare state; second, no counter part will be seen in TeV-PeV range; and third, the flare spectrum will not be harder than $\omega F_\omega \propto \omega^1$. The predictions will be evidences for our model because these features would contradict the predictions by other models.

The radiation spectra from relativistic electrons interacting with turbulence have various different signatures from those of other existing radiation mechanisms. Notwithstanding, only a few applications to high energy astrophysical objects have been done. In this thesis, we have shown a clear reference chart of radiation signatures, so that we hope that this thesis will play a role in understanding the physical mechanisms of the high energy astrophysical objects by applying to the observed spectra.

Appendix A

Basic Concepts of Radiation from a Single Particle

In this appendix A, we briefly review the radiation mechanisms from an electron moving in electromagnetic fields. First, we introduce the basic picture of the synchrotron radiation. This is one of the most popular radiation mechanisms from a relativistic electron interacting with external magnetic field. Next, we introduce two convenient concepts for understanding the radiation spectrum. The one is photon formation length (PFL) or Photon Formation Time (PFT), and the other is the virtual quanta. The picture of the synchrotron radiation and these concepts are very useful to understand the radiation signatures in this thesis. Lastly we briefly show the synchrotron insertion devices of Wiggler and Undulator. The concepts which are developed for these devices are also useful for interpretation of radiation spectra.

A.1 Synchrotron radiation

The synchrotron radiation is the radiation from a relativistic charged particle moving in uniform magnetic field. It is firstly calculated by Schott (1912), and sophisticated by many researchers, for example, Schwinger (1949) and Ginzburg & Syrovatskii (1965). The basic pic-

ture of the synchrotron radiation is as follows. A charged particle with Lorentz factor $\gamma \gg 1$ is moving in a uniform magnetic field. The energy of this particle is constant, since there is no electric field. The equation of motion is written as

$$m\gamma \frac{d}{dt} \mathbf{v} = \frac{q}{c} \mathbf{v} \times \mathbf{B}, \quad (\text{A.1})$$

where m is mass and q is charge for this particle. Separating the velocity components along the field and in a plane normal to the field, it is separated into

$$\frac{d\mathbf{v}_{\parallel}}{dt} = 0, \quad (\text{A.2})$$

$$\frac{d\mathbf{v}_{\perp}}{dt} = \frac{q}{\gamma mc} \mathbf{v}_{\perp} \times \mathbf{B}. \quad (\text{A.3})$$

Because of $|\mathbf{v}| = \text{constant}$, $|\mathbf{v}_{\perp}| = 0$. The frequency of the gyration is

$$\omega_g = \frac{qB}{\gamma mc}. \quad (\text{A.4})$$

Thus, the particle traces helical orbit with rotation frequency ω_g .

The major part of radiation power from relativistic particle is emitted toward velocity direction, concentrated into small cone within the angle $\sim 1/\gamma$. It can be understood easily by using Lorentz transformation as follows. We assume the magnetic field is along the z -axis and pitch angle $\alpha = \pi/2$ and the instantaneous velocity direction is along x -axis. In the electron rest frame, there is electric field $E'_y = -\gamma v B_z / c$. The electron accelerates toward by the electric field toward y' direction, so that the radiation intensity resembles that of dipole radiation, anisotropic intensity of which is depicted in the upper in Figure A.1. The emitted photon direction is written as

$$\cos \theta' = \frac{\cos \theta - \beta}{1 - \beta \cos \theta}, \quad (\text{A.5})$$

where θ is the angle between the x -axis and radiation direction. From this equation, the emitted photon into $\theta' \leq \pi/2$ region is concentrated into small angle $\theta = 1/\gamma$, i.e., $\cos \theta > \beta$. The radiation in the observer frame is strongly anisotropic, which is called relativistic beaming. The beamed emission in observer frame is depicted lower in Figure A.1.

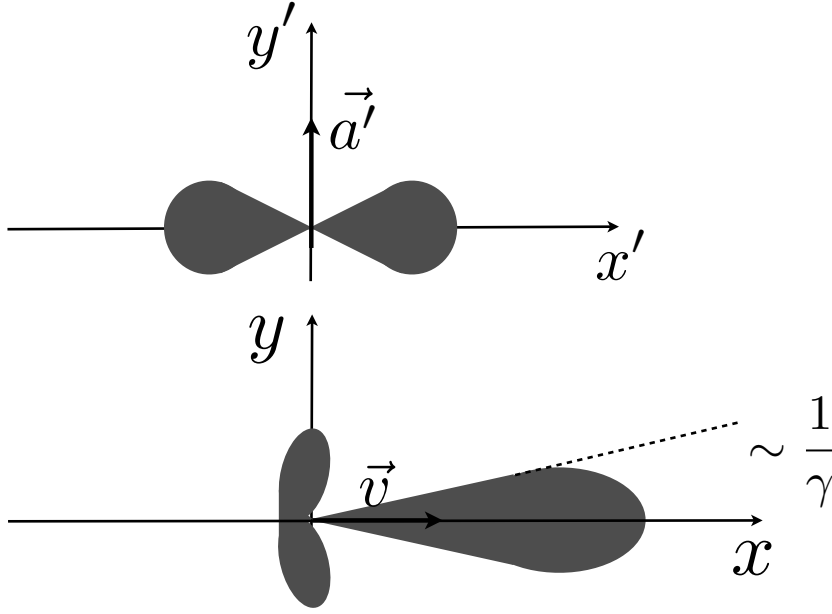


Figure A.1: Relativistic beaming. Upper image represents the geometry and emission pattern in electron rest frame. Lower image represents these in observer frame.

For arbitrary pitch angle $\alpha = \tan v_{\parallel}/v_{\perp}$, the major part of radiation is confined into a small solid angle as is depicted in Figure A.2. This picture is important as the basis of the interpretation of the radiation spectra.

Before we show the radiation spectra of the synchrotron radiation, we briefly review the method of the calculation of the radiation spectra from a relativistic charged particle. It starts from the equation of radiated energy emitted to unit solid angle:

$$\frac{dW}{d\Omega} = \int_{-\infty}^{\infty} |\vec{A}(t)|^2 dt, \quad (\text{A.6})$$

where $A(t)$ is written by the radiation part of the retarded electric field:

$$\vec{A}(t) = \left(\frac{c}{4\pi}\right)^{1/2} [R\vec{E}]_{\text{ret}}, \quad (\text{A.7})$$

where R is the distance from the radiating particle to the observer. We approximate the size of emission region is much smaller than the distance. Performing Fourier transformation of

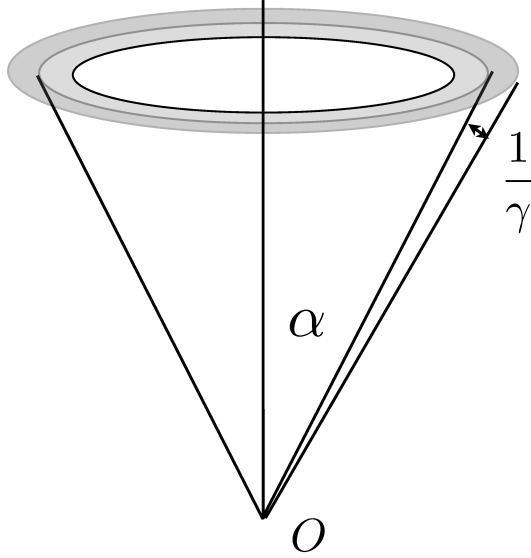


Figure A.2: Synchrotron radiation from a particle located at point O with pitch angle α .

$\vec{A}(t)$, we get

$$\vec{A}(\omega) = \left(\frac{e^2}{8\pi^2 c} \right)^{1/2} \int_{-\infty}^{\infty} e^{i\omega t} \left[\frac{\vec{n} \times \{\vec{n} - \vec{\beta}\} \times \dot{\vec{\beta}}}{(1 - \vec{\beta} \cdot \vec{n})^3} \right]_{\text{ret}} dt, \quad (\text{A.8})$$

where $\vec{\beta} = \vec{v}/c$, and \vec{n} is the unit vector to the observer. On the other hand, the radiated energy per unit solid angle per unit frequency is written as

$$\frac{d^2 I(\omega, \vec{n})}{d\omega d\Omega} = 2|A(\omega)|^2 \quad (\text{A.9})$$

with

$$\frac{dW}{d\Omega} = \int_0^\infty \frac{d^2 I(\omega, \vec{n})}{d\omega d\Omega} d\omega. \quad (\text{A.10})$$

Using the approximation that the distance from the observer to the radiating particle is very far, and changing the variable from the observer time to the retarded time, the radiated energy

per unit solid angle per unit frequency is rewritten as

$$\frac{d^2 I(\omega, \vec{n})}{d\omega d\Omega} = \frac{e^2}{4\pi c} \left| \int_{-\infty}^{\infty} \frac{\vec{n} \times [\{\vec{n} - \vec{\beta}\} \times \dot{\vec{\beta}}]}{(1 - \vec{\beta} \cdot \vec{n})^2} e^{i\omega(t' - \vec{n} \cdot \vec{r}(t')/c)} dt' \right|^2, \quad (\text{A.11})$$

where t' is the retarded time, and $\vec{r}(t')$ is the position of the electron. The distance to observer $R(t')$ is approximated to $|\vec{x}| - \vec{n} \cdot \vec{r}(t')$, where \vec{x} is the vector from the center of the emission region to observer, since $x \gg r$. This equation (A.11) is the basic formula for the radiation spectrum from a charged particle. We use this formula in numerical calculation. One can calculate the radiation spectra by using the information of motion, i.e., the position, the velocity, the acceleration of the particle, and the direction from the observer to the particle.

We use the assumption that particle motion is a gyro motion with constant velocity as we show above, and we get the radiation spectra of synchrotron radiation. Finally, the commonly used synchrotron radiation spectrum is calculated by integrating it over solid angle as

$$\frac{dI}{d\omega} = \sqrt{3} \frac{e^2}{c} \gamma f(x), \quad (\text{A.12})$$

where $f(x)$ is a function of

$$x \equiv 2\omega/3\gamma^3\omega_B \sin \alpha, \quad (\text{A.13})$$

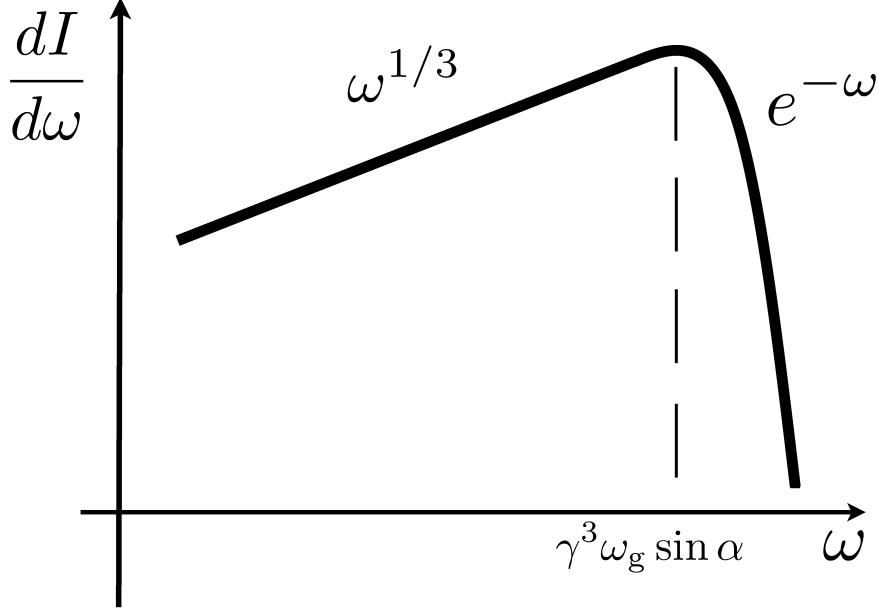
and written by modified Bessel function as

$$f(x) \equiv x \int_x^{\infty} K_{5/3}(\xi) d\xi. \quad (\text{A.14})$$

The radiation spectrum is depicted in Figure A.3. It is characterized by the peak frequency of $\gamma^3\omega_g \sin \alpha$, the spectral index in low frequency region of $1/3$ and exponential cutoff above the peak frequency.

A.2 Useful concepts

Here we introduce useful concepts for a clear interpretation of the radiation spectra.

Figure A.3: Synchrotron radiation spectrum from a charged particle with pitch angle α

A.2.1 Photon Formation Time and Photon Formation Length

First, we review a concept of Photon Formation Time (PFT) or Photon Formation Length (PFL). This concept is introduced by Akhiezer & Shul'ga (1987), to investigate the effect of the scattering on the radiation in amorphous and crystal media. PFT or PFL is the coherent time or length of the photon formation. In general, PFT τ is determined implicitly by using corresponding frequency ω as

$$\omega \times (\tau - |\vec{x}(t + \tau) - \vec{x}(t)|/c) = 2\pi. \quad (\text{A.15})$$

It can be understood as follows. We consider the radiation from a non-relativistic particle, the timescale T of motion and the frequency of the radiation are related as

$$\omega = \frac{2\pi}{T}. \quad (\text{A.16})$$

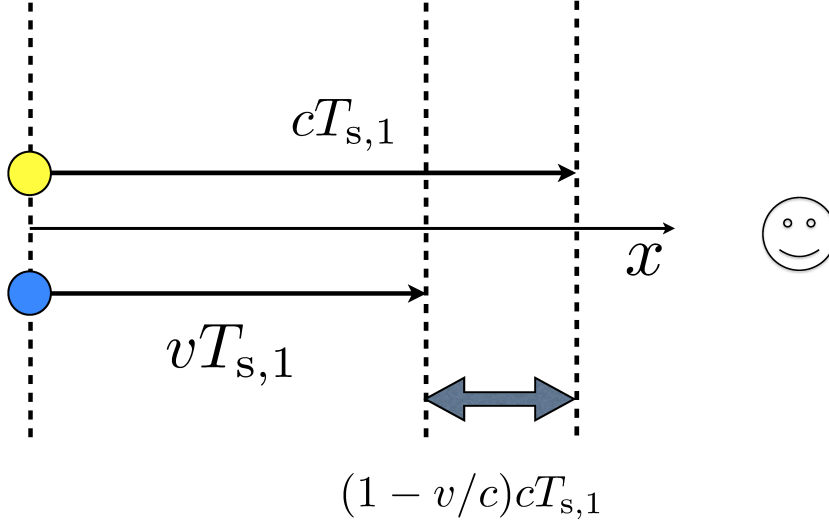


Figure A.4: A relativistic electron chases photon. A yellow filled circle is a photon, and blue filled circle is a electron which emit the photon. Observer sees Doppler-boosted photon.

For example, the correlation of the timescale of the simple oscillation of charged particle and the frequency of the dipole radiation from this particle is written as equation (A.16). However, this relation is not valid for the radiation from a relativistic particle, because the retarded effect is not negligible. When the particle velocity is not negligible compared to the light speed, the radiation frequency ω is affected by the photon chasing effect (Doppler effect). Next we estimate the difference of $1/\omega$ and τ . For simplicity, we consider simple situation when the relativistic charged particle moving along the x -direction with the Lorentz factor γ is perturbed to z -direction with frequency $\omega_{s,1}$. The observer is on the x -direction.

Because of $\beta = v/c \sim 1$, the effect of particle chasing the photon as in Figure A.4 is not negligible. The emitted radiation in the time scale of $T_{s,1} = 2\pi/\omega_{s,1}$ is observed in the timescale $T_{o,1} = T_{s,1}(1 - v/c)$, so that the observed frequency is $\omega_{o,1} = 2\pi/T_{o,1} \simeq 2\gamma^2\omega_{s,1}$. Conversely, the corresponding time of the observed frequency $\omega_{o,2}$ is $T_{s,2} = \tau = 4\pi\gamma^2/\omega_{o,2}$. This is called

Photon Formation Time, and the passing length in PFT is PFL, which is approximated as $c \times$ PFT in many cases for the typical frequency of some radiation mechanisms. However, we note that the PFT is not always $4\pi\gamma^2/\omega_o$ and PFL is not always $v \times$ PFT for the low frequency photon in general complicated trajectory.

We can estimate the observed frequency using the PFT and orbit. For example, the typical (peak) frequency of the synchrotron radiation can be understood as follows. The majority of the radiation energy is concentrated in small beaming cone with angle $\sim 1/\gamma$, and the radiating particle traces gyro orbit. Therefore, the observer sees strong emission in the time scale $\sim 1/\omega_g\gamma = mc/eB$. This is the PFT of the synchrotron radiation. The velocity direction is almost toward the observer in this time span, therefore the observed frequency is $\sim \gamma^2 eB/mc$.

Moreover, the correlation between the beaming cone angle and observed frequency is qualitatively understood by PFT and PFL. The lower frequency corresponds to the larger cone angle. Therefore, PFT of the lower frequency photon is larger than the higher frequency photon. The fact that the correspondence between the frequency and PFT is not linear, which is from the fact that the trajectory is not a straight orbit.

A.2.2 Method of virtual quanta

Here we introduce another useful concept of virtual quanta. It is an approximation of regarding a wave (which is a component of a turbulence) as a photon in the electron rest frame, which is proposed by Weizsacker 1934 and Williams 1934 independently (cf. Jackson 1999). To introduce this concept, we use very simple assumption. A highly relativistic particle with Lorentz factor γ moves along x -axis interacting with a sinusoidal wave $\vec{B}(\vec{k})$, i.e., frequency $\omega = 0$. As an example, we assume

$$B_z(x) = B_{z0} \sin k_x x.$$

Performing the Lorentz transform to the electron rest frame, this wave has not only $B'_z = \gamma B_z$, but also $E'_y = -\frac{v}{c} B_z$, with wavenumber $k'_x = \gamma k_x$. This mode moves to x -direction with

velocity $-v \sim -c$. Thus, the wave in the electron rest frame is almost photon with frequency $\omega' = ck'_x$. Here, we make one more assumption that this wave is "not strong", i.e., satisfies

$$\frac{qE'_{y0}}{mc\omega'} \ll 1, \quad (\text{A.17})$$

where E'_{y0} is the largest value of the electric field, which is from B_{z0} . When this condition is achieved, the electron in this frame is always non-relativistic while interacting with this wave. Therefore, the electron scatters the "photon" in Thomson regime, so that the frequency of the radiation is not changed from ω' . We perform the Lorentz transformation back to the observer frame, and get the radiation with frequency $\sim \gamma\omega' \sim \gamma^2 k_x c$. We note that the majority of the radiation energy is concentrated into the small cone centered along the velocity direction with solid angle $\sim 1/\gamma^2$, from the relativistic effect (relativistic beaming). This picture is quite similar to the inverse Compton scattering, therefore this mechanism is called "Inverse Compton scattering of the plasmon", and this method is called "The method of the virtual quanta (photon)".

A.2.3 Wiggler and Undulator

In the field of laboratory experiments, the radiation from an electron which moves in non-uniform magnetic field is well studied using the insertion device of synchrotron orbital radiation factory, where a series of magnets are line-upped to make the particle deflect periodically. It is called "Wiggler" or "Undulator" (see e.g. Jackson 1999). For Undulator, the strength of magnets B and gaps between them λ are chosen to satisfy the condition that the observer is always in the beaming cone. On the other hand, for Wiggler, the observer is periodically in and off the beaming cone. We estimate the critical distance λ_c which divides Wiggler and Undulator. The deflection angle in one deflection is $\theta_{\text{def}} = \lambda/r$, where $r \simeq \gamma mc^2/eB$ is the typical curvature radius of the orbit. The radiation from a relativistic particle is concentrated into small cone with opening angle $\sim 1/\gamma$. Therefore, the critical condition dividing the Wiggler and Undulator is $\theta_{\text{def}} = 1/\gamma$, which is rewritten as $\lambda_c = r/\gamma$. Thus, the device is

called Undulator when $\lambda < \lambda_c$, while it is called Wiggler when $\lambda > \lambda_c$. The radiation spectrum of Undulator shows a sharp peak at $\gamma^2 2\pi c/\lambda$, while Wiggler shows a broad spectrum with peak frequency $\sim \gamma^2 eB/mc$. The relation between typical frequencies and deflection angle is a key point for understanding of the radiation spectra. Perturbative jitter radiation or perturbative DSR is recognized as extensions of the Undulator radiation, since the spatial scale of turbulence λ is assumed to be much smaller than mc^2/eB . The original jitter radiation (Medvedev 2000) is almost identical to the Undulator radiation, because a single mode dominates the turbulent magnetic field in his treatment. We note that some review of the radiation spectra of Wiggler and Undulator are shown in Appendix C

Appendix B

Details of Past Studies

In this appendix B, we describe the theoretical studies for the radiation from a relativistic charged particle moving in turbulent electromagnetic field related to our study in this thesis.

We have reviewed the synchrotron radiation in Appendix A, which is the radiation mechanism from a relativistic particle moving in a uniform magnetic field. We first review the case when magnetic field is non-uniform. Next we review the applications of the theories to the high energy astrophysical objects. Although many researchers (especially in Russia) have examined the radiation signatures (e.g. Tsytovich & Chikhachev 1969, Melrose 1971, Ginzburg & Tsytovich 1980, Toptygin & Fleishman 1987, and references therein), the application has not been discussed actively.

Medvedev rediscovered the radiation signatures from a relativistic electron in small scale magnetic turbulence, and applied to GRBs, by naming it "jitter radiation" (Medvedev 2000). This study is important, because it has attracted the attentions of researchers to the radiation processes. Moreover, this process is on the very simple configurations, so that we start from the review of the jitter radiation.

B.1 Jitter radiation

Medvedev and Loeb (1999) examined Weibel (or filamentation) instability at the relativistic ion-electron shock in the context of Gamma ray bursts (GRB). Medvedev (2000) claimed that the radiation from an accelerated electron at this shock is different from the synchrotron radiation because the spatial scale of the generated magnetic field is very small and electrons would not trace a helical orbit. The strength parameter a is estimated to $O(10^{-1})$ by Medvedev, so that he approximated $a \ll 1$ for calculation of the radiation spectra.

Medvedev derived a radiation formula for $a \ll 1$, which is same expression as Landau & Lifshitz 1980. Physical picture is as follows. The electron moves almost straightly at almost constant velocity, but it is shaken perpendicularly to the velocity, so called "jittering". The perpendicular component of the velocity is very small, and it is also non-relativistic in the mean velocity frame. By an analytical treatment of the radiation from this particle, he started from the formula (A.11) with the approximation of $\gamma \gg 1$ and $a \ll 1$. In other words, he assumed that the electron trajectory is straight and that the observer is always in the beaming cone. The acceleration is treated as a perturbation, so that the change of the velocity is omitted. We use the electron rest frame and the mean velocity frame as an identical meaning hereafter, since there is no difference in Medvedev's treatment. The angle integrated radiation spectra is approximated as

$$\frac{dW}{d\omega} = \frac{e^2\omega}{2\pi c^3} \int_{\omega/2\gamma^2}^{\infty} \frac{|\vec{w}_{\omega'}|^2}{\omega'^2} \left(1 - \frac{\omega}{\omega'\gamma^2} + \frac{\omega^2}{2\omega'^2\gamma^4}\right) d\omega', \quad (\text{B.1})$$

where the $\vec{w}_{\omega'}$ is a Fourier component of the acceleration, and $\omega' = \omega(1 - \beta \cos \theta)$ expresses the photon chasing effect, and θ is the angle between the observer and photon emission direction in the observer frame. As you see at the relativistic Doppler boost effect, the observed frequency is the function of the emission angle. ω' is approximated as

$$\omega' = \omega(1 - \beta \cos \theta) \simeq \omega \left(1 - \beta + \frac{\theta^2}{2}\right) \simeq \frac{\omega}{2} \left(\frac{1}{\gamma^2} + \theta^2\right), \quad (\text{B.2})$$

where we used $\theta \ll 1$, because the emission from the relativistic particle is concentrated into

the small beaming cone.

He assumed an 1D distribution for the magnetic field as

$$B(k) = \begin{cases} C_B k^{-\mu} & \text{for } 0 \leq k \leq k_{\text{typ}} \\ 0 & \text{otherwise} \end{cases} \quad (\text{B.3})$$

where k_{typ} is the typical wavenumber of the generated turbulence, C_B is a normalization constant, and $\mu \geq 1$, so that the mode $k \simeq k_{\text{typ}}$ is dominant. This is an important difference with the turbulence which Fleishman used (e.g. Flesihman 2006). He further assumed that the velocity and the magnetic field are perpendicular. On the above setting, he solved the equation of motion and performed the Fourier transform of the acceleration. Substituting it to the equation B.1, he got the radiation spectrum. The peak frequency is about $\gamma^2 k_{\text{typ}} c$. The lower frequency region is written by power law with index 1, and higher frequency region shows abrupt cutoff.

The typical frequency is understood by using the method of virtual quanta. The mode with wavenumber k_{typ} is a quasi photon with frequency $\sim \gamma k_{\text{typ}} c$ in the electron rest frame. Therefore, the frequency of the scattered photon in the observer frame is $\sim \gamma^2 k_{\text{typ}} c$. The abrupt cutoff in the higher frequency region is understood, because the higher wave number than k_{typ} does not exist. As for the low frequency spectrum, we show only the physical picture and omit the detail explanation of the index of 1, since it is rather redundant. As is shown in the appendix C, the low frequency region than $\gamma^2 k_{\text{typ}} c$ with a power law index of 1 is the weakly beamed emission (Figure B.1). In other words, this low frequency photons are emitted larger angle than $1/\gamma$. The radiation frequency in the electron rest frame is $\gamma k_{\text{typ}} c$, therefore, the spectrum in the observer frame comes from the beaming effect. The observer in a specific direction to the velocity observes the monochromatic emission. Their frequency corresponds to the angle between the velocity and the line of sight. This picture is same as inverse Compton scattering of the monochromatic emission by a single particle. The angle integrated radiation spectrum is same as this jitter radiation.

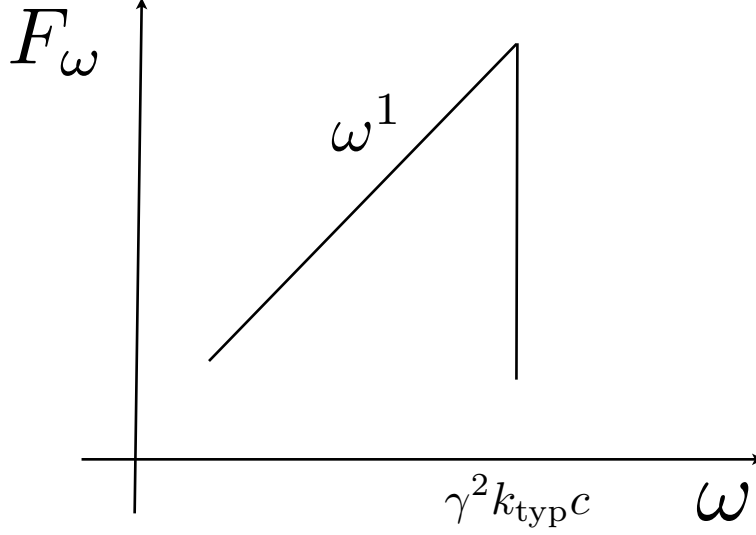


Figure B.1: The radiation spectrum of the 1D jitter radiation (Medvedev 2000). The maximum frequency is $\gamma^2 k_{\text{typ}} c$. The frequency region lower than peak shows hard spectrum $F_\omega \propto \omega^1$, and shows abrupt cutoff above the peak.

The jitter radiation can produce the very hard spectrum $P_\omega \propto \omega^1$. Medvedev claimed that the Gamma ray bursts which have very hard spectra $F_\omega \propto \omega^1$ may be explained by jitter radiation mechanism. It was big impact to the society of the high energy astrophysicists. However, Fleishman (2006) claimed that it is based on too simplified an assumption of artificial magnetic field configuration (Figure B.2) and the radiation spectrum is rather soft for more general magnetic field configuration. For preparation of the discussion about the validity of the configuration of the magnetic field, we firstly clarify the physical picture which Medvedev assumed. He assumed the emission region is shock surface of $x - y$ plane in the shock front rest frame. Here, we note that Medvedev omitted downstream bulk velocity in the shock front rest frame, since he implicitly assumed that the shock is kinetically dominated, so that the downstream velocity is sub-relativistic. The observer is in the x -direction in this frame. The

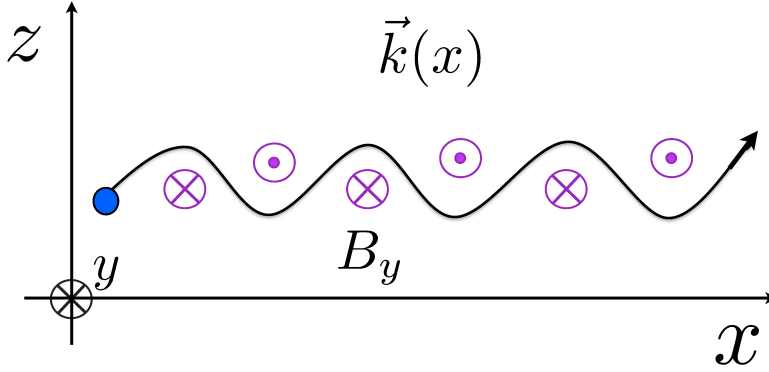


Figure B.2: A cartoon of the configuration of electron and magnetic field which Medvedev (2000) used.

magnetic field is B_y with the wavenumber k_x . The velocity is v_x , so that acceleration is a_z . The electron interacting with $B_y(k_x)$ and radiate the emission to the x-direction. For this situation, the observer observes the hard spectrum $F_\omega \propto \omega^1$ of the jitter radiation.

Next, we discuss the validity of his assumptions. He claimed that one dimensional jitter radiation dominated the GRB emission on the basis of the limb brightening effect (Panaitescu & Meszaros 1998). However, it is rather misleading, because the velocity distribution of radiating electron would be nearly isotropic in the downstream rest frame, so that large part of the emission is from the electrons having v_z components (Figure B.3). Moreover, the filamentation instability restricted the direction of wavenumber to the perpendicular direction to the beam, therefore, k_y should also exist. From the general treatment of the instability of the relativistic two-stream plasma by Bret et al. (2004, 2005), the wavenumber generally has all component of \vec{k} . Thus, the Medvedev's treatment must be over simplified one. Although his treatment

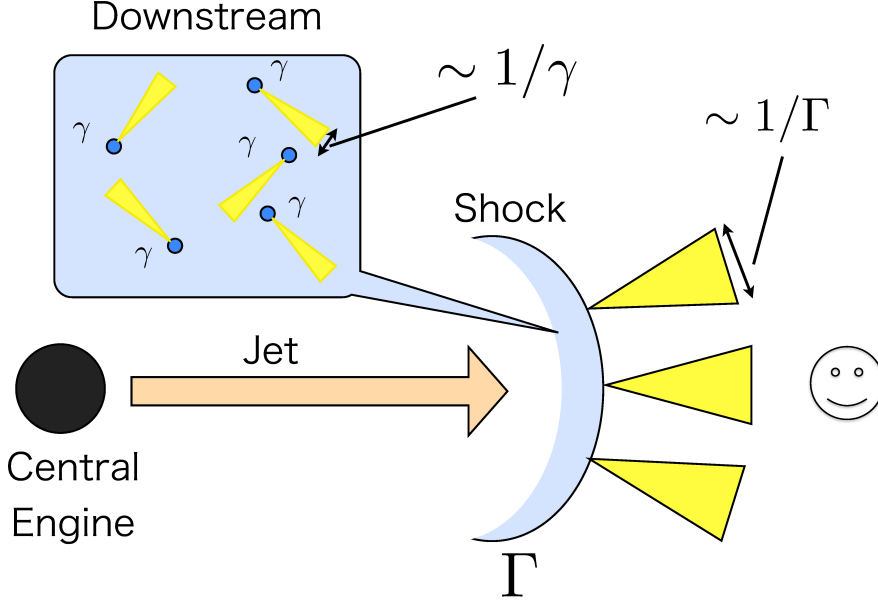


Figure B.3: A cartoon of the emission region of the GRB on standard scenario of internal shock.

would fail to explain the GRB, he attained important work of shedding light to the radiation mechanism for the high energy astrophysics.

B.2 Multi dimensional jitter radiation and Diffusive Synchrotron Radiation

Fleishman (2006) claimed that the multi dimensional magnetic turbulence must be used for the radiation spectra from the situation as we see in the former section. His treatment is based on the sophisticated statistical method which was developed by Toptygin & Fleishman (1987). It is a calculation method for radiation spectrum from a single relativistic charged particle and ensemble of particles moving in very small or very large random electromagnetic fields¹. There

¹there is an inapplicable regime in intermediate scale for their treatment, which is shown in chapter 5

treatment for small scale magnetic field is suitable for magnetic turbulence with $a \ll 1$.

First, we note that the treatment of the uniform and turbulent magnetic fields. They call the components with $k > k_*$ small scale components, while the opposite large scale components. The critical wavenumber k_* is defined by somewhat ambiguous inequality $R \gg k_*^{-1} \gg R/\gamma$, where R is the local or mean Larmor radius. However, in reality they treat each component for the calculation as

$$\begin{cases} k^{-1} < R/\gamma & \text{small scale components} \\ k^{-1} \gg R & \text{large scale components.} \end{cases} \quad (\text{B.4})$$

Thus, there is an ignored wavenumber region $R/\gamma < k^{-1} < R$. This is important for the chapter 5, because we investigate the radiation spectra for this intermediate scale turbulence. Hereafter we define small scale/large scale components by equation (B.4), and we define components with $R > k^{-1} > R/\gamma$ as intermediate scale components. For large scale scale components, the radiation is written by synchrotron radiation, therefore we omit the discussion. We show the treatment by Fleishman (2006) based on Toptygin & Fleishman (1987) for the small scale components. The superposition of the large and small components are discussed in chapter 5.

The formula for the radiation spectrum is the formula (B.1), which is same as Medvedev's treatments. We write it again for convenience.

$$\frac{dW}{d\omega} = \frac{e^2\omega}{2\pi c^3} \int_{\omega/2\gamma^2}^{\infty} \frac{|w_{\omega'}|^2}{\omega'^2} \left(1 - \frac{\omega}{\omega'\gamma^2} + \frac{\omega^2}{2\omega'^2\gamma^4} \right) d\omega'.$$

To get the Fourier components of the acceleration $|w_{\omega'}|$, Fleishman treated it statistically, by using correlation function of the turbulent magnetic fields as is shown below. We show short review of his treatment. The orbit is approximated as rectilinear

$$\vec{r} = \vec{r}_0 + \vec{v}t.$$

The force acting on the moving particle is expressed by

$$\vec{F}(\vec{r}_0 + \vec{v}t, t) = \int e^{-i(\omega t - \vec{k} \cdot \vec{r}_0 - \vec{k} \cdot \vec{v}t)} \vec{F}_{q_0, \vec{q}} d q_0 d \vec{q}. \quad (\text{B.5})$$

Then the Fourier component $\vec{F}_{\omega'}$ specifying the magnitude $\vec{w}_{\omega'} = \vec{F}_{\omega'}/m\gamma$ is found by temporal Fourier transformation. We write the square of $\vec{w}_{\omega'}$ as

$$|\vec{w}_{\omega'}|^2 = \frac{(2\pi)^3}{m^2\gamma^2V} \int dq_0 d\vec{q} \delta(\omega' - \omega + \vec{k} \cdot \vec{v}) |\vec{F}_{q_0, \vec{q}}|^2, \quad (\text{B.6})$$

where V is the source Volume. Next we specify the field as a random static magnetic field as

$$\vec{F}_{q_0, \vec{q}} = e^2(\delta_{\alpha\beta} - v_\alpha v_\beta/v^2) B_{\vec{q}}^\alpha B_{\vec{q}}^\beta.$$

We introduce the second-order correlation tensor of the statistically uniform random magnetic field as

$$K_{\alpha\beta}^{(2)}(\vec{r}) = \frac{1}{V} \int d\vec{R} B_\alpha(\vec{R}) B_\beta(\vec{R} + \vec{r}), \quad (\text{B.7})$$

and the $|\vec{w}_{\omega'}|$ is obtained from Fourier transformed correlation function. Substituting $|\vec{w}_{\omega'}|$ into equation (B.1) and dividing it by the total duration time T , we get the radiation intensity:

$$\frac{dI}{d\omega} = \frac{e^4}{m^2 c^3 \gamma^2} \int_{1/2\gamma^2}^{\infty} d\left(\frac{\omega'}{\omega}\right) \left(\frac{\omega}{\omega'}\right)^2 \left(1 - \frac{\omega}{\omega'\gamma^2} + \frac{\omega^2}{2\omega'\gamma^4}\right) \int d\vec{q} \delta(\omega' + \vec{q} \cdot \vec{v}) K(\vec{q}), \quad (\text{B.8})$$

where $K(\vec{q}) = K_{\alpha\beta}^{(2)}(\vec{q})(\delta_{\alpha\beta} - v_\alpha v_\beta/v^2)$. By specifying $K(\vec{q})$, we get the radiation spectrum. We show the spectral features using equation (B.8). We here consider the isotropic case $K_{\alpha\beta}^{(2)} \propto (\delta_{\alpha\beta} - q_\alpha q_\beta/q^2) f(|\vec{q}|)$ with spectrum of the random magnetic field:

$$f(|\vec{q}|) = \frac{q^2}{(q_m^2 + q^2)^{\mu/2+2}}. \quad (\text{B.9})$$

It expresses a broken power law distribution with the break frequency of q_m , the low frequency side is $B^2(k) \propto k^4$ and high wavenumber side is $B^2(k) \propto k^{-\mu}$. When $\mu = 5/3$, the magnetic field is the well known Kolmogorov turbulence. For $\omega \gg \gamma^2 q_m c$, the corresponding wavenumber is much higher than q_m . Integrating equation (B.8) with using power spectrum of turbulence (B.9), one obtains $dI/d\omega \propto \omega^{-\mu}$. The high frequency component is from the resonance contributions of the modes $q = \omega'/v$. On the other hand, for $\omega \ll \gamma^2 q_m c$, the spectrum consists of non resonant contribution of the mode q_m . The integral of the corresponding part to making the spectral index in equation (B.8) is

$$\int d\vec{q} f(|\vec{q}|) \delta(\omega' + \vec{q} \cdot \vec{v}) = \frac{1}{v} \int dq_y dq_z f(q_y^2 + q_z^2 + (\omega'/v)^2), \quad (\text{B.10})$$

where we specify $\vec{v} = (v_x, 0, 0)$. Since we now treat $\omega' \ll q_m c$, the $f(|\vec{q}|)$ very weakly depends on ω' . Thus, $dI/d\omega \propto \omega^0$ for the low frequency region than $\gamma^2 q_m c$. Summarizing above, except for the special configuration of $\vec{k} \parallel \vec{v}$, the radiation spectrum is $F_\omega \propto \omega^0$ in lower frequency region than $\gamma^2 q_m c$, and $F_\omega \propto \omega^{-\mu}$ in higher frequency region. He call the treatment above perturbative Diffusive Synchrotron Radiation theory (DSR).

B.3 Beyond the perturbative DSR theory

The Fleishman's treatment of DSR theory is appropriate under the approximation that the magnetic turbulence is static and that the radiating particle is moving rectilinearly. These are, of course, not general. When these assumptions does not hold, the radiation spectra are significantly changed as we show as follows and in main part of this thesis. Moreover, the electric field would also be generated at the shock region, which is demonstrated in PIC simulations, for example Dieckmann (2005).

We firstly discuss the break of the approximation of the rectilinear trajectory, which is also studied in Fleishman 2006. The condition $k^{-1} < R/\gamma$ means only that the change of deflection angle in the electron passing time of an eddy is smaller than $1/\gamma$. Therefore, when the particle moves longer scale, the observer may be off the typical beaming cone. As a result, the approximated formula breaks down for the calculation of lower frequency region. Here we estimate the break frequency by calculating the cumulative deflection angle by diffusion approximation. The deflection angle in one deflection is defined as

$$\theta_0 = eBl_0/\gamma mc^2, \quad (\text{B.11})$$

where l_0 is the length of an eddy. By equating cumulative deflection angle θ_c and $1/\gamma$, obtain

$$\theta_c = \sqrt{N}\theta_0 = \frac{1}{\gamma}, \quad (\text{B.12})$$

where N is the number of the deflections. Using the equations (B.11) and (B.12), we estimate

the timescale of which the rectilinear approximation breaks down as

$$1/T \sim \frac{c}{Nl_0} \sim a \frac{eB}{mc}. \quad (\text{B.13})$$

Therefore, the break frequency for the observer is $\sim a\gamma^2 eB/mc^2$. We can imagine that the lower frequency region than that would be dimmer, because the observer is off the beaming cone in the longer time scale. In reality, the spectrum in lower frequency region than the break frequency shows $F_\omega \propto \omega^{1/2}$. More detailed description of this effect will be written in Appendix C. As we firstly claimed, this discussion is made on the assumption of $a < 1$. Then, what spectra will be obtained for $a > 1$? It means $k^{-1} > R/\gamma$, the intermediate region, which is not treated by Toptygin and Fleishman (1987). The answer is shown in the chapter 5.

Next we shortly discuss on the time variability of the fields. We may have to consider the time variability of the electromagnetic turbulence for the high energy astrophysical objects. Because the thermal components of downstream plasma would have relativistic energy for the relativistic shocks. Furthermore, the plasma instabilities which generate the electromagnetic field are not only Weibel/filamentation instability, but also two-stream instability which would play a role in a certain condition (Bret et al. 2006). By this instability, the Langmuir turbulence is generated, which consists of rapidly oscillating electrostatic waves (Langmuir waves). We should not ignore the time variability of the background field in such a case. This is firstly claimed by Gailitis & Chikhachev (1969), and a few researchers have calculated for limited conditions. Fleishman & Toptygin (1987) performed the calculations of radiation spectra of various characters of turbulence. However, the parameter range for calculation was limited.

B.4 Other studies

The basic picture of the radiation mechanisms from an electron interacting with background magnetic field related to our study in this thesis is nearly completed in above sections. Lastly, we review other researches about this topic after the Medvedev presented the idea of jitter

radiation. First we show the applications of the jitter/DSR theory to the various high energy astrophysical objects.

Medvedev and his collaborators continuously examined the GRBs and jitter radiation. The time variability of the spectral hardness of prompt emission (gamma-ray) of GRBs is modeled by the anisotropic magnetic turbulence and anisotropic velocity distribution of electrons (Medvedev, Pothapragada, & Reynolds 2009). The light curve and spectral evolution are calculated both for prompt emission and afterglow (Medvedev et al. 2007, Workman et al. 2008, Morsony et al. 2009). They include many effects, such as the expansion of the shell, electron cooling, and self absorption. They conclude that the light curve in some frequency range is different from the synchrotron case. However, there is no advantage for the interpretation in terms of jitter radiation. For example, some observation shows that afterglow decay in the X-ray region is flatter than the theoretical prediction, or that the decay rates of the X-ray region and optical region are different. The origin of such peculiar features of the afterglow of GRBs has been unresolved. To argue this point would carry us too far away from the purpose of this thesis, we stop discussion about it.

Fleishman and his collaborators applied DSR theory to many astrophysical objects. The main point is that the power law index can be not from the energy distribution of the radiating electrons but from the signatures of electromagnetic turbulence. We reviewed above that the shape of higher frequency region than $\gamma^2 k_{\text{typ}} c$ is determined by turbulent field as

$$F_{\omega} \propto \omega^{-\mu}, \quad (\text{B.14})$$

where μ is the power index of the magnetic turbulence:

$$\begin{cases} B^2(k) \propto k^{-\mu} & \text{for } k_{\text{typ}} \leq k \leq k_{\text{max}} \\ 0 & \text{others} \end{cases} \quad (\text{B.15})$$

When the condition $s < 2\mu + 1$ is satisfied, where s is the power law index of the energy distribution of electrons $dN/dE \propto E^{-s}$, the radiation spectra shows a broken power law shape.

The break frequency is $\gamma_{\text{max}}^2 k_{\text{typ}} c$. He noted that the interknot regions of AGN jet 3C273 and M87 show broken power law spectra in radio region by this radiation mechanism (Fleishman 2006). Furthermore, they also interpret the broadband broken power law spectra of the pulsar wind nebulae. It is well known that the radio spectrum of the Crab nebula is brighter than the theoretical prediction on the assumption of the one zone model (cf. Kennel & Coroniti 1984). Fleishman and Bietenholtz (2007) claimed that the radio components can be reproduced by the DSR mechanism in the strong deflection regime. The important parameter of this strong turbulence is expressed as

$$k_0^{-1} > mc^2/eB. \quad (\text{B.16})$$

It clearly express that the turbulent field is in "large deflection regime". However, they used perturbative formula to calculate the radiation spectra, so that it may be over simplified. They apply this treatment to the GRBs. They create the histogram of the break frequency of the broken power law spectrum (cf. Band function shown in chapter 2) and power law indices, using randomly selected physical parameters from parent distributions. They argue that the created histogram is consistent with the histogram made from observed spectra. However, the corresponding parameter regime of the turbulence which they claim suitable for reproducing the observation is in strong deflection regime. Therefore, this calculation must be recast by using correct radiation spectra for the strong deflection regime. Moreover, they used static magnetic field for this calculation, the time variability should be introduced.

Several papers inspired by the studies mentioned above have been published from the late '00s. They discussed not only the applications to the observation, but also the fundamental clarification of the radiation spectra. We review some of such important works.

Firstly, we review the important suggestion by Kirk & Reville (2010). They claimed the maximum frequency of jitter radiation is lower than that of synchrotron radiation from an accelerated electron in a relativistic shock region by DSA mechanism (Diffusive Shock Acceleration, cf. Drury 1983) in one zone model. This makes a caution that the radiation energy of the jitter radiation has to be estimated with the attainable energy of the radiating electron.

If we assume spatial scale of the field and electron energy independently, we can get any frequency by jitter radiation. However, they showed that this is not correct for one zone case. Their discussion is summarized as follows. We suppose that the relativistic electrons move in the relativistic shock region, where isotropic turbulent magnetic field exist with strength and the wavenumber characterized by the strength parameter $a = eB\lambda_B/mc^2$. For a kinetic reason, the average energy gain per cycle is roughly factor of 2 (Achterberg et al 2001). Equating the energy gain and the radiative loss in one cycle, we get the radiation energy limit:

$$\begin{cases} \hbar\omega_{\max} = (\alpha_f a_{\text{crit}})^{-1} mc^2, & \text{for } a < 1 \\ \hbar\omega_{\max} = a(\alpha_f a_{\text{crit}})^{-1} mc^2, & \text{for } 1 < a < a_{\text{crit}} \\ \hbar\omega_{\max} = \alpha_f^{-1} mc^2, & \text{for } a > a_{\text{crit}} \end{cases} \quad (\text{B.17})$$

where $\alpha_f = e^2/\hbar c$ is the fine-structure constant, and a_{crit} is the critical strength parameter, which is the maximum attainable Lorentz factor and is typically much larger than unity. The case $a > a_{\text{crit}}$ corresponds to $\lambda \gg \gamma_{\max} mc^2/eB$, and all the electrons are transported helically and cooled through the synchrotron radiation. The maximum value of the synchrotron radiation does not depend on the magnetic field strength for this case. This is an important fact for the Crab gamma ray flare, which is discussed in chapter 7. Furthermore, we emphasize that this discussion is on the assumption that the emission region is isotropic, and this assumption may not always be adopted.

From the view point of the analytical calculation of the radiation spectra from charged particles moving in turbulent fields, the calculation methods have not been improved from the Toptygin & Fleishman (1987). However, their kinetic equation is too complex to obtain the analytical solution. Kelner et al. (2013) improved it and make it easy to treat analytically. Their method is in the frame work of the perturbative treatment. Therefore, the validity range for the strength parameter limited to $a < 1$. They treat the radiation for $a > 1$ is a simple synchrotron formula. However, it is not rigorous treatment as is shown in chapter 5.

Using the analytical perturbative treatment, Mao & Wang (2012, 2013) tackled the obser-

vational features of GRBs which are hard to reproduce by synchrotron radiation. In Mao & Wang (2012), they claimed that the GeV excess of the prompt emission originates from jitter self Compton (JSC) radiation. In Mao & Wang (2013), they calculated the polarization degree of the jitter radiation on the assumption of 2-dimensional orientation of the magnetic field. They claimed that the model can reproduce the high degree polarization which is reported recently (Yonetoku et al. 2012). They proposed a possible scenario where the high energy emission of GRBs is emitted by jitter mechanism.

Next we review the numerical approaches of the calculation of radiation spectra. Using the numerical methods, we can calculate more general cases for electromagnetic turbulences. Moreover, we calculate the radiation spectra for which any approximation is not applicable. We take this approach as a main method for calculation in this thesis. The numerical approach is firstly introduced by Hededal (2005), and our method is identical with it. This treatment is most rigorous, but very numerically expensive.

Reville & Kirk (2011) focused attention on the PFT, and use very reasonable approximation. As a result, a cost of original Hededal's method is cut significantly. They analytically derived the fact that we do not have to pursue the motion in the very short time step defined by the observing frequency. In the Hededal's method, the time step is determined by the inverse of highest frequency we intend to calculate. Reville & Kirk clarified that required time step depends on the frequency. When we want to obtain F_{ω_1} , we may use the time step roughly (PFT for ω_1)/25 for calculation. Therefore, we can use different time step for different frequency. We can cut a cost drastically for highly relativistic case. For example, the typical frequency of the synchrotron radiation is $\gamma^2 eB/mc = \gamma^2 \omega_{\text{cyc}}$, therefore the time step in the Hededal's method is $\sim (\gamma^2 \omega_{\text{cyc}} \times 10)^{-1}$, while in Reville's method it is the order of $\sim (\omega_{\text{cyc}} \times 10)^{-1}$. Their method is applicable when the deviation from the rectilinear orbit is not very large. For jitter radiation regime $a \ll 1$, the deviation in PFT for ω is negligible for $\omega \sim \gamma^2 k_0 c$. For synchrotron radiation regime $a > \gamma$, their method is also applicable for the frequency region $\sim \gamma^2 eB/mc$, because the deviation from rectilinear trajectory in the time scale of mc/eB is very small. To

summarize, their method is applicable regardless of a , but the applicable range is limited to higher frequency region and the frequency where the approximation becomes worse depends on a . However, the deviation is proportional to $1/\gamma$, therefore the wide range of the radiation spectra can be calculated by this method for $\gamma \gg 1$.

We lastly note that Fleishman also developed fast calculation code, which, however, is optimized for mildly relativistic particles. The radiation from mildly relativistic charged particles gyrating in $a > \gamma$ magnetic field is called as "gyrosynchrotron radiation", the spectrum for which shows higher harmonics clearly, and it is observed in solar or stellar flares. Although this radiation mechanism apparently unrelated our study in this thesis, it is important for the deep understandings.

Appendix C

Physical Interpretations of Spectral Indices in Various Regions Considered in this Thesis

In this appendix C, we show the examples of the interpretation of the spectral indices for various parameter ranges. The review of other researcher's interpretation and our original interpretation is given.

C.1 Undulator

The Undulator is an insertion device of the intense high energy emission, which is shortly reviewed in Appendix A. Here we show the spectral indices of the Undulator spectrum.

We assume a relativistic electron moving toward z -direction, and magnets are line upped along z axis with the gaps of the $\lambda = 2\pi/k_0$. The electron deflects in the x -direction and the deflection angle θ_{def} is much smaller than $1/\gamma$. In the mean velocity (of radiating electron)

frame, the electron can be regarded as a simple harmonic oscillator

$$x' = A \sin(k' \beta c t'),$$

where $k' = \gamma k_0$ is the wavenumber of the radiation in this frame, and A is a constant. The radiation from it is the dipole radiation, and the frequency of it is $\omega_{dp} \simeq k' c$ in this frame, where we approximate $\beta \sim 1$. The emitted energy per unit time into unit solid angle is

$$\frac{dP'}{d\Omega'} = \frac{e^2 c}{8\pi} k'^4 A^2 \sin^2 \Theta, \quad (\text{C.1})$$

where $\Theta = \vec{n}' \cdot \ddot{\vec{x}}'$ is the angle between the emission direction and second derivative of the dipole moment. We transform the radiation to the observer frame and make a few approximation for $\gamma \gg 1$, such as $\beta \sim 1 - 1/2\gamma^2$, we get

$$\frac{d^3 P}{d\chi dk d\phi} = \frac{e^2 c \gamma^4 k_0^4 A^2}{2\pi} \left[\frac{(1 - \chi^2) + 4\chi \sin^2 \phi}{(1 + \chi)^4} \right] \delta[k(1 + \chi) - 2\gamma^2 k_0], \quad (\text{C.2})$$

where $\chi = (\gamma\theta)^2$ is an angle variable, $\delta[\dots]$ is the Dirac delta function, and θ' and ϕ' are Lorentz transformed θ and ϕ , respectively. The orientations of θ and ϕ are depicted in Figure C.1. We note that there is a correlation between θ and frequency. We integrate of ϕ and χ in the integration range $0 < \chi < \chi_{\max}$, and we get the radiation spectrum:

$$\frac{dP}{d\nu} = P_0 [\nu(1 - 2\nu + 2\nu^2)], \quad (\nu_{\min} < \nu < 1) \quad (\text{C.3})$$

where P_0 is a normalization constant, $\nu = kc/2\gamma^2 k_0 c$ is the normalized frequency, and $\nu_{\min} = 1/(1 + \chi_{\max})$. We note that we implicitly assumed $\theta \ll 1$, so that χ_{\max} cannot be much larger than $1/\gamma$. The peak frequency of this spectrum is $\nu = 1$ ($\omega_{\max} = 2\gamma^2 k_0 c$). The spectrum in frequency region lower than peak ($\nu \ll 1$) is $dP/d\nu \propto \nu^1$, while the spectrum shows abrupt cutoff above the peak. We note that the spectrum shows $dP/d\nu \propto \nu^3$ in the very narrow frequency range slightly lower than the peak ($\nu \lesssim 1$). The radiation in this frequency range corresponds to the very small angle $\theta \ll 1/\gamma$. Summarizing above, the radiation from Undulator is a dipole radiation with frequency $\gamma^2 k_0 c$ in the mean velocity frame. The spectral

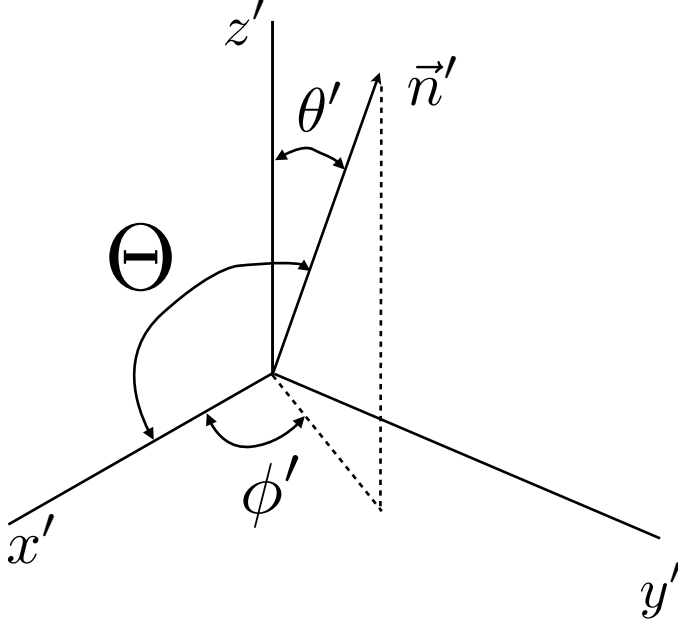


Figure C.1: Coordinate for consideration of radiation spectrum. The electron trajectory is on the $x - z$ plane

feature in the observer frame originates from relativistic aberration. We note that the angle integrated radiation spectra of the inverse Compton scattering also have same spectral index of 1, since the physical condition resembles Undulator.

C.2 Jitter radiation

We next discuss the spectral indices of the jitter radiation. Although the jitter radiation is firstly proposed by Medvedev (2000), the concepts of the physical mechanism have been studied earlier by several researchers such as Landau & Lifshitz (1971), Toptygin & Fleishman (1987). Fleishman (2006) pointed out this fact and he call this mechanism DSR. For simplicity, we here adopt "jitter radiation" as the name of this process, but there is no difference between jitter radiation and DSR in a broad sense.

C.2.1 One-dimensional jitter radiation

The mechanism which makes spectral feature of $P_\omega \propto \omega^1$ for one-dimensional jitter radiation is same as that of Undulator. Medvedev (2000) assumed one dimensional dependence of the turbulence and the radiating charged particle moves along the wavevector. Rigorously speaking, a further constraint that the narrow range of the Fourier modes of around the typical wave number dominates the turbulence was adopted. Therefore, the spectral shape becomes $P_\omega \propto \omega^1$ under almost the same condition as Undulator.

C.2.2 Multi dimensional jitter radiation

We next discuss the jitter radiation from an electron in a multi dimensional turbulence, i.e., the magnetic field is depicted as $\sum \vec{B}_i(\vec{k}_i)$. The spectrum shows the feature $P_\omega \propto \omega^0$ for isotropic turbulence. This spectral shape emerges in frequency region lower than $2\gamma^2 k_{\text{typ}} c$. This is the standard radiation signature of jitter radiation, since the turbulences have multi dimensional structure, and the radiation spectra from ensemble of electrons with isotropic velocity distribution mimic angle integrated spectra. From this view point, even if the direction of wave number is one dimensional, the radiation from ensemble of particles realizes this $F_\omega \propto \omega^0$ radiation spectrum. The reason of it is seen as follows.

We have already reviewed the analytical DSR and derived $P_\omega \propto \omega^0$ in Appendix B. Therefore, we show more intuitive explanation here. From equation B.8, we extract important part for the frequency region lower than $\gamma^2 k_{\text{typ}} c$.

$$\frac{dP}{d\omega} \propto \int_{1/2\gamma}^{\infty} d\left(\frac{\omega'}{\omega}\right) \left(\frac{\omega}{\omega'}\right)^2 \int d\vec{q} \delta(\omega' + \vec{q} \cdot \vec{v}) K(\vec{q}) \quad (\text{C.4})$$

We see the second integral as an interaction the electron with field. When the second integral does not depend on ω' , that is, there is non-resonant contributions of the field to the electron, the spectrum becomes $dP/d\omega \propto \omega^0$. This can be satisfied when $\omega' \ll k_{\text{typ}} c$ in a turbulence with multi dimensional dependence, because the power law distribution of the turbulence has a peak at k_{typ} , so that the value of second integral weakly depends on the ω' .

We note that the $dP/d\omega \propto \omega^1$ is easily derived from this equation when we assume a perfectly harmonic motion. The electron trace a simple harmonic motion as Undulator with wavenumber q_{und} , the second integral is proportional to

$$\int d\vec{q} \delta(\omega' + \vec{q} \cdot \vec{v}) \delta(\vec{q} - \vec{q}_{\text{und}}) = \delta(\omega' + \vec{q}_{\text{und}} \cdot \vec{v}). \quad (\text{C.5})$$

We substitute it to the equation (C.4), we get $dP/d\omega \propto \omega^1$ spectrum.

The spectrum $F_\omega \propto \omega^{-\mu}$ in frequency region higher than $\gamma^2 k_{\text{typ}} c$ is also understood easily. The index μ is from the power law index of the turbulent field $B^2(k) \propto k^{-\mu}$. For $\omega' > k_{\text{typ}} c$, the power law distribution for the high wavenumber region is $B^2(k) \propto k^{-\mu}$. Therefore, the Fourier amplitude of the acceleration is $\propto k^{-\mu}$. As a result, we obtain $dP/d\omega \propto \omega^{-\mu}$. In other words, the field components for $k = \omega'/v$ resonantly contribute to make a radiation spectrum.

C.2.3 LPM effect on the jitter radiation

We lastly show the interpretation of $F_\omega \propto \omega^{1/2}$. It is from the break of the perturbative approximation, which is well known as LPM effect (Landau & Pomeranchuk 1953, Migdal 1956). Here, we derive the index of 1/2 on the assumptions that the deflection is written by a part of the circular orbit, and the deflection angle in one deflection $\theta_{\text{def}} = \frac{e\sigma}{\gamma mc^2} \lambda$, that the strength parameter is $a < 1$, and that the angle deflection of electron can be written in diffusion formula.

Consider an electron moving toward the observer at $t = 0$. The angle between the direction toward observer and the electron velocity at t is denoted by θ . The probability of θ being in a range $[\theta, \theta + d\theta]$ is written by using diffusion approximation:

$$P(\theta, t) = \frac{1}{\sqrt{4\pi Dt}} \exp\left(-\frac{\theta^2}{4Dt}\right) d\theta, \quad (\text{C.6})$$

where D is the diffusion coefficient

$$D = \theta_{\text{def}}^2 / 2\tau, \quad (\text{C.7})$$

and $\tau = \lambda/c$ is the PFT of the jitter frequency of $\gamma^2 k_{\text{typ}} c$. When $\theta \gtrsim 1/\gamma$, the observer is out of the beaming cone, and the observed emission becomes dimmer. We substitute $\theta = 1/\gamma$ into the exponential function. The index is rewritten as

$$\frac{1/\gamma^2}{4Dt} = \frac{1}{2at} \frac{mc}{e\sigma}. \quad (\text{C.8})$$

We can approximate exponential part as 1 for the time $t \gg 1/a\omega_{\text{st}}$, which is satisfied when we see the frequency region lower than $a\gamma^2\omega_{\text{st}}$. We approximated the probability as

$$P(\theta) \sim \frac{1}{\sqrt{4Dt}} \propto t^{-1/2}.$$

Using this approximated probability, we obtain the spectrum of $F_\omega \propto \omega^{1/2}$. When we consider ensemble of electrons in $[\theta_0, \theta_0 + d\theta]$, the electron number N which is in this angle range decreases with time $N \propto t^{-1/2}$. We assume $\theta_0 = 0$, i.e., the electrons are moving toward observer at $t = 0$, and $\gamma \gg 1$, so that the observer is off the beaming cone when θ becomes slightly large. In this situation, the electrons which illuminate the observer decrease with $t^{-1/2}$, therefore, the flux decreases with $\propto t^{1/2}$. When we consider the turbulence, the electrons not only be off but also be in the line of site. Therefore, the correlation flux and the time span of illumination by an electron is interpreted by using Fourier transformation as $F_\omega \propto \omega^{1/2}$.

C.3 DRL: small deflection regime

For the Langmuir turbulence, the spectrum $F_\omega \propto \omega^1$ can be realized even if the turbulence has multi dimensional dependence. The condition for realization of this spectrum is that the field oscillation frequency ω_w is the higher than ω_{st} and ω_0 . The reason is understood by the analogy of the 1D jitter radiation. Since the field oscillation frequency does not depend on the direction, the changing rate of direction is the same for each electron. Moreover, we use 3D isotropic turbulence in this thesis. Therefore, the physical condition for electron is same as we discuss in the former section for spatial fluctuation. This condition is expected to realize in

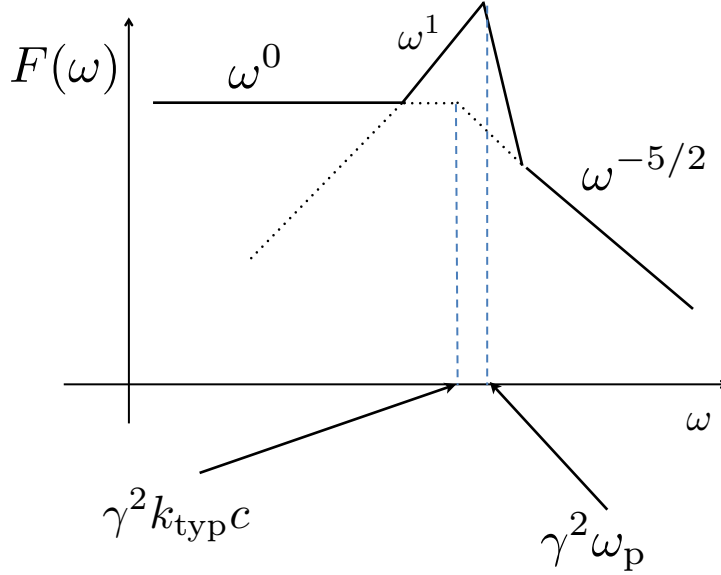


Figure C.2: The radiation spectrum of the DRL. The peak frequency is $\gamma^2 \omega_p$, which comes from the field oscillation effects. The highest frequency region and lowest frequency region is from the effects of spatial fluctuation.

the high energy astrophysical object when Langmuir turbulence is generated by two stream instability.

As we see in chapter 6, $F_\omega \propto \omega^1$ does not extend to lower frequency region, and emerges $F_\omega \propto \omega^0$ spectrum (Figure C.2). The reason can be understood by considering the origin of these spectral shape and the radiation power comes from each radiation mechanism. The spectral shape of $F_\omega \propto \omega^1$ is caused by field oscillation, so that the spectral power at some frequency ω_1 is beamed dipole radiation, where we assume $\omega_1 < \gamma^2 \omega_0 < \gamma^2 \omega_p$. Thus, this radiation comes from electrons moving with some angle toward the observer. The spectral power is proportional to σ^2 , because we assume all the components of the turbulent field has same frequency. On the other hand, the spectral shape of $F_\omega \propto \omega^0$ is caused by spatial fluctuation. The spectral power at ω_1 is dominated by the radiation from the electrons moving

toward observer with $\vec{k}_{\text{typ}} \cdot \vec{v} = \omega_1/2\gamma^2$. The spectral power is proportional to $B(k_{\text{typ}})dk$. Therefore, the spectral shape changes from $F_\omega \propto \omega^1$ to $F_\omega \propto \omega^0$ at the frequency where the spectral power of strongly beamed radiation originating from spatial fluctuation of a few Fourier components of turbulent field dominates the weakly beamed radiation originating from field oscillation of all the components.

C.4 Wiggler radiation: low frequency

The Wiggler spectrum shows $F_\omega \propto \omega^{1/3}$, which is also seen in synchrotron radiation. The mechanism which makes this signature is somewhat different from that for other spectral signatures, which are explained above. The spectral signatures of $F_\omega \propto \omega^0$, $F_\omega \propto \omega^{-\mu}$, and $F_\omega \propto \omega^1$ are on the assumption that the electrons always illuminate the observer. Moreover, the spectral shape $F_\omega \propto \omega^{1/2}$ can be interpreted by simple picture that the electrons is out of the line of sight after multiple deflection. Therefore, we used almost one dimensional trajectory. On the other hand, we have to use at least two dimensional trajectory for the radiation signature for this $F_\omega \propto \omega^{1/3}$ case, because the shape of deflection is essential factor to determine the spectral index of $1/3$.

To explain the index $1/3$, we assume the circular trajectory in the time scale of Nmc/eB , which is N/γ of the gyro time, where N is a real number. We assume $\gamma \gg N$, so that the trajectory we see is a part of the circular orbit. The trajectory is assumed on the $x - y$ plane. We consider the radiation from this electron, the trajectory and coordinate we use for calculation is depicted in Figure C.3. We start the interpretation of the spectral index of $1/3$ from the equation (A.11) we used for the numerical calculation. The argument of the exponential is

$$\omega \left(t - \frac{\vec{n} \cdot \vec{r}(\tau)}{c} \right) \sim \frac{\omega}{2} \left[\left(\frac{1}{\gamma^2} + \theta^2 \right) t + \frac{c^2}{3r_L^2} t^3 \right], \quad (\text{C.9})$$

where r_L is a curvature radius, and we approximate third order of the $c\tau/r_L$. The first order and third order is comparable for $\tau \sim mc/eB$, but fifth order is $1/\gamma^2$ times smaller than them.

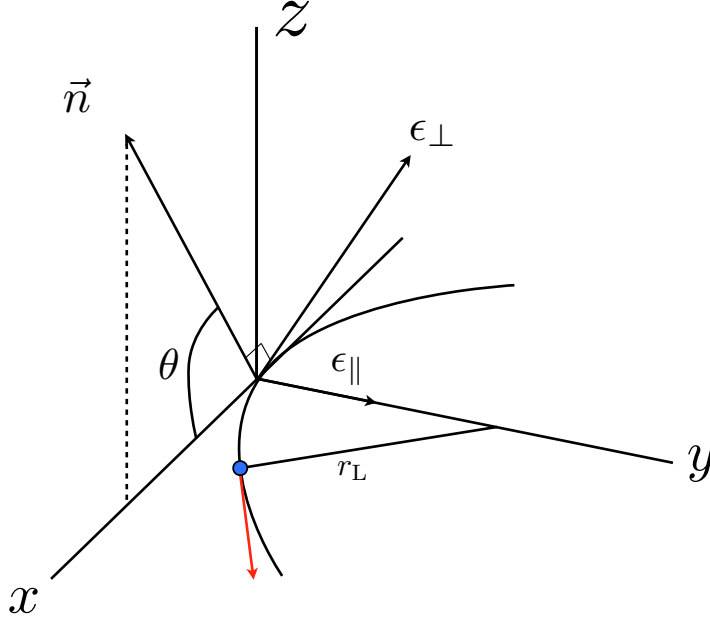


Figure C.3: Coordinate we use for calculations of radiation spectrum. Blue filled circle represent a radiating electron, and \vec{n} is the radiation direction we consider. θ is the angle between \vec{n} and x axis.

We rewrite the equation (A.11) as

$$\frac{d^2 I}{d\omega d\Omega} = \frac{e^2 \omega^2}{4\pi^2 c} \left| -\epsilon_{\parallel} A_{\parallel}(\omega) + \epsilon_{\perp} A_{\perp}(\omega) \right|^2, \quad (\text{C.10})$$

where ϵ_{\parallel} and ϵ_{\perp} are unit vector with direction is depicted in Figure C.3. A_{\parallel} and A_{\perp} are written by modified Bessel functions, so that we get the radiated energy per frequency per unit solid angle is

$$\frac{d^2 I}{d\omega d\Omega} = \frac{e^2}{3\pi^2 c} \left(\frac{\omega^2 r_L^2}{c} \right)^2 \left(\frac{1}{\gamma^2} + \theta^2 \right)^2 \left[K_{2/3}^2(\xi) + \frac{\theta^2}{(1/\gamma^2) + \theta^2} K_{1/3}^2(\xi) \right], \quad (\text{C.11})$$

$$\xi = \frac{\omega r_L}{3c} \left(\frac{1}{\gamma^2} + \theta^2 \right)^{3/2}. \quad (\text{C.12})$$

Since the $K_{2/3}(\xi)$ term dominates in equation (C.11), we see the frequency dependence in low frequency region for $\theta = \theta_1 = \text{const}$ by using $K_{2/3}(\xi)$. We use asymptotic behavior for Bessel

function

$$K_{2/3}(\xi) \propto \xi^{2/3} \text{ for } \xi \ll 1 \quad (\text{C.13})$$

since $\xi \ll 1$ means low frequency. As a result, we get the radiation spectra for an observer in the particular direction is

$$\left. \frac{d^2 I}{d\omega d\Omega} \right|_{\theta=\theta_1} \propto \omega^{2/3}. \quad (\text{C.14})$$

We note that this index of $2/3$ is harder than $1/2$ which we obtained by using angle diffusion. We can understand it by comparing two cases with the same field strength σ , $a < 1$ for one and $a > 1$ for the other. The beaming cone sweeps for $a > 1$ is more quickly than $a < 1$ cases. Therefore, the intensity is weaker for $a > 1$ than for $a < 1$ for the same PFT, i.e., for the same frequency. Thus, the spectrum for $a > 1$ is harder than for $a < 1$.

The modified Bessel function $K_{2/3}(\xi)$ is very small for $\xi \gg 1$. From this property, we define the radiation angle for given frequency by using the constraint $\xi(\theta_c) = 1$ as

$$\theta_c = \left(\frac{3c}{\omega r_L} \right)^{1/3} \propto \omega^{-1/3}. \quad (\text{C.15})$$

Using equations (C.14) and (C.15), we can approximate the angle integrated, well known spectral shape:

$$\frac{dI}{d\omega} = 2\pi \int_{-\pi/2}^{\pi/2} \frac{d^2 I}{d\omega d\Omega} \cos \theta d\theta \simeq 2\pi \int_{-\infty}^{\infty} \frac{d^2 I}{d\omega d\Omega} d\theta. \sim 2\pi \theta_c \left. \frac{d^2 I}{d\omega d\Omega} \right|_{\theta=0} \propto \omega^{1/3}. \quad (\text{C.16})$$

We note that the emission energy is highly concentrated into small θ , since $\gamma \gg 1$.

We organize the points of the mechanism which makes the index $1/3$.

- In the retarded effect which is written in exponential part of the equation (A.11), the third order of vt/r_L is mainly contribute as first order of it. The First order and third order of vt/r_L is both contribute for making the spectrum in low frequency region.
- For fixed angle θ , the radiation spectra is $d^2 I/d\omega d\Omega \propto \omega^{2/3}$.
- For fixed frequency, the radiation spreading angle $\theta_c \propto \omega^{-1/3}$.

- The angle integrated spectrum is obtained by superposing of angle fixed spectrum, and make it softer, since the low radiation is emitted relatively large solid angle. As a result, the spectrum becomes $dI/d\omega \propto \omega^{1/3}$.

Appendix D

Turbulent Electromagnetic Field

In this appendix D, we show the electromagnetic turbulence which is expected to be generated in the emission regions of high energy astrophysical objects. Electromagnetic turbulences are generated by plasma instabilities where the velocity distribution of particles is not Maxwellian, such as shock region and magnetic reconnection region. We firstly show the electromagnetic turbulences in PIC simulations. We secondly review plasma instabilities by using linear analysis.

D.1 Electromagnetic turbulences in PIC simulations

Particle-In-Cell code is a particle code which treats electrons and ions as individual particles. It is suitable to treat kinetic plasma instabilities. We first show the simulations of relativistic collisionless shocks by Sironi & Spitkovsky (2009) in Figure D.1. They use an open PIC code TRISTAN-MP (Buneman 1993) to simulate a relativistic shock propagating into an unmagnetized pair plasma. This shock is triggered by reflecting an incoming cold flow off a conducting wall at $x = 0$. Therefore, this simulation is performed in downstream frame. The incoming flow propagating along $-\vec{x}$ with Lorentz factor $\gamma_0 = 15$. The spatial scale is normalized by non relativistic inertial length c/ω_p . There is a shock front at $x = 1000$.

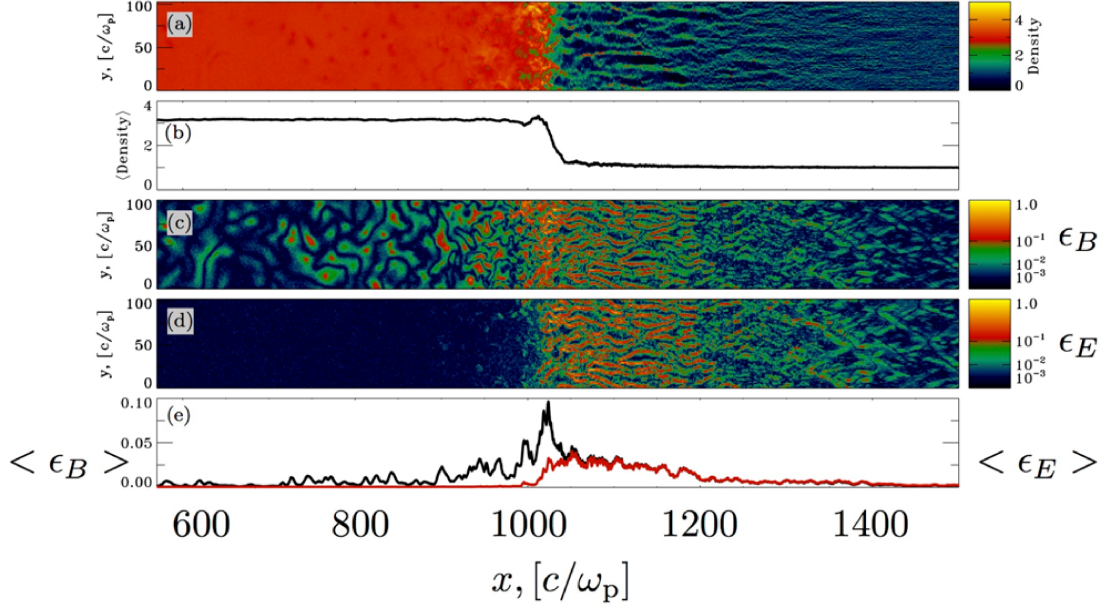


Figure D.1: Shock structure produced using 2D PIC simulation by Sironi & Spitkovsky (2009). (a) Number density in the simulation plane, normalized to the upstream density. (b) Transversely (y -direction) averaged density. (c)-(d) Magnetic and electric energy density in the simulation plane, normalized to the upstream kinetic energy density. (e) Transversely averaged magnetic (black) and electric (red) energy density.

The magnetic field is generated around the shock front, and electric field is also generated in this frame. The characteristic transverse (y -direction) spatial scale is $\sim 10c/\omega_p$, and energy conversion ratio from kinetic to electromagnetic is order 0.1. Not negligible amount of energy density is converted to the small scale electromagnetic field.

The magnetic reconnection is also an energy conversion process, which converts magnetic energy to the kinetic energy by rearranging magnetic field topology (Sweet 1958, Parker 1957

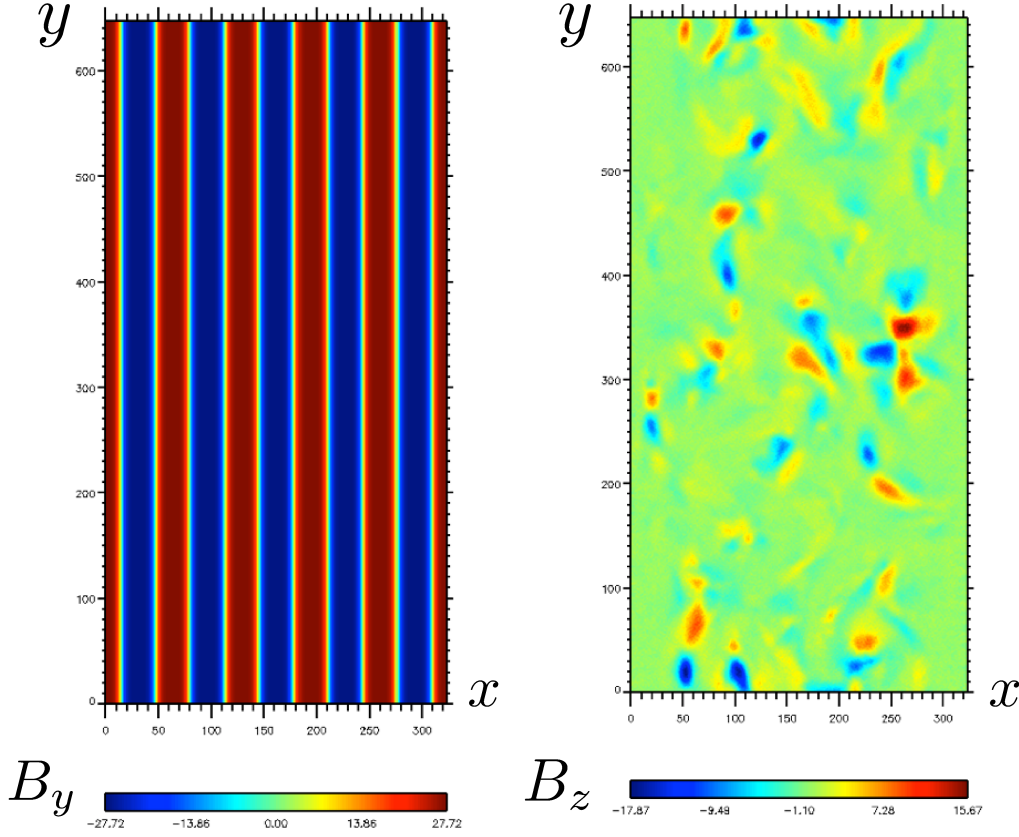


Figure D.2: Left panel: The initial magnetic field B_y is shown in $x - y$ plane. The coordinates are normalized by Debye length, which is $1/(2\sqrt{2} \times \text{inertial length})$. Right panel: The B_z component of the formed electromagnetic field.

and Petscheck 1964). This process involves not only dissipation of magnetic field but also generating electromagnetic field. For example, simulation results which shows magnetic field generation by Weibel instability are shown by Zenitani & Hesse 2008, Swisdak 2008. Moreover, the reconnection jets would form a counter streaming configuration. It would become a generation site of electromagnetic field, because the velocity distribution is unstable as we show in next section. We next show our results of non-relativistic magnetic reconnection in Figure D.2. We perform this simulation by using an open code of pCANS (<http://www.astro.phys.s.chiba-u.ac.jp/pcans/>). We set multi Harris current sheets, which mimics Parker spiral (Parker 1958),

which is seen in heliosphere. The relativistic wind with striped magnetic field is called "Striped Wind" (Coroniti 1990), which is thought to blow from the pulsars. We here use non relativistic pair plasma, and simulate multi current reconnection. The initial condition is as follows. Ten current sheets are set in $y - z$ plane alternately with width equating inertial length c/ω_p , and the current density \vec{j} is along $\pm z$. This configuration is unstable to the tearing-mode instability. These current sheets instantaneously reconnect and form the turbulence. We show the initial configuration of magnetic field B_y in left panel of Figure D.2 and B_z component of formed electromagnetic turbulence in right panel. The spatial scale is about $10c/\omega_p$, and the maximum strength is around 50% of the initial magnetic field strength.

D.2 Linear analysis

We shortly review the instabilities which we assume in this thesis. First, we derive dispersion relation of waves for unmagnetized plasma. We can neglect background magnetic field when the timescale is shorter than cyclotron period. It can be achieved in many astrophysical objects. Next, we drive electromagnetic Weibel/filamentation instability and electrostatic two-stream instability. In general, these instabilities couple (Bret et al. 2004), while we treat them separately for simplicity.

D.2.1 Dispersion relation

The linearized Maxwell equations for electric field $\delta\vec{E}$ and magnetic field $\delta\vec{B}$ are given as:

$$\frac{\partial}{\partial t}\delta\vec{E} = c\nabla \times \delta\vec{B} - 4\pi\delta\vec{j}, \quad (\text{D.1})$$

$$\frac{\partial}{\partial t}\delta\vec{B} = c\nabla \times \delta\vec{E}, \quad (\text{D.2})$$

where $\delta\vec{j}$ and c are current density and speed of light. In the plasma, the current corresponding to the electric field appears. When the electric field is small, the current is expressed by Ohm's

law,

$$\delta \vec{j} = \overleftrightarrow{\sigma} \cdot \delta \vec{E}, \quad (\text{D.3})$$

where $\overleftrightarrow{\sigma}$ is the electric conductivity tensor and obtained from linearized Boltzmann equation. Performing Fourier expansion of $\delta \vec{E}$, $\delta \vec{B}$, and $\delta \vec{j}$, equations (D.1), (D.2), and (D.3) are reduced as follows:

$$0 = \overleftrightarrow{D}(\vec{k}, \omega) \cdot \delta \vec{E}_k \quad (\text{D.4})$$

$$\overleftrightarrow{D}(\vec{k}, \omega) \equiv \overleftrightarrow{I} + \frac{4\pi i \overleftrightarrow{\sigma}}{\omega} - \left(\frac{ck}{\omega} \right)^2 \left(\overleftrightarrow{I} - \frac{\vec{k} \otimes \vec{k}}{k^2} \right), \quad (\text{D.5})$$

where \vec{E}_k is the Fourier amplitude of the mode (\vec{k}, ω) .

To obtain $\overleftrightarrow{\sigma}$, we use linearized collisionless Boltzmann equation. Since we here treat unmagnetized plasma, background electromagnetic field is zero. Then, it is written as

$$\frac{\partial}{\partial t} \delta f_s + \vec{v} \cdot \nabla \delta f_s + \frac{q_s}{m_s} \left(\delta \vec{E} + \frac{\vec{v}}{c} \times \delta \vec{B} \right) \cdot \nabla_v f_{s,0} = 0, \quad (\text{D.6})$$

where q_s , m_s , δf_s , and $f_{s,0}$ are the particle charge, particle mass, perturbation of the distribution function, and the background distribution function, respectively, and the subscript "s" represent particle species. The current $\delta \vec{j}$ is given by

$$\delta \vec{j} = \sum_s \int q_s \vec{v} \delta f_s d^3v. \quad (\text{D.7})$$

Performing the Fourier expansion of $\delta \vec{E}$, $\delta \vec{B}$, and δf_s , from (D.1), (D.2), (D.3), (D.6), and (D.7), $\overleftrightarrow{\sigma}$ is written as

$$\overleftrightarrow{\sigma} = - \sum_s \frac{q_s}{im_s \omega} \left[n_{s,0} - \int (\vec{k} \cdot \nabla_v f_{s,0}) \frac{\vec{v} \otimes \vec{v}}{\omega - \vec{k} \cdot \vec{v}} d^3v \right], \quad (\text{D.8})$$

where $n_{s,0} = \int f_{s,0} d^3v$ is the number density. Once the distribution function $f_{s,0}$ is given, we can calculate above $\overleftrightarrow{\sigma}$ and solve the dispersion relation (D.4).

The terminology of the instabilities we treat below is somewhat confusing. We define the orientations of electric/magnetic field and wavevector for each instabilities according to

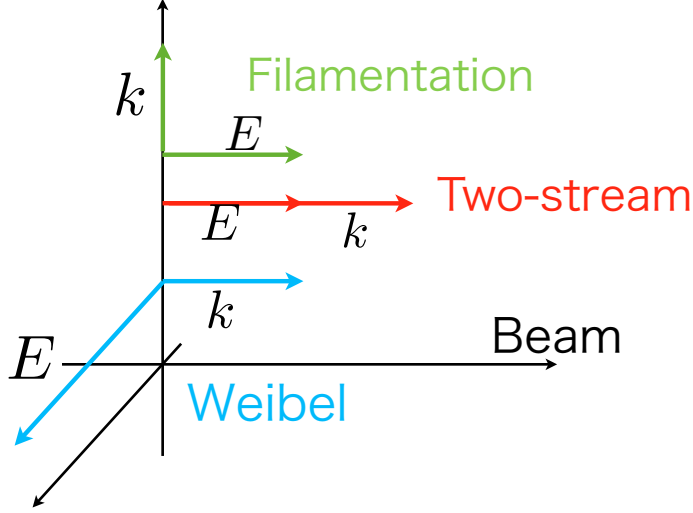


Figure D.3: Weibel, two-stream, and filamentation modes.

Bret et al. (2005). We depict them in figure D.3. However, it is widely recognized that the filamentation mode is identical to the Weibel instability, and they are in electromagnetic modes. Therefore, we call them "Weibel instability". On the other hand, the name "two stream instability" is sometimes used for electromagnetic mode, but originally it is an electrostatic mode. Thus, we call "two-stream instability" as an electrostatic mode only.

D.2.2 Weibel (filamentation) instability

The Weibel instability is firstly introduced by Weibel (1959), which produces transverse waves with an important magnetic component growing aperiodically, i.e., the real frequency $\omega_r = 0$ and growth rate $\omega_i > 0$. We derive the growth rate on the assumption that non-relativistic electron-ion plasma which has anisotropic temperature. The physical picture and condition in high energy astrophysical objects may be somewhat different from it. For example, the

emission region we assume is relativistic shock region. The plasma is expressed as two counter streaming beams, furthermore, the plasma is usually relativistic. The dispersion relation for counter streaming beams is almost identical to the one of the Weibel instability for thermal velocity \sim streaming beam velocity. As for the relativistic effects, although the growth rate of Weibel instability in relativistic regime is larger than in non relativistic regime, the physical mechanism is same as non-relativistic regime. Therefore, we consider Weibel instability in non-relativistic anisotropic plasma, and we show the relativistic correction after that.

We here define the x-direction as the wave vector direction. For simplicity, we assume that the distribution function of each species $f_{s,0}$ is the Maxwell distribution with the drift velocity of the y -direction,

$$f_{s,0} = \frac{n_{s,0}}{\pi^{3/2} v_{\text{th},s}^3} \exp \left[-\frac{v_x^2 + (v_y - v_{d,s})^2 + v_z^2}{v_{\text{th},s}^2} \right], \quad (\text{D.9})$$

where $v_{\text{th},s} = (2k_B T_s / m_s)^{1/2}$ is the thermal velocity and $v_{d,s}$ is the drift velocity. Substituting it to the equation (D.8), the dispersion relation (D.4) becomes

$$0 = 1 - \left(\frac{ck}{\omega} \right)^2 - \sum_s \frac{\omega_{p,s}^2}{\omega^2} + \sum_s \frac{\omega_{p,s}^2}{\omega^2} \left[2 + \left(\frac{v_{d,s}}{v_{\text{th},s}} \right)^2 \right] (1 + \xi_s Z(\xi_s)), \quad (\text{D.10})$$

$$Z(\xi_s) \equiv \frac{1}{\pi} \int_{-\infty}^{\infty} \frac{1}{z - \xi_s} e^{-z^2} dz, \quad (\text{D.11})$$

$$\xi_s = \frac{\omega - kv_{d,s}}{kv_{\text{th},s}}, \quad (\text{D.12})$$

where $Z(\xi_s)$ is the plasma dispersion function.

Next, we consider the most simple condition for Weibel instability for example. We assume counter streaming cold electron-proton plasma. Their distribution functions are

$$f_{e-,0} = n_e [\delta(v_y - v_d) + \delta(v_y + v_d)] \delta(v_x) \delta(v_z), \quad (\text{D.13})$$

and

$$f_{p-,0} = n_p [\delta(v_y - v_d) + \delta(v_y + v_d)] \delta(v_x) \delta(v_z). \quad (\text{D.14})$$

The dispersion relation (D.10) becomes

$$0 = 1 - \left(\frac{ck}{\omega}\right)^2 - 2\left(\frac{\omega_{p,e}}{\omega}\right)^2 - \left(\frac{\omega_{p,e}}{\omega}\right)^2 \left(\frac{kv_d}{\omega}\right)^2, \quad (\text{D.15})$$

where we neglect the contribution of protons because of $\omega_{p,e} \gg \omega_{p,p}$. The maximum growth rate is

$$\text{Im}[\omega] = \left(\frac{v_d}{c}\right) \omega_{p,e} \text{ at } k \gg \frac{\omega_{p,e}}{c} \quad (\text{D.16})$$

We see the typical value for growth rate is ω_p and unstable wavelength is c/ω_p .

In relativistic plasma, although the plasma frequency becomes $\omega_{p,\text{rela}} = \sqrt{4\pi ne^2/\gamma m}$, the features are unchanged. For example, the same signature on growth rate and unstable wavelength can be seen for anisotropic relativistic plasma (Yoon & Davidson 1987). In their treatment, the anisotropic electron distribution functions are

$$f_{e,0} = \frac{1}{2\pi p_\perp} \delta(p_\perp - \hat{p}_\perp) \frac{1}{2\hat{p}_z} H(\hat{p}_z^2 - p_z^2), \quad (\text{D.17})$$

where p_z , p_\perp and $H(x)$ are momentum of z -direction, momentum of perpendicular to z -direction, and Heaviside step function, respectively. The protons are assumed as stationary. For $p_\parallel \gg p_\perp$, the maximum growth rate Γ_{max} and corresponding wave vector of the fastest growing mode k_{max} are

$$\Gamma_{\text{max}} \sim \omega_{p,\text{rela}} \quad (\text{D.18})$$

$$k_{\text{max}} \sim \frac{\omega_{p,\text{rela}}}{c} (1 - \beta_\perp^2)^{1/4}, \quad (\text{D.19})$$

where $\beta_\perp = p_\perp/\gamma m_e c$ is the perpendicular velocity per light speed. As you see above, the growth rate and corresponding wavelength are nearly plasma frequency and inertial length, respectively.

If the gyro frequency is much smaller than the plasma frequency at the unperturbed state, the assumption that unmagnetized plasma which we take in this Appendix D is justified because the growing time $\sim 1/\omega_p$ is much shorter than gyration time. It is usually achieved for the initial condition, and it is also maintained in the saturation level. The saturation level

is limited by Alfvén critical current (Alfvén 1939, Kato 2005). The critical current for the column current is determined as

$$I_A = \frac{\gamma m c^2 v}{e}, \quad (\text{D.20})$$

which does not depend on the radius of the column. We calculate the magnetic field strength on the surface of the column when the $I = I_A$ and the radius is inertial length.

$$B_A \simeq \frac{\gamma m c \omega_{p,\text{rela}}}{e} \quad (\text{D.21})$$

We drive the condition

$$\frac{eB}{\gamma m c} \lesssim \omega_{p,\text{rela}}. \quad (\text{D.22})$$

Therefore, the gyro frequency is always smaller than plasma frequency, i.e., growth rate, when the initial condition is $\omega_{\text{cyc}} < \omega_p$.

D.2.3 Two stream instability

The two stream instability has a broad meaning for the electrostatic instability which occurs when two species of plasma have relative drift velocity. Furthermore, sometimes the term is used for electromagnetic instabilities as we showed above. We here use narrowly-defined term as the instability resulting from coupling with the beam mode and the Langmuir plasma mode. We first assume the distribution function of each species $f_{s,0}$ is Maxwell distribution with the drift velocity of the x direction,

$$f_{s,0} = \frac{n_{s,0}}{\pi^{3/2} v_{\text{th},s}^3} \exp \left[-\frac{(v_x^2 - v_{d,s})^2 + v_y^2 + v_z^2}{v_{\text{th},s}^2} \right]. \quad (\text{D.23})$$

Then, the dispersion relation (D.4) becomes

$$0 = 1 + \sum \frac{2\omega_{p,s}^2}{k^2 v_{\text{th},s}^2} [1 + \xi_s Z(\xi_s)]. \quad (\text{D.24})$$

We next simplify the condition that a cold electron beam ($s=\text{eb}$) in the cold electron-proton plasma ($s=\text{p,e}$). This is three component plasma with drift velocity. We assume

current neutrality, Because of the charge and current neutralities, the following conditions are satisfied

$$0 = n_p - n_e - n_{eb}, \quad (\text{D.25})$$

$$0 = n_p v_{d,p} - n_e v_{d,e} - n_{eb} v_{d,eb}, \quad (\text{D.26})$$

where n_s and $v_{d,s}$ are the number density and the drift velocity of each component. We here chose background electron ($s=e$) rest frame, that is, $v_{d,e} = 0$. Assuming $|\xi_s| \gg 1$, we get the dispersion relation from equations (D.4) and (D.11)

$$0 = 1 - \left(\frac{\omega_{p,e}}{\omega} \right)^2 - \left(\frac{\omega_{p,p}}{\omega - kv_{d,p}} \right)^2 - \left(\frac{\omega_{p,eb}}{\omega - kv_{d,eb}} \right)^2. \quad (\text{D.27})$$

We assume $n_p \gg n_{eb}$ ($v_{dp} \ll v_{dbe}$) and $\omega \sim kv_d \ll \omega_{p,e}$, then growth rate $\gamma_{ts} = \text{Im}[\omega]$ is

$$\gamma_{ts} = \frac{kv_{d,eb}}{1 + n_{be}/n_p} \left(\frac{n_{eb}}{n_p} \right)^{1/2}. \quad (\text{D.28})$$

As k becomes larger, the growth rate becomes large. On the other hand, the growth rate has maximum value when $\omega_e = \omega_{be}$ for a given k , which means $v_e \sim -v_{be}$, i.e., the electron fluids has two stream condition.

The two stream instability is considerably modified when the beam density is much less than the density of the ambient plasma, $n_{be} \ll n_e$. In the shock region of the high energy astrophysical objects, the number of the reflected electrons is less than the number of bulk electrons. Therefore, we next consider the case of $n_{be} \ll n_e$. We introduce a new variable as

$$\Omega = \omega - \omega_{p,e}. \quad (\text{D.29})$$

Equation D.27 then reduces to

$$2\Omega(\omega - kv_{eb})^2 - \omega_{p,e}\omega_{p,eb}^2 = 0. \quad (\text{D.30})$$

Here we used the approximation that $1 - \omega_{p,e}^2/\omega^2 \sim 2\Omega/\omega_{p,e}$, for $\omega \sim \omega_{p,e}$. Furthermore, we assume $\omega_{p,0} \sim kv_{d,be}$, we get the frequency

$$\omega_{wb} = \omega_{p,e} \left[1 + \left(\frac{n_{eb}}{2n_e} \right)^{1/3} \right], \quad (\text{D.31})$$

where ω_{wb} is the frequency of the two stream instability in weak beam regime. The growth rate is calculated as

$$\gamma = \sqrt{3}\omega_{\text{p,e}} \left(\frac{n_{\text{eb}}}{2n_{\text{e}}} \right). \quad (\text{D.32})$$

The growth rate is much lower than the case of $n_{\text{be}} \sim n_{\text{be}}$. On the other hand, this is a high frequency instability close to the back ground plasma frequency. Thus, weak beam excites Langmuir wave at small growth rate. The general excitation processes have been on the discussion (e.g., Dieckmann 2005, Bret et al. 2006). The Langmuir waves would be generated in shock region.

Bibliography

- [1] Abdo, A. A., et al. 2011, *Science*, 331, 739
- [2] Achterberg, A., Gallant, Y. A., Kirk, J. G. Guthmann, A. W. 2001, *MNRAS*, 328, 393
- [3] Akhiezer, A. I., & Shul'ga, N. F. 1987, *Sov. Phys.–Usp.*, 30, 197
- [4] Alfven, H, 1939, *Phys. Rev.* 55, 425
- [5] Atoyan, A. M., & Aharonian, F. A. 1996, *MNRAS* 278, 525
- [6] Band, D. et al. 1993, *ApJ*, 413, 281
- [7] Bednarek, W., & Idec, W. 2011, *MNRAS*, 414, 2229
- [8] Bernstein, I. B. 1957, *PhRv.* 108, 546
- [9] Bhat, N. D. R., Tingay, S.J., & Knight, H. S. 2008, *ApJ*, 676, 1200
- [10] Bret, A., Firpo, M.-C., & Deutsch, C. 2004, *PRE*, 70, 046401
- [11] Bret, A., Firpo, M.-C., & Deutsch, C. *PRL*, 2005, 94, 115002
- [12] Bret, A., Dieckamnn, M. E., & Deutch, C., *PHPl*, 13, 082109
- [13] Buehler, R. et al. 2012, *ApJ*, 493, 291

-
- [14] Buneman, O., 1993, in *Computer Space Plasma Physics*, ed. H. Matsumoto & Y. Omura (Tokyo: Terra Scientific), 67
 - [15] Bykov, A. M., Pavlov, G.G., Artemyev, A. V., & Uvarov, Y. A. 2012, *MNRAS*, 421, L67
 - [16] Cerutti, B., Uzdensky, D. A., Begelman, M. C. 2012, *APJ*, 746, 148
 - [17] Cerutti, B., Werner, G. R., Uzdensky, D. A., & Begelman, M. C. 2013, arXiv:1311.2605
 - [18] Chang, P., Spitkovsky, A., & Arons, J. 2008, *ApJ*, 530, 292
 - [19] Clausen-Brown, E., & Lyutikov, M. *MNRAS*, 426, 1374
 - [20] Crusius, A. & Schlickerser, R., 1986, *A&A*, 164, L16
 - [21] De Jager, O. C., & Harding, A. K. 1992, *ApJ*, 396, 161
 - [22] Dieckmann, M. E. 2005, *Phys. Rev. Lett.*, 94, 155001
 - [23] Drury, L. O'C. 1983, *Rep. Prog. Phys*, 46, 973
 - [24] Epstein, R. I. 1973, *ApJ*, 183, 593
 - [25] Fleishman, G. D. 2005, arXiv:astro-ph/0510317v1
 - [26] Fleishman, G. D. 2006, *Apj*, 638, 348
 - [27] Fleishman, G. D., & Bietenholz, M. F. 2007, *MNRAS*, 376, 625
 - [28] Fleishman, G. D., & Toptygin, I. N. 2007a, *Phys. Rev. E.*, 76, 017401
 - [29] Fleishman, G. D., & Toptygin, I. N. 2007b, *MNRAS*, 381, 1473
 - [30] Fleishman, G. D., & Urtiev, F. A. 2010, *MNRAS*, 406, 644
 - [31] Frederiksen, J.T., Haugbolle, T., Medvedev, M.V., & Nordlund, A. 2010, *ApJ*, 722, L114

-
- [32] Fredediksen, J. T., Hededal, C.B., Haugbolle, T., & Nordlund, A. 2004, *ApJ*, 608, L13
 - [33] Gaensler, B. M., & Slane, P. O. 2006, *ARAA*, 44, 17
 - [34] Gailitis, A. K., & Tsytovich, V. N., 1964, *Sov. Phys. -JETP*, 19, 1165
 - [35] Getmantsev, G. G., 1971, *Nature Phys. Sci.* 229, 199
 - [36] Getmantsev, G. G. & Tokarev, Y. V., 1972, *Ap&SS*, 18, 135
 - [37] Giacalone, J., & Jokipii, J. R. 1999 *ApJ*, 520, 204
 - [38] Ginzburg V. L., & Syrovaatskii, S. I. 1965, *ARA&A*, 3, 297
 - [39] Ginzburg, V. L., & Tsytovich, V. N. 1984, *The transition radiation and transition scattering*, Nauka, Moscow
 - [40] Haugbolle, T. 2010, *arXiv:astro-ph/1007.5082v1*
 - [41] Hededal, C. 2005, PhD thesis, Nils Bohr Institute, *arXiv:astro-ph/0506559*
 - [42] H.E.S.S. Collaboration 2013, *arXiv:1311.3187*
 - [43] Hoshino, M. 2012, *PRL*. 108, 135003
 - [44] Jackson, J. D. 1999, *Classical Electrodynamics* (3rd ed.;New York:Wiley)
 - [45] Jorstad, S. G., et al. 2005, *AJ*, 130, 1418
 - [46] Kato, T. N. 2005, *Physics of Plasmas* 12, 080705
 - [47] Kaneko, Y. et al. 2006, *ApJS*, 166, 298
 - [49] Kelner, S. R., & Aharonian, F. A. 2012, *arXiv:1207.6903*
 - [49] Kelner, S. R., Aharonian, F. A., & Khangulyan, D. 2013, *ApJ*, 774, 61

-
- [50] Kennel, C. F., & Coroniti, F. V. 1984, ApJ, 283, 710
- [51] Kirk, J. G., & Reville, B. 2010, ApJ, 710, L16
- [52] Kohri, K., Ohira, Y., & Ioka, K. 2012, MNRAS, 424, 2249
- [53] Komissarov, S. S., & Lyutikov, M., 2011, MNRAS, 414, 2017
- [54] Kuzmin, A. D., Losovsky, B. Ya., Logvineko, S.V., & Litvinov, I. I. 2008, Astron. Zh. 85, 1011
- [55] Kuzmin, A. D. et al. 2011, Astron. Rep. 55, 416
- [56] Landau, L. D., & Lifshitz, E. M. 1980, The classical theory of Fields (4th ed.; Butterworth-Heinemann)
- [57] Landau, L. D., & Pomeranchuk, I. 1953, Dokl. Akad. Nauk Ser. Fiz., 92, 735
- [58] Lundgren, S. C., Cordes, J. M., Ulmer, M., & Matz, S. M.
- [59] Mao, J., & Wang, J. 2012, ApJ, 748, 135
- [60] Mao, J., & Wang, J. 2013, ApJ, 776, 17
- [61] Mayer, M., Buehler, R., Hays, E., et al. 2013, ApJ, 775, L37
- [62] Medvedev, M. V., & Loeb, A. 1999, ApJ, 526, 697
- [63] Medvedev, M. V. 2000, ApJ, 540, 704
- [64] Medvedev, M. V. 2006, ApJ, 637, 869
- [65] Medvedev, M. V. 2007, ApJ, 666, 339
- [66] Medvedev, M. V., Pothapragada, S. S., & Reynolds, S. J. 2009, ApJ, 702, L91
- [67] Medvedev, M.V., Frederikseni, J. T., Haugblle, T., & Nordlund, A. 2011, ApJ, 737, 55

-
- [68] Melrose, D. B. 1971, *Ap&SS*, 10, 197
- [69] Mickaliger, M. B. et al. 2012, arXiv: astro-ph/1210.0452v1
- [70] Migdal, A. B. 1956, *Phys. Rev.*, 103, 1811
- [71] Morsony, B. J., Workman, J. C., Lazatti, D., & Medvedev, M. V. 2000, *MNRAS*, 312, 1397
- [72] Nishikawa, K. -I. et al 2011, *Adv. Space Res.* 47, 1134
- [73] Ojha, R. , Buhler, R., Hays, E., and Dutka, M. et al. 2012 ATEL # 4239
- [74] Ostriker, J. P. & Gunn, J. E. 1969, *ApJ*, 157, 1395
- [75] Panaitescu, A., & Meszaros, P. 1998, *ApJ*, 493, L31
- [76] Parker, E. N. 1957, *JGR*, 62, 509
- [77] Parker, E. N. 1958, *ApJ*, 128, 664
- [78] Perlman, E. S., Georganopoulos, M., May, E. M., & Kazanasa, D. 2010. *ApJ*. 708, 1
- [79] Petschek, H. E. 1964, *NASSP*, 50, 425
- [80] Preece, R. D., et al. 1998, *ApJ*, 506, L23
- [81] Rees, M. J. 1971, *IAUS*, 46, 407
- [82] Rees, M. J., & Gunn, F. E. 1974, *MNRAS*, 167, 1
- [83] Reville, B., & Kirk, J. G. 2010, *ApJ*, 724, 1283
- [84] Reynolds, S. J., Pothapragada, S., & Medvedev. M. V.
- [85] Reynolds, S. J., & Medvedev, M. V. 2012, *PhPl*, 19, 023106

-
- [86] Rybicki, R. D., & Lightman, A. D. 1979, *Radiative Processes in Astrophysics* (New York: Willey)
- [87] Schott, G. A. 1912, Cambridge university Press, 109
- [88] Schwinger, J. 1949, *Physical review*, 75, 12
- [89] Schlickeiser, R., 2003, *A & A*, 410, 397
- [90] Silva, L. O. 2006, *AIPC*, 856, 109
- [91] Sironi, L., & Spitkovsky, A. 2009, *ApJ*, 707, L92
- [92] Sironi, L., & Spitkovsky, A. 2011, *ApJ*, 741, 39
- [93] Sweet, P. A. 1958, *IAUS*, 6, 123
- [94] Swisdak, M., Lin, Yi-Hin, & Deake, J. F. 2008, *ApJ*, 680, 999
- [95] Tanaka, S. J., & Takahara, F. 2010, *ApJ*, 715, 1248
- [96] Tanaka, S. J., & Takahara, F. 2011, *ApJ*, 741, 40
- [97] Tavani, M., et al. *Science*, 331, 736
- [98] Teraki, Y., & Takahara, F. 2011, *ApJ*, 735, L44
- [99] Teraki, Y., & Takahara, F. 2013, *ApJ*, 763, 131
- [100] Terasawa, T. 2011, Private communication
- [102] Toptygin, I. N. & Fleishman, G. D. 1987, *Ap&SS*, 132, 213
- [102] Toptygin, I. N., & Fleishman, G. D. 1987, *Ap&SS*. 133,213T
- [103] Treumann, R. A., Baumjohann, W. 1997, *Advanced Space Plasma Physics* (London:Imperial College Press)

-
- [104] Tsunemi, H., 2008, "Supernova remnants", Official site of physical chronological table (NAOJ, maruzen)
- [105] Tsytovich, V. N., & Chikhachev, A. S. 1969, SvA, 13, 385
- [106] The VERITAS Collaboration, Aliu, E., Archambault, S., et al. 2013, arXiv: 1309.5949
- [107] Vittorini, V., et al. 2011, ApJ, 732, L22
- [108] Uchiyama, Y. et al. 2006, ApJ, 648, 910
- [109] Uchiyama, Y. et al. 2007, ApJ, 661, 719
- [110] Uzdensky, D. A., Cerutti, B., & Begelman, M. C. 2011, ApJ, 737, L40
- [111] Weibel, E, S. 1959, PRL, 2, 83
- [112] Workman, J. C., Morsony, B. J., Lazatti, D., & Medvedev, M. V. 2008, MNRAS, 386, 199
- [113] Yonetoku, D. et al. 2012, ApJ, 758, L1
- [114] Yuan, Q., Yin, P.-F., Wu, X.-F., et al. 2011, ICRC, 7, 259
- [115] Yuan, Q., Yin, P.-F., Wu, X.-F., et al. 2011, ApJ, 730, L15
- [116] Zenitani, S., & Hesse, M., 2008, PhPl, 15, 2101